MULTICOMPONENT DOPED BARIUM STRONTIUM TITANATE THIN FILMS FOR TUNABLE MICROWAVE APPLICATIONS

A Dissertation
Submitted to the Graduate Faculty
of the
North Dakota State University
of Agriculture and Applied Science

By

Fikadu Legesse Alema

In Partial Fulfillment of the Requirements
for the Degree of
DOCTOR OF PHILOSOPHY

Major Department:
Materials and Nanotechnology

November 2014

Fargo, North Dakota

North Dakota State University
Graduate School

Title

Multicomponent Doped Barium Strontium Titanate Thin Films For Tunable Microwave Applications

By

Fikadu Legesse Alema

The Supervisory Committee certifies that this ***disquisition*** complies with North Dakota State University's regulations and meets the accepted standards for the degree of

DOCTOR OF PHILOSOPHY

SUPERVISORY COMMITTEE:

Dr. Konstantin Pokhodnya
Chair

Prof. Erik Hobbie

Prof. Kalpana Katti

Dr. Michael Reich

Approved:

11/12/2014	Prof. Erik Hobbie
Date	Department Chair

ABSTRACT

In recent years there has been enormous progress in the development of barium strontium titanate (BST) films for tunable microwave applications. However, the properties of BST films still remain inferior compared to bulk materials, limiting their use for microwave technology. Understanding the film/substrate mismatch, microstructure, and stoichiometry of BST films and finding the necessary remedies are vital. In this work, BST films were deposited via radio frequency magnetron sputtering method and characterized both analytically and electrically with the aim of optimizing their properties.

The stoichiometry, crystal structure, and phase purity of the films were studied by varying the oxygen partial pressure (OPP) and total gas pressure (TGP) in the chamber. A better stoichiometric match between film and target was achieved when the TGP is high (> 30 mTorr). However, the O_2/Ar ratio should be adjusted as exceeding a threshold of 2 mTorr in OPP facilitates the formation of secondary phases. The growth of crystalline film on platinized substrates was achieved only with a lower temperature grown buffer layer, which acts as a seed layer by crystallizing when the temperature increases.

Concurrent Mg/Nb doping has significantly improved the properties of BST thin films. The doped film has shown an average tunability of 53%, which is only ~8 % lower than the value for the undoped film. This drop is associated with the Mg ions whose detrimental effects are partially compensated by Nb ions. Conversely, the doping has reduced the dielectric loss by ~40 % leading to a higher figure of merit. Moreover, the two dopants ensure a charge neutrality condition which resulted in significant leakage current reduction. The presence of large amounts of empty shallow traps related to $Nb_{Ti}^{\bullet}$ localize the free carriers injected from the contacts; thus increase the device control voltage substantially (>10 V).

A combinatorial thin film synthesis method based on co-sputtering of two BST sources doped with Mg/Nb and Ce, respectively, was applied. The composition and the dielectric properties of the deposited film were correlated and the optimal concentration of dopants corresponding to high tunability and low dielectric loss was determined in a timely fashion.

ACKNOWLEDGMENTS

First and foremost, my deepest gratitude goes to my advisor, Dr. Konstantin Pokhodnya, for his continuous guidance and mentorship over the course of this work. I'm very grateful for his support in the ups and downs of this journey. Dr. Pokhodnya has not only been an academic mentor for me, he was someone that I could always count on for advice on matters outside research as well. Thank you for giving me the opportunity to work with you. I'm also thankful for my committee members, Prof. Erik Hobbie, Prof. Kalpana Katti, and Dr. Michael Reich, for closely following the progress of my work and providing valuable comments in this dissertation.

My sincere appreciation to my past and present colleagues at the Center for Nanoscale Science and Engineering (CNSE), NDSU is enormous. I would like to thank Joseph Sandstorm, Matthew Mumm, James Bahr, Kevin Mattson, Greg Strommen, Eric Jarebeck, Margaret Piranian, Chris Olson, and all others whom I could have forgotten to mention for making CNSE a fun place to work.

I would like to acknowledge the financial support through the Defense Microelectronics Activity (DMEA) and National Science Foundation (NSF) under Agreement Numbers H94003-11-2-1103 and DMR-1005882, respectively. Without these funding agencies, the achievements in this dissertation would not have been possible.

I'm particularly grateful to my parents, Askale Regassa and Legesse Alema, who have always believed in me and encouraged me with their blessing to be the person that I'm. Their determination to send me to school with no basic education for themselves is what kept me going this far. The support of my brothers and sisters has been enormous. My uncle, Habtamu Regassa, was also instrumental in shaping my life. His words of optimism, though we are miles away from each other, have been sources of strength for me.

Last and most importantly, I want to thank my wife, Mestawet Aweke; and daughter, Simbo Legesse for always being there for me. The support, patience and unconditional love of my wife are never forgotten. My little angle, Simbo, I love you so much. Thank you for coming into my life and make me smile even when things are not right.

DEDICATION

To my grandparents,

Regassa Ayane Biyo

and

Bizunesh Dejene Aderu

TABLE OF CONTENTS

LIST OF TABLES

LIST OF FIGURES

Figure Page

LIST OF ABBREVIATIONS

AFM.....Atomic Force Microscopy

BMN .....Barium Magnesium Niobate

BST .....Barium Strontium Titanate

BTO.....Barium titanate

CCS.....Continuous Composition Spread

CDMA.....Code Division Multiple Access

CMS .....Combinatorial Materials Science

CSD.....Chemical Solution Deposition

CTE.....Coefficient of Thermal Expansion

CVD .....Chemical Vapor Deposition

DCS.....Discrete Composition Spread

FESEM.....Field Emission Scanning Electron Microscopy

GIXRD.....Grazing Incidence X-ray diffraction

GPS .....Global Positioning System

GS .....Ground-Signal

GSG.....Ground-Signal-ground

GSM.....Global System for Mobile Communications

ICDD.....International Center for Diffraction Data

ICP-OES .....Inductively Coupled Plasma - Optical Emission Spectroscopy

LAN .....Local Area Network

LST .....Lyddane-Sachs-Teller

MIM .....Metal-Insulator-Metal

MOCVD.....Metal-Organic Chemical Vapor Deposition

MOD .....Metal Organic Deposition

OPP .....Oxygen partial pressure

PE.....Poole Frenkel

PLD .....Pulsed Laser Deposition

PVD.....Physical Vapor Deposition

RBS .....Rutherford Backscattering Spectroscopy

RF.....Radio Frequency

RPM .....Rotation per minute

STO .....Strontium titanate

SE.....Schottky Emission

TGP .....Total gas pressure

XRD .....X-ray diffraction

XRF.....X-ray Fluorescence

XRR .....X-ray Reflectivity

LIST OF APPENDIX FIGURES

1. INTRODUCTION AND MOTIVATION

Over the last 30 years, the wireless communication technologies have evolved through a number of development generations that led to the improvement of systems, increased functionalities, and reduced size as well as cost. Today, modern mobile phones are required to operate in multiple frequency bands and offer multiple modes of operations. For example, a quad-band GSM phone can operate in four dissimilar frequency bands of 850 MHz, 900 MHz, 1800 MHz, and 1900 MHz [1] which can be used depending on what part of the globe the telephone is operated in. Similarly, a mobile phone with multiple modes of operation (e.g. GSM, CDMA, etc.) can switch between the available modes. More so, a mobile phone with combined multiband and multimode operations is ideal as it allows switching between frequency bands and transmission modes as required. Apart from basic communication services, modern mobile phones offer functionalities such as GPS, Wi-Fi, LAN, Bluetooth, and many more. These multi-functionalities require multiple circuits to transmit and receive wireless signals (transceivers) integrated into a single hardware component.

Although desirable for end users, the multimode and multiband functionalities create problems for microwave engineers to have well-designed and cost effective transceivers. The traditional approach to realize a multimode and multiband radio frequency (RF) transceiver is to integrate multiple discrete transceiver circuits in a single hardware component, where each of them is optimized to operate at a single frequency band. Despite the straightforward nature of this method, the duplication of circuitry increases the complexity, production cost, and space issues on the circuit board [2]. In order to curb these problems, the RF front end circuitry can be reconfigured by using tunable components which would allow replacing a single, tunable

component for several fixed components. This scheme lowers the production cost and enables additional functionalities on the hardware.

Circuit tuning is done using tunable capacitors known as varactors, which are electrical components that change their capacitance by applying an external control signal such as the electric field [3], magnetic field [4], or mechanical force [5]. However, electrically tunable capacitors are preferred and widely used to fabricate reconfigurable components for RF and microwave applications due to their small size, light weight and monolithic integration with active devices [3]. In recent years, ferroelectric barium strontium titanate (BST) thin films have attracted considerable attention to fabricate microwave components due to the high dielectric constant that can be tuned by an electric field and a fairly low dielectric loss at microwave frequencies. Numerous reports have shown that BST based tunable devices have been successfully used as key elements of phase shifters, delay lines, filters, and matching networks [3, 6-9]. On the other hand, to fully contest with existing microwave technologies (semiconductor varactors, and micro-electro-mechanical systems (MEMS)), BST varactors must demonstrate high tunability, low dielectric losses, and good insulating properties [10]. In what follows, the existing tunable varactor technologies are compared to realize and appreciate the capabilities of the ferroelectric varactors.

1.1. Microwave Technologies

As pointed out above, currently, semiconductor (e.g. GaAs or Si), MEMS, and ferroelectric (e.g. BST) varactors are the three widely competing technologies that are used for tunable microwave devices [11, 12]. The principle to realize a varactor in each of these technologies is different. The semiconductor varactor is based on reverse biasing a junction (pn or Schottky) with a DC field to increase the depletion width that leads to a decrease of

capacitance. It is limited to a unipolar device because if the polarity of the DC bias is reversed in such a way that the device is forward biased, the junction tends to conduct. Similarly, the MEMS varactor is based on changing the distance between two electrodes (one of the two electrodes is coated with dielectrics to prevent an electrical short) by using electrostriction actuator. The ferroelectric varactor is unique because the capacitance tuning is based on an inherent property of the material, i.e. that the permittivity is dependent on a bias field.

Table 1.1. Comparison between varactor technologies [11, 12]

	GaAs	MEMS	BST
Tunability, n_r (%)	50-83	33-67	50-75
Q-factor	20-50 (10GHz)	Very high	20-100 (10GHz)
Control Voltage (V)	<15 (unipolar)	<50(bipolar)	<15(bipolar)
Tuning Speed	~1μs	~10μs	~1ns
Reliability	Good	Poor	Good
Cost	High	High	Low
Power handling	Poor	Good	Good
Packaging	Hermetic	Vacuum	--

Among the three, the most widely used and proven technology is the semiconductor varactors (e.g. GaAs) [13]. The advantages of semiconductor varactors include large tunability, low control voltage and its easy integration with the standard complementary metal oxide semiconductor (CMOS) systems. However, the poor quality factor which worsens with frequency, the poor power handling capability owing to the reverse bias requirement, and the cost are limiting its applicability. Table 1.1 presents the pros and cons of the three technologies based on desirable electrical properties that are required for microwave applications: tunability, quality factor, control voltage, power handling capability, and tuning or switching speed.

The BST varactors are reliable; and require low control voltage as in GaAs varactors. Besides, the BST varactors have some important advantages over the semiconductor varactors

including low dielectric loss [14], low material cost, fast tuning speed, and good power handling capability. The power handling capability of BST is better due to the polarity independent bias and therefore no forward conduction region as it is the case for semiconductor varactors [15].

The MEMS varactors have the highest quality factor (Q) and good power handling capability. However, they suffer from slow tuning speed, and require high control voltage compared to BST varactors. In addition, the low tunability and high packaging cost together with the poor reliability due to the mechanical moving parts puts MEMS at the lower performance end compared with the two other technologies.

Based on the standards given in the table, BST varactors have already exhibited excellent performance compared to the other two technologies. It is also worth noting that, as opposed to MEMS and GaAs, BST has large dielectric constant enabling the miniaturization of the microwave components [16]. However, there is still plenty of room for improving the properties of BST thin films. Factors known for degrading the properties of BST thin films, including residual stress, microstructural features, dead layers, and stoichiometry among many others affect the microwave properties of BST varactors [12]. Therefore, it is extremely important to understand the relation between materials and microwave properties of the devices in order to optimize the performance of BST based microwave components.

1.2. Scope and Outline of the Work

The prime objective of this thesis is to optimize the dielectric properties of barium strontium titanate (BST) thin films for tunable microwave applications. The thesis focuses on identifying and understanding factors that are responsible for deteriorating the permittivity, tunability, loss and resistivity of the BST thin films, and finding suitable solutions to modify them. In order to improve these properties, the use of buffer layers, controlling stoichiometry,

and doping the BST film are studied. The work involved fabrication of BST targets (in house), pure or with dopants of interest, radio frequency magnetron sputter deposition on different substrates, and use of various analytical and electrical characterization methods. A combinatorial thin film method based on co-sputtering of two BST sources each doped with dissimilar dopants was applied to determine concentration of dopants corresponding to the optimal properties of interest.

The thesis starts by revising fundamental principles of dielectric and ferroelectric materials with emphasis on the barium strontium titanate (BST) in Chapter 2. The thin film and bulk forms of BST were thoroughly reviewed and film residual stress, dead layer, microstructural effects, and stoichiometry were identified as factors that weaken the dielectric properties of BST film. Pathways to improve the properties of the thin film are also discussed. In Chapter 3, possible BST thin film deposition techniques with the emphasis on RF magnetron sputtering, analytical and device characterization methods were presented. In Chapter 4, the sputter target fabrication procedures and substrate selection are discussed. In addition, the temperature used to grow a crystalline film was determined, and the need for using a thin buffer layer to grow a crystalline BST film on a platinized substrate was also studied. In Chapter 5, the effects of total gas and oxygen partial pressure of the process chamber on the stoichiometry and phase purity of the RF magnetron sputter deposited thin film is studied. In Chapter 6, the properties of concurrent Mg/Nb doped BST thin film is studied. The Mg/Nb dopants are introduced to BST through barium magnesium niobate ($BaMg_{0.33}Nb_{0.67}O_3$) to realize a neutrality condition which introduces no free carriers into the film, and thus reduces the leakage current. In Chapter 7, RF magnetron sputtering based continuous composition spread (CCS) combinatorial thin film method is applied to BST. This method is a fast and cost effective way to introduce

multiple-dopants (three dopants in this work) and determine their concentration corresponding to high tunability and low dielectric loss in the material. In Chapter 8, the conclusion and future outlook of the work is presented.

2. LITERATURE REVIEW

2.1. A Brief Background on Dielectric Materials

Dielectrics are materials that (unlike conductors) can be polarized under an externally applied electric field. They generally have large band gap, E_g >2.5 eV, with a small number of free carriers [13], resulting in practically no current flow through them when they are placed in an electric field. Instead, the positive and negative charges in the material are displaced opposite to each other, causing a phenomenon known as dielectric polarization. This polarization field opposes an externally applied electric field to minimize the field in the dielectrics, making them efficient in storing electrostatic energy and charges [17]. In what follows, important concepts in dielectrics including electric dipole, polarization, electric displacement, dielectric constant and loss are discussed.

2.1.1. Electric Dipole and Polarization

An electric dipole ($\vec{p}$) is defined as the measure of the electrostatic effect of a pair of equal but opposite charges (±Q) separated by a finite distance, *d*. It is a vector quantity directed from the negative to the positive charge by convention, and is expressed as

$$\vec{p} = Q\vec{d} \,. \tag{2.1}$$

Although the net charge is zero, the electric dipole moment gives rise to an electric field in space and interacts with an electric field that originates from another source. The polarization ($\vec{P}$) of the dielectric is defined as the total dipole moment per unit volume [18]

$$\vec{P} = \frac{1}{volume}\sum_i \vec{p}_i \,, \tag{2.2}$$

where, $\sum \vec{p}_i$ is the total dipole moment in the material. When a dielectric material is placed in an external electric field ($\vec{E}$), the atoms or molecules in the material are polarized and the overall charge neutrality of the matter leads to following relation:

$$\vec{D} = \varepsilon_0 \vec{E} + \vec{P} = \varepsilon \vec{E} \,, \tag{2.3}$$

where, $\vec{D}$ is the electric displacement vector, ε is the permittivity of the material, and ε_0 (=8.854x10^{-12}F/m) is the permittivity of free space. This equation relates the free and bound surface charge density regardless of the nature of the polarization mechanism in the material. For an isotropic material, the polarization is related linearly to the electric field as

$$\vec{P} = \varepsilon_0 \chi_e \vec{E}, \tag{2.4}$$

where, x_e is defined as the electric susceptibility of the material. Inserting Eq. (2.4) into (2.3) the relation between relative permittivity or dielectric constant, $\varepsilon_r = {}^{\varepsilon}/_{\varepsilon_0}$, and x_e can be written as

$$\varepsilon_r = 1 + \chi_e. \tag{2.5}$$

Furthermore, denoting the number of atoms or molecules per unit volume of a dielectric material by *N*, and assuming that each atom or molecule produces one dipole moment, the polarization of the material can be expressed as

$$\vec{P} = N\alpha \vec{E}, \tag{2.6}$$

where, α is known as the polarizability of the material. This equation holds for a dilute phase dielectric material where the interaction between atoms or molecules can be neglected, and the actual (local) field experienced by an atom is equal to the applied field. In solid and liquid phases however, the local field is greater than the external field since there is polarization in the vicinity. Assuming a small and spherical shaped dielectric material, the local electric field (Lorentz field) is related to the polarization as $\vec{E}_{loc} = \vec{E} + \vec{P}/3\varepsilon_0$. With this expression, Eq. (2.6) can be modified to hold for condensed matter systems as [18, 19]

$$\vec{P} = N\alpha\vec{E}_{loc} = N\alpha\left(\vec{E} + \frac{\vec{P}}{3\varepsilon_0}\right). \quad (2.7)$$

The local field, however, does not affect the fundamental definition in Eq. (2.4), which combined with Eq. (2.7) results in an explicit relation between the local and applied field as

$$E_{loc} = \frac{2+\varepsilon_r}{3}E. \quad (2.8)$$

In addition, combining Eqs. (2.4), (2.5), and (2.7), the relation between dielectric constant and polarizability, also known as Clausius-Mossotti equation is obtained

$$\frac{\varepsilon_r - 1}{\varepsilon_r + 2} = \frac{N\alpha}{3\varepsilon_0}. \quad (2.9)$$

2.1.2. Polarization Mechanisms

Any dielectric material possesses one or more of the five basic types of microscopic polarization mechanisms that are responsible for the macroscopic polarization. These are the electronic or atomic, ionic, dipolar (orientational), spontaneous, and interface or space charge polarization mechanisms [17-20].

- *Electronic polarization (P_e)*: The electronic polarization arises in all dielectrics. It is based on the deformation of the symmetrical distribution of the electron cloud of atoms due to an externally applied electric field.
- *Ionic polarization (P_i):* this polarization occurs in ionic crystals (e.g. NaCl). The ionic crystal has cations and anions located at well-defined lattice sites. An externally applied electric field displaces these ions relative to each other, resulting in an induced net dipole moment between them.
- *Dipolar (orientational) polarization (P_d):* this occurs only in materials consisting of molecules or particles with permanent dipole moments (e.g. H_2O). At ambient temperature, the dipole moments are randomly distributed in the dielectric material. An

applied electric field orients them along its direction and results in orientational polarization. If the field is removed, the net polarization returns to zero because thermal agitation randomizes the moments.

- *Spontaneous polarization* (P_s): spontaneous polarization occurs only in single crystals or crystallites in polycrystalline materials with a non-centrosymmetric structure (e.g. ferroelectric material). A non-centro symmetric structure has a non-coinciding centroid of the negative and the positive charges which form dipoles without an external field.
- *Space charge (interfacial) polarization* (P_{sc}): this polarization is associated with mobile and trapped charges in the material. The accumulation of charges in the dielectric material near the electrodes, the trapping of carriers (electron, holes, ions) by defects at the surface or interface, and grain boundaries are some of the phenomenon under which the space charge polarization mechanism is dominant.

If a dielectric material involves all the mechanisms, the total macroscopic polarization originates from the superposition of all the microscopic polarization mechanisms as

$$\vec{P}_{total} = \vec{P}_{sc} + \vec{P}_s + \vec{P}_d + \vec{P}_i + \vec{P}_e \tag{2.11}$$

2.1.3. Frequency Response of Permittivity

In the presence of an oscillating electric field, each polarization mechanism discussed above responds in different time scales and, hence, in different frequency regimes [18, 21]. Figure 2.1 shows the dispersion of permittivity over a wide frequency range. When the frequency increases, the number of polarization mechanisms involved in polarization decreases, leaving only the electronic polarization mechanism above the infrared region.

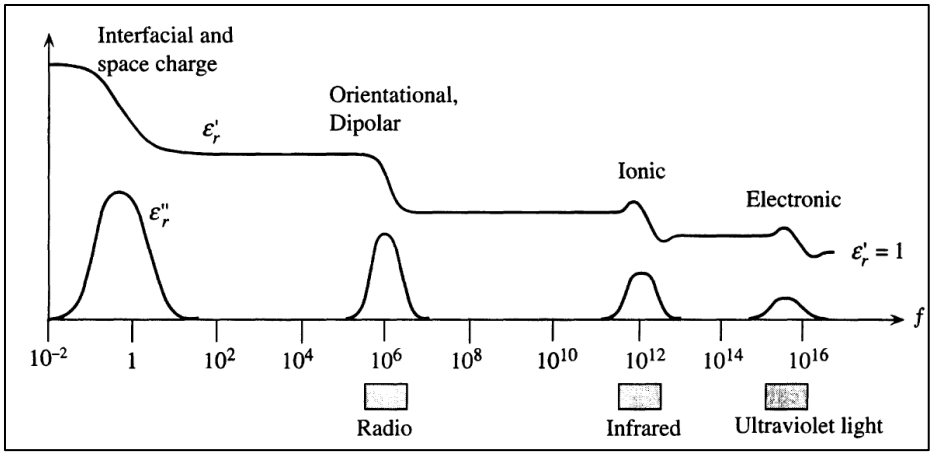

Figure 2.1. Frequency dependence of real (ε_r') and imaginary (ε_r'') parts of relative permittivity [18]

When the oscillating masses experience a restoring force, relaxation behavior is observed in space charge, spontaneous, and orientation polarization mechanisms while resonance effect is dominant in the ionic and electronic polarization [18, 21]. The slowest polarization response in a dielectric material is the space charge mechanism. It occurs in a frequency of up to 10 kHz. On the other hand, the electronic polarization mechanism is the fastest and the only mechanism that remains to respond to a very high frequency (visible region~10^{15} Hz). The orientation polarization mechanism is dominant in a radio to microwave frequency region. The infrared region (~1 to 10 THz) is dominated by resonances of ionic lattice vibration [22].

Since the polarization vector cannot always follow the change of the applied electric field, the dispersion of the dielectric response can be expressed in terms of the complex relative permittivity as

$$\varepsilon_r^* = \varepsilon_r'(\omega) - j\varepsilon_r''(\omega), \tag{2.12}$$

where, $\omega=2\pi f$ is the angular frequency; f is the frequency (in Hz) of the oscillating field, j is a complex number, and ε_r' and ε_r'' are the real and imaginary parts of the relative permittivity,

respectively. The phase shift between polarization and applied electric field leads to the energy dissipation in the dielectric material which is defined as the loss tangent (tanδ):

$$\tan\delta = \frac{\varepsilon_r''(\omega)}{\varepsilon_r'(\omega)} \tag{2.13}$$

2.2. Ferroelectrics

When single crystals or poly-crystalline materials composed of crystallites are subjected to external forces, such as electric field, stress, or heat, they undergo a small change in dimension which results in piezoelectric, pyroelectric, or ferroelectric effects. Piezoelectrics are materials in which an applied mechanical stress generates polarization (electricity) or, conversely, an electric field produces a mechanical stress. Similarly, pyroelectric materials polarize due to the change in temperature or heat. Ferroelectric materials exhibit a spontaneous polarization whose direction must be switched by an electric field [17, 20].

In crystallography, there are seven crystal systems that can be classified into 32 crystallographic point groups. Out of these, 11 classes are centrosymmetric while 21 classes are non-centrosymmetric, fulfilling the necessary requirement for the existence of piezoelectricity. However, one of the 21 non-centrosymmetric classes has other combined symmetry elements which makes it exhibit no piezoelectricity. Thus, only 20 classes of the non-centrosymetric crystals show the piezoelectric effects. Figure 2.2 shows the relationship between polarization behavior and crystal structure for the 32 point groups.

The piezoelectricity in 10 of the 20 classes can only be induced by mechanical stress; while the polarization in the remaining 10 classes can be induced both by stress and heat. Therefore, the latter 10 classes exhibit both the piezoelectric and pyroelectric effects. Ferroelectrics are a subclass within the class that possesses the pyroelectric effect exhibiting spontaneous polarization that can change direction (switchable) with an electric field.

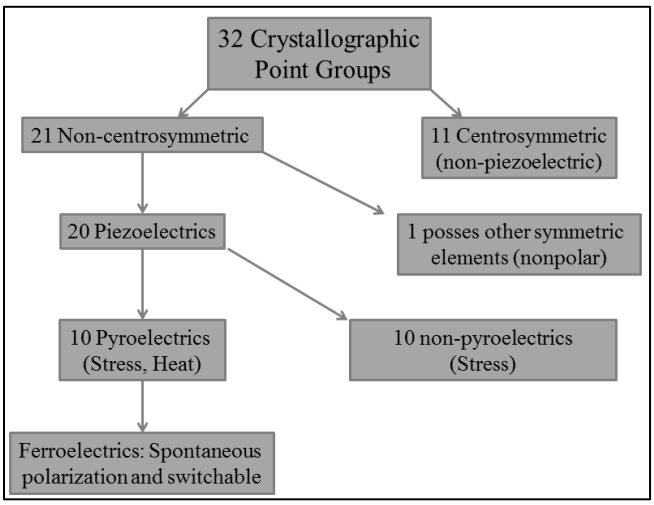

Figure 2.2. Piezoelectric, pyroelectric, and ferroelectric classification of the 32 point groups [20]

2.2.1. Fundamentals of Ferroelectricity

The ferroelectric phenomenon was discovered in 1921 when J. Valasek [23] observed an electric field reoriented spontaneous polarization in Rochell salt ($KNaC_4H_4O_6.4H_2O$) crystal. Since then several ferroelectric materials (e.g. KH_2PO_4, $BaTiO_3$, $PbTiO_3$, etc. [19]) that have been discovered and employed for numerous technological applications.

When a ferroelectric material is cooled, it undergoes a structural phase transition from a high symmetry (paraelectric) phase to a low symmetry (ferroelectric) phase. This transition occurs at a critical temperature known as Curie point, T_C, which is different for different ferroelectric materials. Above T_C (paraelectric phase), the dielectric constant (ε_r) of the material fallows an inverse relation in temperature, and is given by the Curie-Weiss law [19, 24]

$$\varepsilon_r = \frac{C}{T - T_C}, \tag{2.14}$$

where, T_C and C are the Curie temperature and constant, respectively. At and below the transition point, the material possesses spontaneous polarization by undergoing either an order-disorder (e.g. the ordering of hydrogen atoms in KH_2PO_4 crystal) or displacive (e.g. the

displacement of Ti^{4+} from its initial site invoking lattice distortion in $BaTiO_3$ crystal) type phase transition depending on the type of material [25].

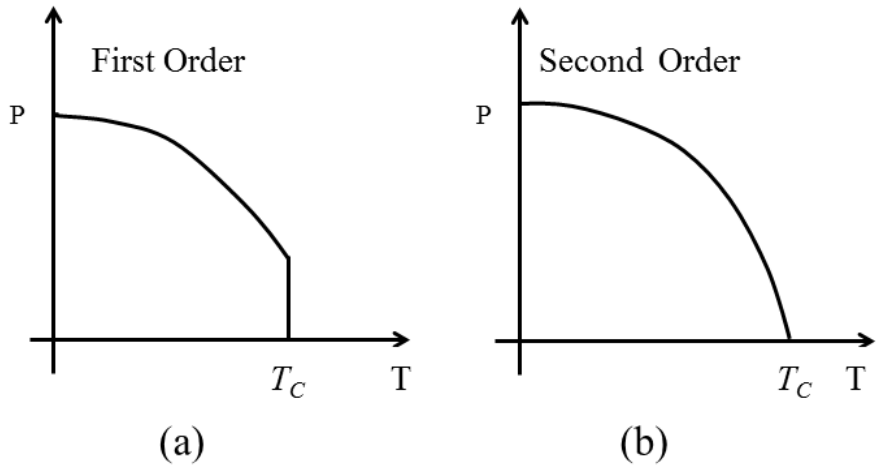

Figure 2.3. Polarization in the first (a) and second (b) order ferroelectric phase transitions

The phase transition in ferroelectric materials can be classified as first or second order phase transitions based on how the order parameter—polarization—changes with temperature at the transition point. The first order phase transition shows discontinuity in polarization, and involves associated change in volume and latent heat at the transition point (Figure 2.3a). The second order transition shows a continuous function of polarization (Figure 2.3b) without change in volume and latent heat at the transition point. However, the first derivative of polarization is discontinuous for the second order phase transition[19, 25].

There are two widely accepted viewpoints in explaining the origin of ferroelectricity which results from the structural phase transition. The first approach is known as "polarization catastrophe," referring to the situation in which the polarization becomes very large near the transition temperature. In this case, the local field caused by dipole moments in a unit cell exceeds the restoring force that stabilizes the crystal structure, leading to an asymmetrical shift

of ions from their initial positions[19, 26]. This theory can be better understood by rearranging the Clausius-Mossotti equation (Eq.(2.9)) as

$$\varepsilon_r = \frac{3\varepsilon_0 + 2N\alpha}{3\varepsilon_0 - N\alpha}. \tag{2.15}$$

From this relation, when $N\alpha = 3\varepsilon_0$, the dielectric constant becomes infinite, indicating the state of polarization catastrophe which physically shows the presence of polarization in the material without external electric field. If the external field applied to the material is turned off (i.e. $\vec{E}$ =0), the expression for polarization in Eq. (2.7) can be reduced to

$$\vec{P}\,(N\alpha - 3\varepsilon_0) = 0. \tag{2.16}$$

At the polarization catastrophe, the quantity in the bracket equals zero, which can happen only if $\vec{P} \neq 0$. By assuming the ferroelectric crystal to have polarizability that can be expressed similar to the dipolar polarization (though in fact, the two are quite different) as $\alpha = p^2/3k_BT$, where p is the average dipole moment, k_B is the Boltzmann constant, the expression for the relative permittivity in (Eq. (2.15)) can be expressed as

$$\varepsilon_r = 1 + \frac{3T_0}{(T - T_0)}, \tag{2.17}$$

where, $T_0 = Np^2/3k\varepsilon_0$. This equation resembles the Curie-Weiss law, indicating the divergence of the dielectric constant as the temperature approaches T_0, and that the system becomes unstable and must make a phase transition. However, though the obtained relation in Eq. (2.17) is reasonable and used to qualitatively describe the polarization catastrophe phenomenon, it is important to mention that it cannot substitute the Curie-Weiss law because of the involved assumptions [26].

The second theory to interpret ferroelectricity is known as the soft mode theory which can be explained based on the Lyddane-Sachs-Teller (LST) relation expressed as [19]:

$$\frac{\varepsilon(\infty)}{\varepsilon(0)} = \frac{\omega_{TO}^2}{\omega_{LO}^2}, \tag{2.18}$$

where, ω_{TO} and ω_{LO} are the transverse and longitudinal optical frequencies ($\omega_{TO} < \omega_{LO}$), respectively, and ε(∞) and ε(0) are the high and low frequency limit dielectric constant, respectively. The LST relation shows the increase in the static dielectric constant (ε(0)) with the decrease of the transverse optical frequency. Substituting the Curie-Weiss relation (Eq. (2.14)) for the static dielectric constant in the LST relation (Eq. (2.18)), one can obtain the temperature dependence of the transverse optic mode (soft mode) frequency as

$$\omega_{TO}^2 \; \alpha \; (T - T_C). \tag{2.19}$$

This equation shows as the temperature decreases the soft mode frequency approaches zero, indicating the softening of the force constant controlling the mode [25, 27, 28]. At $T=T_C$, the soft mode frequency "freezes out" (i.e. $\omega_{TO}=0$) and there is no effective restoring force to stabilize the crystal, thus leads to the occurrence of ferroelectric phase transition [28].

2.2.2. Ferroelectrics for Microwave Applications

Ferroelectric materials are used for wide range of applications including ferroelectric random access memory (FRAM), transducers and actuators, infrared detectors, and tunable microwave components [3, 29, 30]. In this work, the ferroelectric material is studied for agile microwave devices due to the DC field dependent dielectric constant.

Perovskite (ABO_3) based ferroelectric materials have been widely studied for microwave applications [3, 12, 30]. They generally have a non-linear dependence of polarization on an electric field as shown in Figure 2.4. Below T_C, the material is in ferroelectric phase, showing hysteresis behavior (Figure 2.4a) and the respective dielectric permittivity has a butterfly shape (Figure 2.4b) dependence on the DC-field. Above T_C, the material is in a paraelectric phase, thus no spontaneous polarization, and shows no hysteresis loop. However, the dependence of

polarization on the field is still non-linear (Figure 2.4c) leading to a bell-shaped dependence of permittivity on the applied electric field (Figure 2.4d). The DC field dependent dielectric constant (Figures 2.4 b&d) is what makes the ferroelectric material important for tunable microwave components.

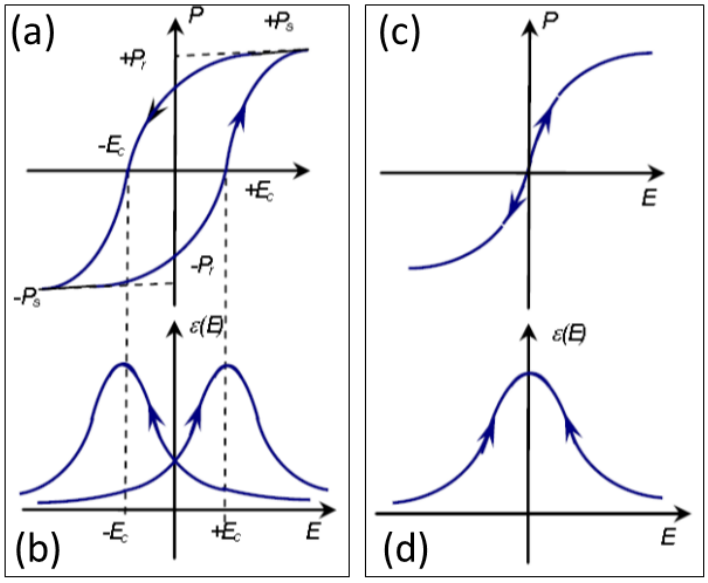

Figure 2.4. Polarization and permittivity (a&b) below and (c&d) above T_C vs. electric field [30]

In principle, for agile microwave applications, the ferroelectric material can be used both in the paraelectric and ferroelectric regions. However, when an electric field is applied to the material in the ferroelectric phase, the domain wall motion and piezoelectric transformation (because most ferroelectrics are piezoelectric) causes large dielectric losses. Consequently, for microwave devices, the paraelectric phase of the materials is highly recommended [3, 12].

2.2.3. Field Dependent Permittivity

As discussed above, the dielectric permittivity of a ferroelectric material is dependent on the applied electric field. This concept can be explained using the phenomenological theory also

known as the Landau theory of ferroelectricity, which is based on the Taylor expansion of the Helmholtz free energy, $F(P,T)$, [31] as a function of polarization, P,

$$F(P,T) \approx \frac{\beta}{2}P^2 + \frac{\gamma}{4}P^4. \tag{2.20}$$

In the expansion a small polarization was assumed and the contribution of the higher order terms was excluded. In addition, only the even terms were taken into consideration due to the fact that the free energy is independent of the polarization reversal [32]. The coefficients β and γ are known as the dielectric constant and non-linearity coefficients.

Using the equation of state ($\frac{\partial F}{\partial P} = E$) the electric field can be related to the polarization as

$$E = \beta P + \gamma P^3, \tag{2.21}$$

and used to define the relative permittivity of the material as

$$\varepsilon_r(E,T) = \frac{1}{\varepsilon_0}\frac{\partial P}{\partial E} = \frac{1}{\varepsilon_0}\frac{1}{\beta+3\gamma P^2}. \tag{2.22}$$

In a paraelectric phase with no externally applied electric field, the induced polarization is zero (i.e. P=0), thus $\varepsilon_r(0,T) = (\varepsilon_0\beta)^{-1}$. Assuming $P = \varepsilon_0\varepsilon_r(0,T)E$, for the condition under an externally applied electric field, Eq.(2.22) can be rewritten as [33]:

$$\varepsilon_r(E,T) = \frac{\varepsilon_r(0,T)}{1+3\gamma\varepsilon_0^3\varepsilon_r^3(0,T)E^2}. \tag{2.23}$$

This equation shows the dependence of relative permittivity as a function of applied electric field and temperature. At a constant temperature, the permittivity decreases with an applied electric field (tunablity), where the maximum is obtained at *E=0*—see Figure 2.4d.

Generally, for a given tunable dielectric (ferroelectric) material, a higher dielectric constant implies higher tunability [31] and occurs near the transition temperature. However, close to the transition temperature, owing to the distortion in the crystal structure, the dielectric loss of the material is also high. Therefore, it is always necessary to measure the tunability and

loss of the material at temperature safely far from T_C to obtain a trade-off between the tunability and dielectric loss.

2.2.4. Definitions

In this section parameters used to measure the performance of ferroelectric thin films for agile microwave components are presented. Tunability (*n*) is the measure of the change of dielectric constant with an external field [12, 31]; it can be described as the ratio of dielectric constant at no bias to dielectric constant at the maximum bias field, *E*, which is expressed as

$$n = \frac{\varepsilon_r'(0)}{\varepsilon_r'(E)}. \tag{2.24}$$

The tunability of a ferroelectric material can also be defined as the relative change of dielectric constant between the zero bias and maximum bias field, *E*, with respect to the zero bias value (thus, relative tunability) as

$$n_r = \frac{\varepsilon_r'(0) - \varepsilon_r'(E)}{\varepsilon_r'(0)} \times 100\% = \frac{n-1}{n} \times 100\%. \tag{2.25}$$

The use of ε_r' above indicates that the measured dielectric constant could be complex, but only the real part is used in the definition of tunability.

The other vital parameter used to characterize a tunable ferroelectric material is the dielectric loss. It is defined in the context of loss tangent, $\tan\delta(E)$, which is written as the ratio of the imaginary to real part of dielectric constant:

$$\tan\delta(E) = \frac{\varepsilon_r''(E)}{\varepsilon_r'(E)} = \frac{1}{Q(E)}, \tag{2.26}$$

where, *Q(E)* is the quality factor. The trade-off between tunability and dielectric loss is presented as the figure of merit (FOM) which is defined by the ratio of relative tunability to loss tangent as

$$FOM = \frac{n_r}{\tan\delta}. \tag{2.27}$$

2.3. Barium Strontium Titanate

Barium strontium titanate (BST) is a solid solution of barium titanate ($BaTiO_3$) and strontium titanate ($SrTiO_3$) which has been extensively studied for the tunable microwave applications [12, 34]. Barium titanate (BTO), one of the prominent ferroelectric materials, crystalizes to a perovskite structure (ABO_3) with the large Ba^{2+} cations situated at the corners of the cube (A-site), the O^{2-} anions on the cubic faces, and the smaller Ti^{4+} ion is at the body center of the cube. The oxygen ions sitting on the faces of the cube form an oxygen octahedral (O_h) cage within which the small titanium ion is located.

BTO naturally exists in four crystal states with the paraelectric-ferroelectric transition temperature (T_C) at ~120 ^oC [19]. Above T_C, the crystal structure of BTO is cubic, and exhibits a paraelectric phase. However, lowering the temperature below T_C transforms BTO into three ferroelectric phases whose polar axes are [100], [110] and [111] with respect to the cubic structure. At 120 ^oC, the crystal structure of the BTO transforms from cubic to tetragonal phase, leading to the first ferroelectric transition which is stable down to 0 ^oC. The second phase transition occurs at 0 ^oC, when the crystal structure transforms from tetragonal to orthorhombic phase. The material remains to be orthorhombic down to -90 ^oC where it undergoes the third phase transition by transforming to a rhombohedral crystal structure [35].

The properties of BTO as a function of temperature in its four crystal states are shown in Figure 2.5. Since all the transitions are first order, the polarization, permittivity as well as lattice constant experience discontinuities at the transition temperatures[22, 32, 35]. The sharp increase in the permittivity of BTO, close to T_C, is associated with the softening of the transverse optical phonon. According to the LST relationship (Eq. (2.18)), the dielectric constant of a ferroelectric material diverges as the transverse phonon frequency 'freezes out' at T_C.

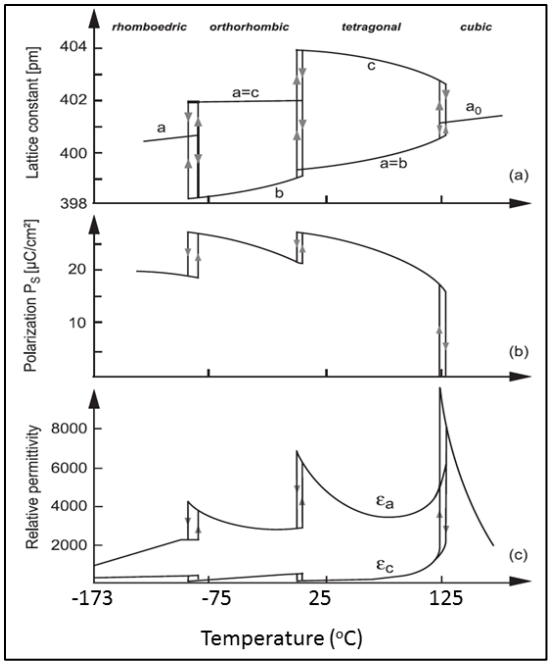

Figure 2.5. Properties of BTO as a function of temperature: (a) lattice dimensions, (b) spontaneous polarization, and (c) relative permittivity measured in the a and c-direction [22]

In contrast to BTO, strontium titanate (STO) remains paraelectric down to 0 K [36]. Such materials are called quantum paraelectrics since the crystal instability that occurs close to the transition point is stabilized by quantum fluctuation so that the material remains paraelectric [28]. Due to the presence of quantum fluctuation, the soft mode frequency of STO never freezes out and suppresses the onset of ferroelectricity as opposed to BTO. As the temperature approaches T_C, the dielectric constant of BTO diverges (Figure 2.5). However, in the case of STO, the dielectric constant rises only until it reaches a temperature low enough (~ 4 K for STO [37]) for the quantum effects to kick in and cancel out the ferroelectricity.

Given the importance of the paraelectric regime for tunable microwave applications, it is impractical to use BTO because of the high transition temperature (120 ^{o}C). Interestingly, the Curie temperature of BTO has been found to be easily manipulated by changing its composition [35, 39]. Figure 2.6(a) shows the change of the Curie temperature of BTO when Ba^{2+} is

substituted with Ca^{2+} or Sr^{2+}, and Ti^{4+} with Zr^{4+} or Sn^{4+} dopants [35]. Among these additives, the use of Sr^{2+} ion (introduced usually in the form of STO) is considered to be the standard method of lowering the Curie temperature of BTO.

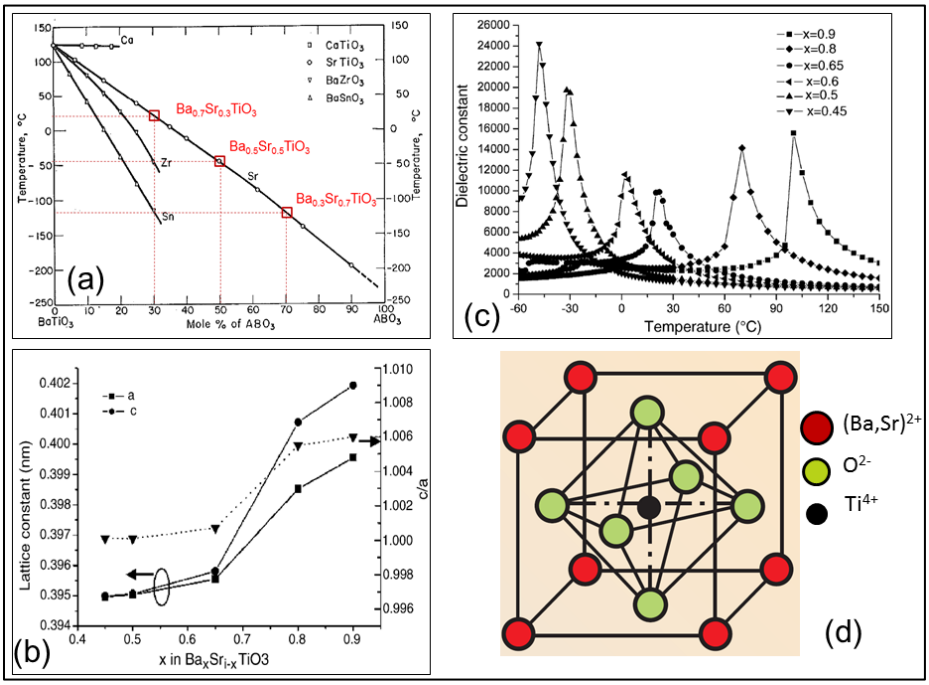

Figure 2.6. Dependence of the Curie temperature of BTO on various dopants (a) [35], change of the lattice constant with Sr concentration (b), temperature dependence of dielectric constant of BST (c) [38], structure of BST (d)

Substituting strontium (small cation compared to barium) for barium decreases the lattice parameter or the unit cell volume (Figure 2.6(b)) [38] and results in a linear decrease of T_C as shown in Figure 2.6(a). Besides, for high frequency application, the use of STO to tune the Curie temperature of BTO is a suitable choice because it has high dielectric permittivity, so that the dielectric constant and tunability remain high with the decrease of the Ba/Sr ratio [15].

The solid state reaction between BTO and STO results in BST, with the generic chemical formula of $Ba_xSr_{1-x}TiO_3$ (x, $0 \leq x \leq 1$ is the molar fraction of barium). As in BTO, BST crystalizes in a perovskite structure (Figure 2.6(d)) with Ba/Sr sitting at the corner and Ti in the octahedral

cage formed by the oxygen on the faces of the cube. Examples of BST with x=0.3, 0.5, 0.7 are marked in Figure 2.6(a), indicating that the Curie temperature of BTO reduces below room temperature when only 30 % of Ba is replaced with Sr. The change in the dielectric constant of BST with different molar fractions of Ba is shown in Figure 2.6(c). Due to the decrease in T_C with composition the peak position for the dielectric constant changes with the Ba/Sr ratio [38]. Therefore, the dependence of the Curie temperature of BTO on composition allows the tuning of the dielectric properties of BST as required.

2.4. Thin Film BST for Microwave Applications

In principle, any form of BST (bulk single crystal, ceramics, thick and thin films) can be used for applications in tunable microwave components [31]. Each of them, however, has advantages and drawbacks. At microwave frequencies, bulk BST offers low dielectric loss, but its applicability is limited by the requirement of a high tuning voltage (hundreds of volts to tens of kilovolts). The other source of concern in using bulk BST is the variation of its dielectric constant with temperature and incompatibility with semiconductor microelectronic circuits [40, 41]. On the contrary, the thin film form of BST is very attractive for microwave applications since it enables device miniaturization, and potential integration with semiconductor microelectronic circuits [12, 31]. Unlike bulk BST, the thin film BST requires a small tuning voltage (~ 20 V) and is inexpensive to grow on different types of substrates.

On the other hand, the dielectric properties of BST thin films have been observed to deteriorate compared to the bulk material—BST thin films have shown low dielectric constant but high dielectric losses [41-44]. For example, Figure 2.7 compares the dielectric constant of bulk and thin film (~100 nm) of the same composition, $Ba_{0.7}Sr_{0.3}TiO_3$ [41]. Though the composition of both forms of the BST materials is the same, the permittivity of bulk BST is

observed to be larger and strongly temperature dependent, with a sharp peak at the paraelectric-to-ferroelectric transition temperature. However, for the thin film, the dielectric constant is much lower (reduced by an order of magnitude), with no sharp peak, and has shown an almost temperature independent behavior. The temperature independent behavior of the film's dielectric constant is important because it indicates a much smaller temperature coefficient which allows the performance of a device over a wide range of temperature when compared to bulk BST material [15].

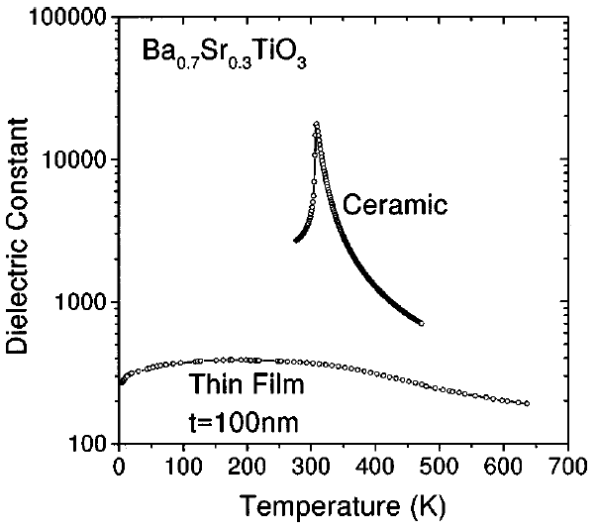

Figure 2.7. Permittivity of bulk and thin film $Ba_{0.7}Sr_{0.3}TiO_3$ versus temperature [41]

The degradation of the dielectric properties of BST thin films has been attributed to many reasons among which substrate induced stress [45], microstructural features including the charged defects (e.g. oxygen vacancies) and structural imperfections that are responsible for creating micro polar regions in the thin films [46], interfacial capacitance or a 'dead layer' with a very low dielectric constant at the substrate/film or electrode/film interfaces [47], and the stoichiometry of the thin films[48] are the major ones. Thus, understanding of these problems is crucial to improve the properties of BST thin films for the intended application. In the

subsequent section some possible pathways to mitigate the detrimental effects of the above mentioned factors on the properties of BST are discussed.

2.5. Pathways for Improving the Properties of BST Thin Films

The mismatches of film/substrate lattice parameters and coefficients of thermal expansion (CTE) induce residual stress into the film which will have drastic effect on the physical properties of the BST thin film. The residual stress typically hardens the soft mode frequency [44] which results in reduced dielectric constant and weakened ferroelectric properties of the film (LST relationship), leading to the reduction of tunablity. If the induced residual stress is large, the grown film may also crack or delaminate.

Selecting substrates whose lattice parameter and CTE are closely matched with the film is extremely important to grow a stress free film [49]. However, it is often very demanding to find a crystalline substrate with the desired lattice constant and CTE (see chapter 4). An alternative approach to mitigate the stress induced by the substrate is to grow a buffer layer (homogeneous or heterogeneous) between the BST film and the substrate [50, 51]. For instance, the lattice mismatch between a MgO substrate and a $Ba_{0.4}Sr_{0.6}TiO_3$ thin film was reduced by using a buffer layer of $Ba_{0.6}Sr_{0.4}TiO_3$ (lattice parameter higher than the film but lower than MgO) and the film shows improved dielectric constant and tunability [50].

Additionally, the film/substrate (electrode) interface may also exhibit a low-permittivity, non-tunable ‘parasitic’ like capacitor known as a ‘dead layer.’ Although the exact origin of the dead layer is controversial, the interfacial discontinuity affecting the polarization state of the film [47], the microstructure or the electronic properties at the interface [12, 52], the field’s penetration into the electrodes [53], and the surface charge traps at the interfaces [54] are

proposed to be the major causes. With the dead layer, the overall permittivity and tunability of the film reduces and the dielectric loss increases [55, 56].

The effect of dead layers was found to be diminished by using oxide electrodes with a close lattice match with BST [12, 57]. For example, in [57], a 200 nm $Ba_{0.7}Sr_{0.3}TiO_3$ thin film grown on a $SrRuO_3$ has shown a bulk like dielectric constant with a defined transition temperature as opposed to a film grown on a platinum electrode (Figure 2.7) [41]. However, the application of oxide electrodes for microwave varactors is limited owing to its high resistivity. Alternatively, the oxide electrodes may be used as a buffer layer between BST and the metal electrodes. The buffer layer may also be used as a seed layer to help grow crystalline BST thin film on a platinum coated substrate (Chapter 4).

The other difference between bulk and thin film BST leading to the degradation of the properties of the film is related to microstructural features. Thin film BSTs are characterized by small grain sizes and associated charged defects that are responsible for creating micro polar regions in the film [46, 58]. Since the volume of the dielectric polarization is proportional to the grain size, the BST thin film has a reduced dielectric constant [34, 58]. Similarly, the charged defects in BST film increase the extrinsic dielectric loss of the material [31].Therefore, suppressing the concentration of charged defects, such as oxygen vacancy is crucial in improving the loss and leakage current of BST. Optimizing the flow of oxygen gas during deposition, doping, and annealing films in oxygen atmosphere are some of the techniques that are used to reduce the number of oxygen vacancies [59].

The stoichiometry (i.e. Ba/Sr and (Ba+Sr)/Ti) ratio) of the deposited films often deviates from the desired values, especially in the RF magnetron sputtering process. Various studies have shown that BST films with the stoichiometric composition (Ba+Sr)/Ti~1.0) show high dielectric

constant and tunability. On the other hand, excess Ti in a BST thin film has the advantage of improving the dielectric loss, performance lifetime, and maximum resistance degradation while reducing tunability [42, 48, 60]. In order to control the stoichiometry of a BST film via RF magnetron sputtering one can use a non-stoichiometric target, deposit films under high pressure, and use an off-axis sputtering source [61-63]. Besides, it is critical to regulate the composition of Ar/O_2 to deposit a BST film with a closer stoichiometric match to the sources target without losing the phase purity (Chapter 5).

2.5.1. Doping Barium Strontium Titanate

The other method that can be used to effectively improve the properties of BST film is by incorporating foreign elements or dopants in the lattice of BST. The effects of dopants such as La^{3+} [64], W^{6+} [65], $Ce^{3+/4+}$ [66], Nb^{5+} [67], Mg^{2+} [68], etc., have been widely studied to improve the properties of BST. These dopants affect the property of BST either by substitution of cations in the BST lattice or precipitation at the grain boundaries to form a non-ferroelectric phase. Substitution is essentially limited by the solubility of the cations which can be grouped as aliovalent (donor or accepter) and isovalent dopant by comparing the valance of the dopant ion with the ion being replaced.

If the introduced dopants are below their solubility limit, they can modify the Curie temperature, the microstructure of BST films including the lattice parameters and grain sizes, and structural defects. Also, substitution reduces the number of oxygen vacancies (especially when aliovalent dopants are incorporated) and thus controls the insulating properties of the film. If the solubility limit is exceeded, the insoluble portions of the dopants form their oxides and settle either at the grain boundaries or within the bulk of the material. The property of the doped

BST film is then a composite of the low-non tunable dielectric constant oxide and high-tunable dielectric constant BST [12].

Discretely, most dopants are effective in improving either the tunability or dielectric loss of the BST thin films. For example, Mg^{2+} doped BST thin film exhibit a significantly improved dielectric loss and insulating property, but are accompanied by lower grain size, dielectric constant, and tunability [68]. The assumption is that Mg^{2+} ions behave as an acceptor dopant by substituting Ti^{4+} and weaken the ferroelectricity (typically by lowering the Curie temperature) of BST, resulting in a decrease of the dielectric constant and tunability. Conversely, the Mg^{2+} acceptors could prevent the hopping of electrons between Ti^{4+} to Ti^{3+} by neutralizing the donor action of the oxygen vacancies to lower losses and the leakage current [12, 68]. On the other hand, Nb^{5+} ions, also substituting Ti^{4+}, behave as donor impurities which affect the properties of BST in the opposite manner to the Mg^{2+} ions [67, 69].

To obtain the positive effects of both Mg and Nb ions, a careful co-doping of the two ions in BST material is required so that the concentrations of the two ions have a unique relationship that does not allow the domination of the effect of one over the other. Predominantly, as one of the properties that need to be improved is the leakage current of the film the co-doping must not introduce free carriers into the material, i.e. there must be neutrality compensation. Given both ions substituting Ti^{4+}, the neutrality compensation is realized when $[Mg''_{Ti}] = 2[Nb^{\bullet}_{Ti}]$ as was reported in [70]. In this work, the ions were introduced through barium magnesium niobate ($BaMg_{1/3}Nb_{2/3}O_3$) where the detailed study is presented in Chapter 6.

Furthermore, it is conceivable that doping BST with multiple (two, three, even more) impurities may help attain an acceptable trade-off between BST film tunability and loss. The critical issue, however, is identifying efficient dopants and determining their optimal doping

levels from a great deal of elements used as impurities for BST. In order to achieve this, the use of a conventional approach is undesirable due to the slow, expensive and rather unpredictable trial-and-error nature of the method. Alternately, the combinatorial materials synthesis methodology combined with high throughput characterization (HPC) have the potential to investigate the effects of a wide range of dopants on BST films [71, 72]. In this work, an RF magnetron sputtering based combinatorial method is implemented to determine the concentration of dopants (three dopants) that correspond to the optimum tunability and loss (Chapter 7).

2.6. Conclusions

In this chapter, topics that are relevant to the tunable dielectric and ferroelectric materials were reviewed. The solid state reaction between BTO and STO leads to the formation of BST whose dielectric properties can be regulated by its composition. For microwave applications, thin film BST has superior advantages but its properties are deteriorated due to residual stress, microstructure, dead layer and stoichiometric deviance. The pathways to mitigate these problems, including the use of a suitable substrate, buffer layer, controlling the composition of Ar/O_2 and doping were discussed. The use of concurrent and multiple doping to achieve a trade-off between loss and tunability were pointed out. Lastly, the need for a combinatorial method to rapidly determine optimal concentration of multiple dopants in a BST film was presented.

3. EXPERIMENTAL METHODS

In this chapter, the methods that are used for BST thin film deposition and subsequent characterization are presented. First, a short introduction to the commonly used deposition techniques, with emphasis on the radio frequency magnetron sputtering (used in this thesis), are summarized. Then, the basic principles behind the analytical characterization techniques, capacitor structure fabrication, and subsequent device characterization methods will be described.

3.1. BST Thin Film Deposition

Ferroelectric BST thin films can be fabricated by several deposition methods which may be generally classified into two main categories: chemical deposition and physical vapor deposition (PVD) methods. The chemical method can be further classified as chemical vapor deposition (CVD) and chemical solution deposition (CSD) while the PVD methods commonly used for BST deposition include sputtering and pulsed laser deposition (PLD). However, regardless of the method used in BST deposition, the process should be economical, scalable for industrial purposes; and the resulting film must have good thickness uniformity, a high degree of structural perfection, and controlled stoichiometry.

3.1.1. Chemical Deposition Methods

The fundamental principle behind any chemical deposition method is the need of a chemical reaction between starting precursors either in gas or liquid phase to make the required thin films. A class of CVD method that has been successfully applied for the deposition of BST is the metal-organic-CVD (MOCVD) [73-77]. In this process, a sufficiently volatile organometallic precursor containing the required cations (e.g. Ba, Sr, Ti) is evaporated and transported with a suitable gas onto the substrate. At the substrate, the precursor decomposes and

gives rise to the formation of the required thin film by eliminating the organic portion. MOCVD has advantages to deposit a film on a complex substrate geometries, to deposit an epitaxial thin film due to the molecular level reaction, and is suitable for deposition of multilayer thin films [11, 73, 75]. Moreover, a film with the intended stoichiometry can be obtained by careful mixing of the precursor and gas flow rates [78, 79]. However, the availability as well as stability of the volatile precursors along with the overall cost of the system, the high thermal budget requirement, and the thickness non-uniformity of the deposited thin films limits its widespread use for BST deposition.

The CSD method produces a film from a homogeneously mixed precursors according to the pre-selected film composition [73, 80]. It includes metal organic decomposition (MOD) [73, 81] and sol-gel [82] methods which typically uses a spin coating practice to deposit a film. The resulting thin film usually undergoes multiple heat treatment steps to realize a crystalline material [73]. The CSD method is inexpensive and is characterized by low processing temperature as well as short deposition time. Besides, it has the advantages of large area coverage, composition control, and easy incorporation of dopants with precursors (ensuring maximum homogeneity). However, thin films fabricated by the CSD methods often suffer from thickness non-uniformity, large surface roughness, cracks, and voids which lower both the dielectric constant and tunability of the BST thin films [12].

3.1.2. Physical Vapor Deposition Methods

PVD method is a technique whereby physical processes such as thermal evaporation, collision impact, and laser ablation are used to create gaseous (vapor) material from a solid source (target) to deposit a thin film. In general, the PVD method involves three consecutive steps to deposit a thin film from a solid source: (1) the solid source is converted to vapor form by

a physical means; (2) the vapor is transported from the source to the substrate across a region of reduced pressure; and (3) the vapor undergoes condensation on the substrate to form the thin film.

The two widely used PVD systems for BST deposition are the pulsed laser deposition (PLD) [83] and RF magnetron sputtering [12, 59, 84-86]. PLD relies on the interaction of a short laser pulse (fs-ps range) with a solid target to create a plume of material to be deposited on a nearby substrate. It has the advantages of replicating the composition of BST film close to the source material at a high deposition rate with low level contamination. However, when the laser pulse interacts with the source material, it creates micron size droplets and clusters which are deposited on the film leading to significant surface roughness. The droplets and clusters are formed mainly as breakaway of surface defects under thermal shock and splashing of liquid material due to superheating of the subsurface layers. Besides, PLD deposited films lack uniformity over a large substrate area (typically $1cm^2$ substrate is used) [33, 87].

3.1.3. Sputtering Deposition Methods

Sputtering is a suitable and relatively simple thin film deposition method with the advantages of excellent uniformity, high purity, and reproducibility. Moreover, it has a respected industrial record due to its scalability, compatibility with standard IC processing, and ability to deposit on large area substrates [33]. The process is based on the transfer of physical momentum and kinetic energy from ionized atoms (typically, Ar+) to the source material (target) as schematically shown in Figure 3.1. When the energetic incident ions transfer momentum to the target, they knock off atoms (i.e. sputtered atoms) which retain the same chemical and physical properties with the target. In a reduced pressure, the sputtered atoms deposit on the substrate and walls of the deposition system. For the success of the sputtering process, generating energetic

ions to sputter atoms from the target, and creating a reduced pressure for the sputtered atoms to move towards the substrate with less number of collisions are critical [88].

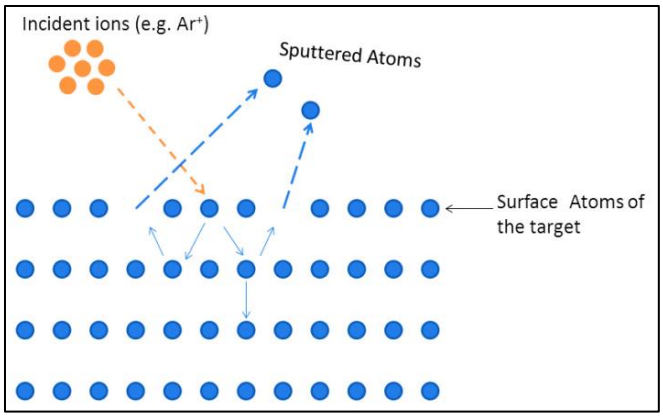

Figure 3.1. Schematics of sputtering processes

The sputtering method is generally divided into four classes: direct current (DC), radio frequency (RF), magnetron, and reactive sputtering methods. The simplest and oldest model of all the sputtering methods is the DC sputtering. In fact, the other sputtering systems are modified forms of DC sputtering in order to improve its efficiency and facilitate the depositions of non-conducting materials. The schematic representation of the DC and RF sputtering systems are shown Figure 3.2. The DC sputtering system consists of parallel cathode (water cooled) and anode electrodes on which target material and substrates are placed, respectively. Introducing sputtering gas (Ar) into an evacuated chamber and applying a high DC voltage across the two electrodes initiates the formation of a glow discharge (plasma), which constitutes electrons (e^-) and Ar^+ ions. The Ar^+ accelerates towards the target and generates sputtered atoms and secondary electrons by transferring momentum. The sputtered atoms pass through the plasma with enough energy and condense on the surface of the substrate [88-90]. The secondary electrons ionize more argon atoms to sustain the plasma discharge.

The DC sputtering system, however, is limited to the deposition of conducting materials. If the target material is an insulator or the deposition is performed in a reactive environment, the plasma between the two electrodes cannot be sustained because of an immediate buildup of positive charge on the surface of the target.

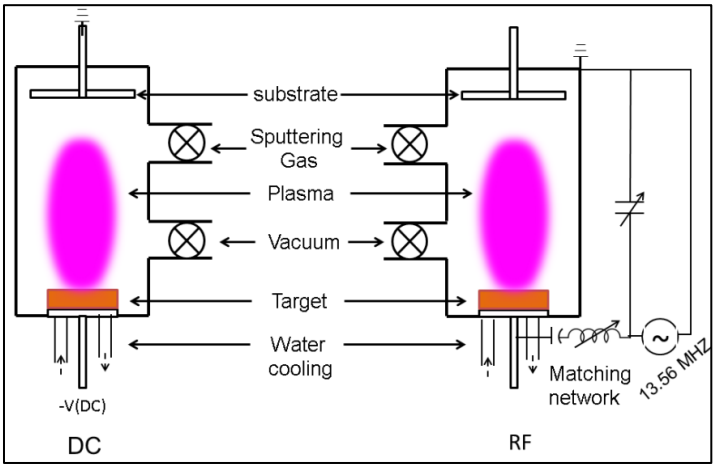

Figure 3.2. DC and RF sputtering systems [90]

The RF sputtering method was designed as a solution for deposition of insulating materials. In this method, a radio frequency range AC source (typically 13.56 MHz) is applied between the two electrodes using an impedance matching network which is coupled to the target material (Figure 3.2). As a result of the AC source, both electrodes reverse their polarity where only electrons are fast enough to switch their direction with the field, thus neutralizing the positive charge built on the target. On the other hand, the Ar^+ is too heavy to follow the RF cycle, and is always accelerating towards the target material (i.e. RF rectification effect). Therefore, RF sputtering uses the fast response of electrons to the changing polarity to sputter both the insulator and conducting materials in a reactive environment [91].

The third sputtering type which is widely used both for R&D and commercial applications with the primary advantage of obtaining a high deposition rate is the magnetron

sputtering method. In DC sputtering, some of the secondary electrons pass right through the plasma without ionizing argon atoms and get absorbed by the substrate or sputtering chamber. As a result, the sputter yield of the material reduces leading to the decrease in the deposition rate of the film. This problem is resolved by putting a magnet beneath the sputtering target, thus magnetron sputtering. The magnetic and electric field forces (Lorentz force) capture the escaping electrons and confine them to the vicinity of the target. This increases the ionization of argon atoms close to 100 % and thus the sputter yield of the material to increase the film deposition rate. Depending on whether a DC or RF source is used with the magnet, it may be called DC/RF magnetron sputtering [88].

The fourth sputtering is the reactive sputtering deposition. As its name indicates, this method involves a chemical reaction of some form at the surface of the substrate and is commonly used for deposition of oxide and nitride films. It can be done either from compound or a pure target under the flow reactive gasses such as O_2 and N_2 together with the sputtering gas [91].

3.1.4. RF Magnetron Sputtering for BST Deposition

The ferroelectric BST thin film deposition is widely conducted by a reactive RF magnetron sputtering system [86, 92, 93] which involves the mixing of oxygen and argon gas. One major difficulty of using RF magnetron sputtering to deposit a BST thin film is the challenge of choosing optimum deposition conditions to obtain a stoichiometric film. The BST film's stoichiometry is an extremely critical parameter which affects the dielectric property of the film. For instance, in numerous studies it has been shown that when the (Ba+Sr)/Ti ratio is equal to one, the BST thin film attains the maximum dielectric constant and tunability; however, an excess or deficiency of Ti decreases the former [42, 48, 60].

Unfortunately, when complex oxides like $Ba_xSr_{1-x}TiO_3$ ($0 \leq x \leq 1$, a multicomponent target) are sputtered in a reactive environment, the obtained film stoichiometry is off from the source material due to the mass and pressure dependent scattering processes [94]. Typically, for a sputter deposited BST film there is a high probability of Ti deficiency since it is the component with smallest mass that can be scattered over large angular range than Ba or Sr. Conversely, the heavy atoms (Ba/Sr) have low sticking coefficient to the substrate and are subsequently re-sputtered when the growing film is bombarded by negative oxygen ions [95]. The re-sputtering of Ba atoms from the grown film was observed in sputter deposited $YBa_2Cu3O_{7-\delta}$ (YBCO) thin film [96]. The stoichiometric control in sputter deposited BST thin film is studied in Chapter 5.

In this work, an advanced reactive (oxygen gas) RF magnetron sputtering system was used to deposit the BST thin films. It is a CMS-18 Series Kurt J. Lesker advanced system (Figure 3.3) available at the Center for Nanoscale Science & Engineering (CNSE) facility of North Dakota State University (NDSU). The system has three off-axis (targets shifted to the side) RF magnetron sputtering sources, where two of them are flexible (their tilt angles can be adjusted). Equipped with two vacuum chambers—load lock and process chamber which are separated by a valve, the system has a substrate bias (100 W RF source) for pre cleaning, capability of heating up to 1300 ^oC, and multiple source gasses (Ar, O_2, and N_2). Furthermore, it can deposit films on various substrate sizes, from small pieces up to 6 inch substrates, and has an ultrahigh vacuum performance which can reach a base pressure as low as $\sim 10^{-9}$ Torr. The flexibility of the RF sources makes it ideal for use in a continuous composition spread combinatorial thin film deposition (Chapter 7).

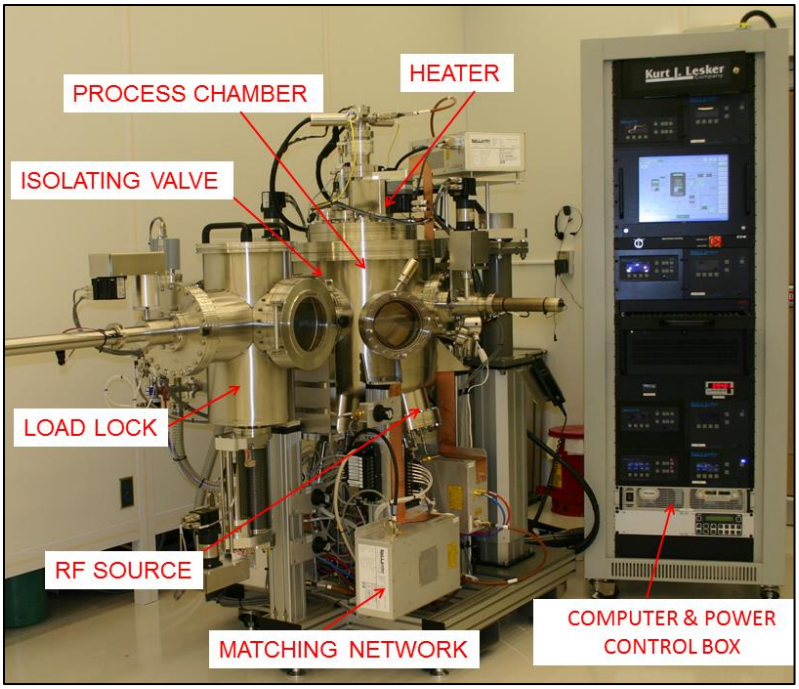

Figure 3.3. RF magnetron sputtering at CNSE, NDSU

3.2. BST Thin Film Characterization

The BST films were studied using various analytical and device characterization methods. The crystallinity, phase purity, and residual stress of the films were analyzed by x-ray diffraction (XRD). Raman spectroscopy was also exploited for a detailed study of the films' structure. The surface morphology, roughness, and grain structure of the films were examined by scanning electron microscopy (SEM) and atomic force microscopy (AFM). The film thickness including 3D mapping was measured by spectroscopic ellipsometery (J.A. Woollam, M88) and X-ray reflectivity (XRR) techniques. The elemental composition of the films was estimated by Rutherford backscattering spectroscopy (RBS), Inductively Coupled Plasma - Optical Emission Spectroscopy (ICP-OES) and X-ray fluorescence (XRF) techniques. The microwave and electrical properties of the films were conducted by lithographically fabricating parallel plate capacitor structures on the films and analyzing their DC- and AC-field responses.

3.2.1. Structural Characterization: X-Ray Diffraction (XRD)

X-ray diffraction (XRD) was used to characterize the crystallinity, phase purity, and residual stress of the BST films, powders, and sputtering targets. It is based on the interaction of an X-ray photon with electron clouds around an atom in a lattice. A crystalline material has a periodic arrangement of atoms in three dimensions which act as a 3D diffraction grating for the X-ray photons. When X-rays are diffracted from a crystalline material, the superposition between the diffracted waves could be either constructive or destructive. The constructive interference is produced when the path difference between the interfering waves is an integral multiple of the X-ray wavelength.

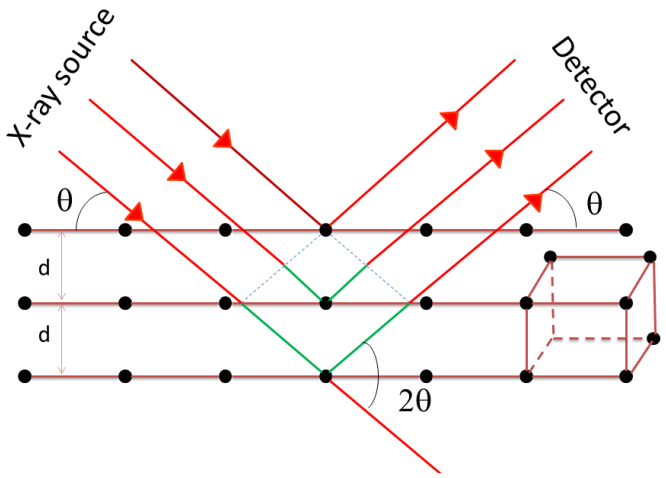

Figure 3.4. Schematics of X-ray diffraction

The schematic representation of the interaction between an X-ray radiation and a crystalline material is shown in Figure 3.4. The constructive interference is satisfied when the path difference (indicated by green lines) equals an integral multiple of the X-ray wavelength. This is governed by Bragg's law [97], $2d\sin\theta = m\lambda$ where, d is an inter-planar spacing, λ is the X-

ray wavelength, θ is the Bragg's angle, and m is an integer representing the order of the diffraction pattern.

The conventional Bragg-Brentano (θ-2θ) geometry can be used to analyze the crystalline properties of the BST powders and targets. However, for the analysis of thin films, the θ-2θ scan is not suitable since the X-ray penetrates through the film and probes the substrate. To suppress the signal from the substrate, using XRD in a grazing incidence XRD (GIXRD) mode is preferable. In GIXRD mode, the X-ray beam impinges onto the surface of the film at a small and constant incident angle (γ), which is close to the critical angle for total reflection, and the detector arm (2θ) rotates to collect the diffracted signal. The small grazing angle (γ, should be optimized) makes the incident beam evanescent, thus penetrates only into the top few nm of the surface of the film allowing suppression of the signal that arises from the substrate. In addition, the intensities of the X-rays are enhanced by 2-4 times at the surface compared to the intensities from the bulk [98, 99]. Therefore, the small penetration depth along with the intensity enhancement makes the GIXRD an ideal technique for the characterization of the crystallinity, phase purity and residual stress of thin films.

The XRD analyses in this work were performed using Rigaku Ultima IV X-Ray Diffractometer with a Cu Kα radiation generated at 40 kV and 44 mA. It has a multipurpose sample stage that can be switched between parallel and focused beam geometry, making it suitable both for the GIXRD and conventional XRD. The incident angle for the GIXRD was optimized to be 1.5^{o}. For the conventional XRD, the divergence, scattering and receiving slits were 2/3 mm, 2/3 mm and 0.3 mm, respectively. Similarly, for the GIXRD set up the divergence slit was 1.0 mm while both the scattering and the receiving slits were open. Phase identification was conducted with JADE 9.0 software equipped with the ICDD data base.

3.2.2. Surface Morphology and Roughness

The surface, grain type and size of the BST films were examined by scanning electron microscopy (SEM). In this technique an electron beam generated from a source (e.g. field emission gun) is focused on the specimen by electromagnetic lenses. These electrons interact with the surface atoms and provide information on the topography as well as composition of the sample. Imaging is typically done by detecting secondary electrons (electrons that emit from the specimen). The instrument used in this work was a JEOL JSM-6700F field emission SEM. It offers high lateral and vertical resolution and has the capability of imaging features down to 1 nm.

Similarly, a tapping mode atomic force microscopy (AFM) was used to study the surface morphology and roughness of the BST films. In this technique, a sharp AFM tip at the end of a cantilever is scanned across the surface of the sample and the cantilever deflection due to surface topography is detected. For the BST films analysis, a VEECO Dimension 3100 AFM equipped with 175 kHz silicon tip of diameter ~ 10 nm was used in a tapping mode. The surface roughness of the samples was extracted from the AFM images using the Nanoscope 5.31r1 software.

3.2.3. Elemental Analysis

The composition, stoichiometry, and dopant concentration of the BST thin film has a direct impact on the tunability, dielectric loss and leakage current of the film. Particularly, in a reactive RF magnetron sputtering method, a small change in deposition condition can significantly alter the stoichiometry of the BST film. Thus, monitoring the composition of the BST film is crucial. In this work, X-ray fluorescence (XRF), Rutherford backscattering spectroscopy (RBS), and Inductive coupled plasma-optical emission spectroscopy (ICP-OES) techniques were used for composition analysis.

Rutherford Backscattering Spectroscopy (RBS): Rutherford backscattering spectroscopy (RBS) is a quantitative analytical technique based on classical scattering in a central force field. It is insensitive to chemical bonding or electronic configuration of the sample. In RBS technique, a beam of monoenergetic (MeV range) particles (usually $^4He^+$ ions) is accelerated and collides with stationary atoms on the sample. In the collision process, the particles transfer some of their energy to the stationary atoms and scatter backward to the detector. The detector measures the remaining energy of the particles which depends on their mass and the mass of the target atom as [100]

$$E_1 = \left(\frac{\left(M_2^2 - M_1^2 \sin^2\theta\right) + M_1 \cos\theta}{M_1 + M_2}\right)^2 E_0. \quad (3.1)$$

Here, M_1 and M_2 are the masses of the incident particle and target atom, respectively, E_0 and E_1 are the energies of the particle before and after scattering, and θ is the scattering angle of the particle. Thus, the energy of the scattered particle measured by the detector provides the composition of the sample material. In this work, the RBS measurements were performed by a MAS 1700 pelletron tandem ion accelerator (5SDH) with a 165° fixed ion detector using 4MeV $^4He^+$ ions (University of Minnesota). The data analysis was conducted by SIMNRA 6.06.

Inductively Coupled Plasma-Optical Emission Spectroscopy (ICP-OES): ICP-OES is an analytical technique used to detect and determine the concentration of metals in various sample matrices. In this method, an inductively coupled plasma (ICP) is used to excite atoms that spontaneously emit photons as they relax to their ground states [101]. The emitted photons are detected by an optical emission spectroscopy (OES) detector and have characteristic energies (wavelengths) that correspond to the element they originate from. The intensity of the emitted photons is directly proportional to the concentration of the elements within the sample.

Liquid and gaseous samples can be directly injected into the instrument without further preparation, but the solid samples must be digested in a suitable solution so that the analytes will be present in a liquid form. In this work a Spectro Genesis SOP ICP-OES instrument equipped with optimist nebulizer and cyclonic spray chamber was used. The BST samples were prepared by digesting them in a mixture 10 % HCl, 45 % H_2O, and 45 % H_2O_2 heated to 60 ^oC.

X-ray Fluorescence (XRF): X-ray fluorescence (XRF) is a fast and non-destructive method for composition analysis. In the XRF process, a sample is irradiated with a primary x-ray source that has sufficient energy to eject electrons from the inner shells of the atoms in the sample, creating vacancies which induce instability to the atoms. The atoms then regain stability by filling the vacant shells with electrons from outer shells and giving off characteristic x- rays. These photons are detected to identify atoms and quantify their concentration (from intensity) in the sample. In this study, a ZSX Primus Rigaku x-ray fluorescence (XRF) furnished with wavelength dispersive spectrometry (WDS) was used. The WDS constitutes multiple analyzing crystals (typically single crystals or synthetic multiple layers of single crystals) which are used to diffract and then separate the characteristic photons generated from all the possible atoms in a sample prior to reaching the detector.

3.2.4. Device Characterization

In this section capacitor fabrication processes, dielectric and electrical characterization methods are discussed. BST thin film varactors are normally designed in two forms: parallel plate and coplanar type varactors as schematically shown in Figure 3.5. In the parallel plate design, the BST thin film is sandwiched between the bottom and top electrodes (Figure 3.5, left) forming a metal-insulator-metal (MIM) capacitor structure, whereas the coplanar geometry does not require the bottom electrode (Figure 3.5, right).

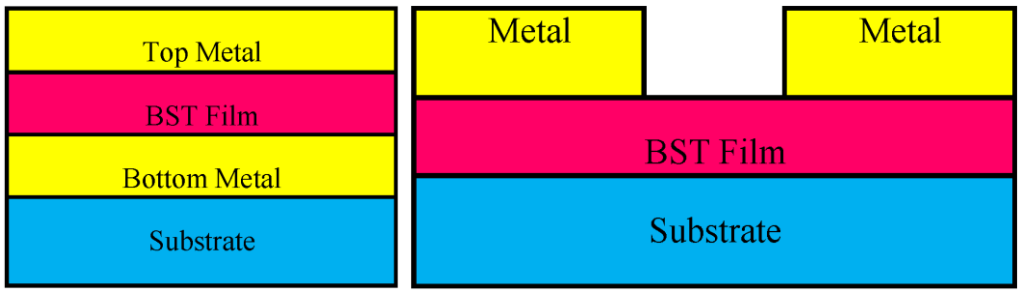

Figure 3.5. Parallel plate type (left) and coplanar type (right) BST varactors [30]

Since bottom electrode is not critical in a coplanar geometry, its fabrication is relatively simple. However, this design has several downsides, including low capacitance, reduced tunability, requirement of high tuning voltage due to the large gap between electrodes (typically $>1\mu m$), and the fringing nature of both the DC and RF fields in the air between the electrodes [30, 102, 103]. On the contrary, the MIM capacitor structure offers high capacitance density and tunability at lower DC voltages since most of the electric field lines enter the BST film (low fringing effect). Besides, the control voltage and power handling capability of the MIM capacitor structure is also good [30, 102, 103], despite the long and complicated processing steps.

Owing to the above advantages, the MIM capacitor structure was chosen to study the dielectric and electrical properties of the BST thin films. Similar to the coplanar capacitor structure, a single mask lithography process was applied to the top electrode to fabricate the MIM capacitor structure on the BST films [104, 105]. The bottom electrode remained inaccessible and acts as a continuous common ground for all the capacitors. Figure 3.6 (left) shows the mask layout used in the fabrication of the MIM structure. It consists of 2432 pairs of capacitors that are 0.2 mm apart and have a 0.5×0.5 mm^2 electrode area (see an optical microscopy image Figure 3.6, right). The detailed steps in the capacitor fabrication process are presented in appendix A.

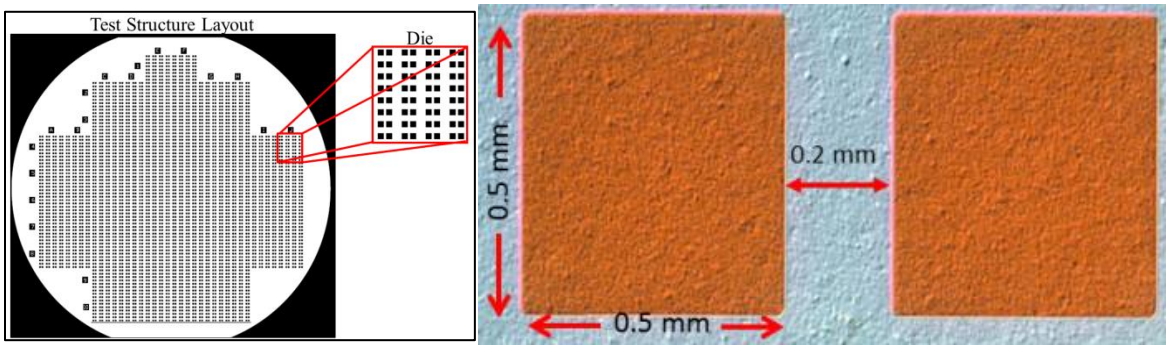

Figure 3.6. Mask layout (left) and a pair of MIM capacitor (right)

The measurement of capacitance (C) and loss tangent (tan δ) as a function of frequency and voltage was performed using a Cascade Microtech Summit 12000 Semi-Automatic Wafer Prober equipped with an Agilent E4991A RF impedance analyzer. The probe used in this experiment was a Picoprobe 40A-GS-500-C (GGB Industries Inc.) with 500 µm pitch (probe tip spacing). Unavoidable errors and losses in the impedance analyzer, its associated cabling and the probe were calibrated out using a CS-11 model calibration substrate.

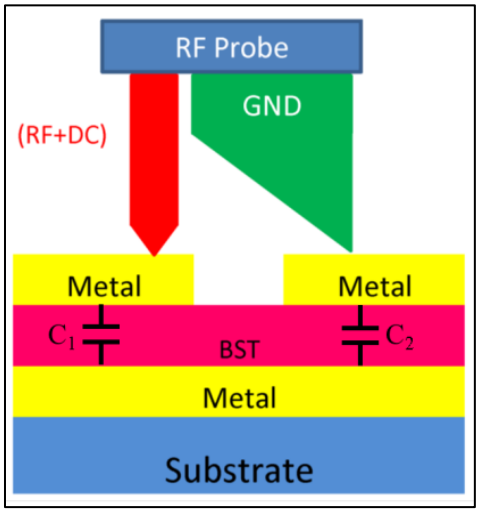

Figure 3.7. GS probe in contact with the two capacitors

To perform the measurement, the GS (Ground Signal) probe is put in contact with the pair of capacitors as schematically shown in Figure 3.7 and the impedance analyzer measures the equivalent capacitance of the two (equal) capacitors connected in series. The bias voltage was applied to the device under test by a Keithley 6487 Picoammeter/Voltage Source externally. The leakage current of the BST films was measured using an Agilent B1500A Semiconductor Device Analyzer.

3.3. Conclusions

MOCVD, CSD, PLD, and RF magnetron sputtering methods can be used to deposit ferroelectric BST thin film. In this work, an RF magnetron sputtering was selected owing to the advantages of excellent uniformity, high purity and its scalability to industry. Analytical techniques used in the BST film characterization, including XRD, SEM, XRF, etc. were discussed. The parallel plate and coplanar capacitor structures can be used for dielectric characterization; however, the parallel plate capacitor structure was chosen due to the high capacitance density, high tunability at lower DC voltage and good power handling capability.

4. SPUTTER TARGET AND FILM DEPOSITION

In order to use the RF magnetron sputtering method to deposit BST thin films, a BST source (target) with pre-determined composition is required. Generally, the BST target materials can be obtained either by purchasing from vendors or fabricating in house. Since a large number of targets (doped and undoped) were needed in this work, they were fabricated in house as it is cost effective and greatly flexible to produce targets with various compositions and dopants as needed. Selecting suitable substrates and optimizing the deposition temperature are also vital for BST thin film deposition. In this chapter, procedures in the fabrication of BST targets, selection of substrate to grow good quality BST film and determination of growth temperature are studied. Also, the need for a buffer layer to grow a crystalline BST thin film is studied.

4.1. Sputter Target Fabrication

In this thesis, three types of BST targets (two doped, two undoped) were fabricated using the traditional solid state reaction method between BTO and STO [38, 39]. The solid state reaction in general involves mixing of the starting powders with stoichiometric proportion, ball milling the mixture in a suitable medium, drying, calcining, and finally sintering (firing) at elevated temperature to promote a diffusion based reaction between the precursors. Figure 4.1 shows the flow chart for the fabrication of the targets. The process involves the synthesis of dopants (as needed), base BST powder, doped BST powder, and finally the target. Mixed precursors were milled at 60 RPM for 48 hours, and the subsequent slurry was dried at 50 ^{o}C for 24 hours in all the syntheses as needed.

For the doped BST targets, the impurities introduced into base BST powder were barium magnesium niobate ($BaMg_{0.33}Nb_{0.67}O_3$ (BMN)) and cerium oxide (CeO_2). The two dopants were introduced into separate base BST powder to fabricate doped BST targets with each of them. The

BMN dopant was intentionally used to introduce magnesium and niobium ions (aliovalent) in such a way that a complete charge neutrality is realized to minimize the dielectric loss and leakage current of the BST film without affecting its tunability [70].

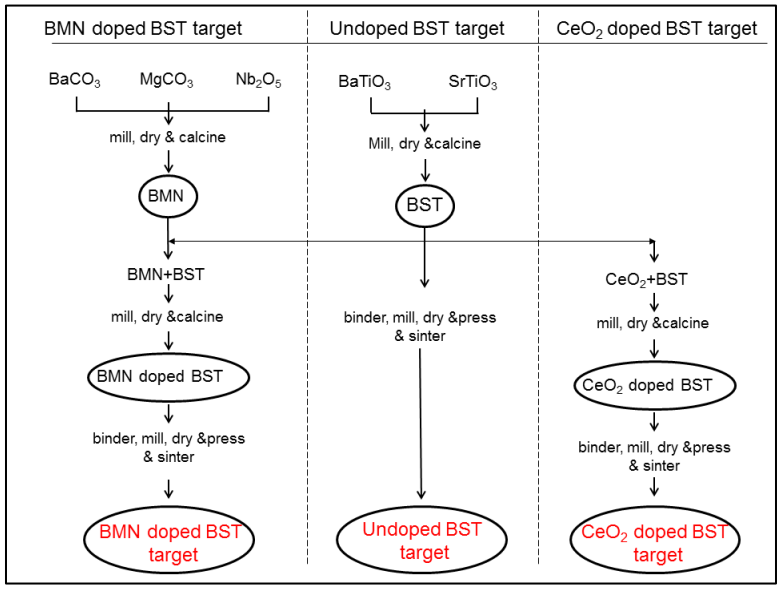

Figure 4.1. Flow chart for the fabrication of the sputtering targets

$BaMg_{1/3}Nb_{2/3}O_3$ dopant: The barium magnesium niobate (BMN) dopant was synthesized using a solid state reaction by closely following the preparation method presented in [106]. $BaCO_3$ (98.5%), $MgCO_3$ (99%), and Nb_2O_5 (>99%) were mixed and ball milled in ethanol. The slurry was dried and the resulting material was calcined at 1400 ^oC for 4 hours (Figure 4.1). After grinding and sieving the calcined material ($\leq$ 250 µm mesh) its phase purity was analyzed by powder XRD. Figure 4.2(a) presents the XRD pattern of the as synthesized BMN powder. The pattern has shown a hexagonal structure BMN material in agreement with the reported result [106],signifying the formation of complete solid solution between the precursors. The CeO_2 powder, however, did not require any further processing and was used as received.

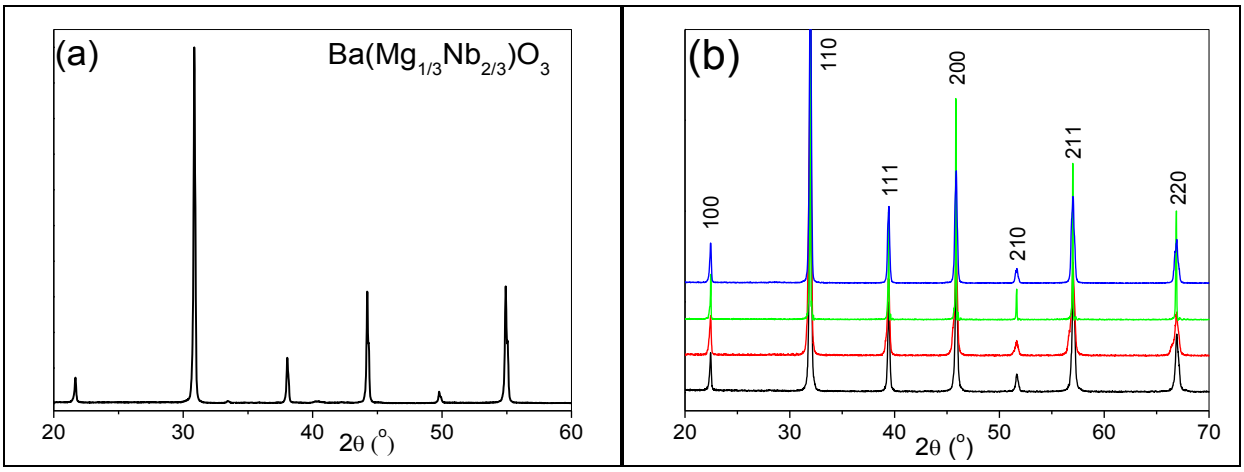

Figure 4.2. XRD patterns of (a) the synthesized BMN powder, (b) undoped BST powder (black), BMN doped BST powder (red), undoped BST target (green), and BMN doped BST target (blue)

Undoped (base) BST powder: Similar to the BMN synthesis, BTO (99.9 %) and STO (99 %) were mixed in a ratio of 9:11 to fabricate base BST powder with a composition of $Ba_{0.45}Sr_{0.55}TiO_3$. The mixture of BTO and STO was ball milled in ethanol and the subsequent slurry was dried. The dried material was calcined at 1300 ^{o}C for 24 hours and followed by grinding and sieving. Then, the phase purity of the resulting powder was examined by powder diffraction. The XRD pattern (Figure 4.2b, black line) has shown that the obtained powder is a pure phase BST with the intended composition [107], indicating a complete solid state reaction between BTO and STO. At this step, the BST powder can be used for the fabrication of the undoped BST target, but for the doped targets, an extra step of synthesizing the doped BST powder is required.

Doped BST powder: Following the synthesis of the base BST powder, 4 mol. % of BMN or an undisclosed concentration of CeO_2 (the concentration is proprietary) was weighed and mixed with base BST powder. Each mixture was ball milled and the subsequent slurry was dried. The two powders were then calcined at 1400 ^{o}C for 24 hours, ground, sieved, and the solubility of the dopants in the base BST was analyzed by XRD. The XRD pattern of the BMN doped BST

powder is presented in Figure 4.2b (red line). The pattern has shown no extra phase, suggesting the complete solubility of the BMN dopant in the BST lattice. A similar result was obtained for the CeO_2 doped BST (data not shown).

Sputter Targets Fabrication: After preparing the undoped and doped BST powders, 2 wt. % binder (Rhoplex) was added to each of them to facilitate the bonding between particles and the mixture was first ball milled in ethanol, and then dried for 12 hours, followed by grinding and sieving. To fabricate a standard sputtering target 160 grams of each powder was weighed and shaped into discs of ~3.5" diameter and 6 mm thickness using a uniaxial pressure of 30000 lb for 10 minutes. Then the BST discs (also known as green bodies) were sintered at high temperature to enable diffusion reaction between the components. The pure BST disk was sintered at 1430 ^{o}C for 3 hours while the doped BST discs were fired at 1600 ^{o}C for 6 hours.

The crystalline structure and phase purity of the undoped and BMN doped targets were analyzed by XRD and presented in Figure 4.2b, green and blue lines, respectively. The XRD patterns for both BMN doped and undoped targets have shown a cubic polycrystalline phase BST material [107]. This shows the phase purity of the fabricated BST target and complete solubility of the dopants in the BST lattices. Similar result was obtained for the Ce-doped BST target (data not shown). Finally, the targets were machined, metal bonded to promote conduction and used in the RF magnetron sputtering to deposit BST films.

Moreover, by taking a closer look at the XRD pattern, it is possible to see the entire evolution of crystal structure and lattice parameter of BST as the solid state reaction progresses. Figure 4.3 shows the (110) XRD line of BST (Figure 4.2b), BTO and STO. At room temperature, BTO has a tetragonal structure (black) and STO has a cubic structure (red). The

solid state reaction between BTO and STO creates a cubic phase BST whose XRD line (green) positions between the two, indicating that its lattice parameter is lower than that of BTO.

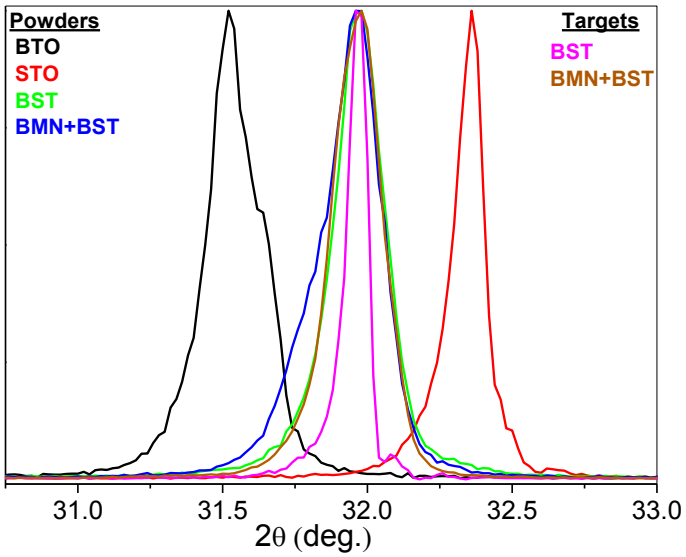

Figure 4.3. The (110) XRD lines for BTO (black), STO (red), undoped BST (green), BMN doped BST powder (blue), and undoped BST (magenta) and BMN doped BST (orange) targets

Interestingly, the doping of BMN into BST powder did not change its lattice parameter, but the full width at half maximum (FWHM) of the (110) XRD line has increased from 0.176^{o} to 0.249^{o}. For the BMN doped target, the FWHM has reduced to 0.183^{o} though it is still higher than the FWHM of the undoped BST target—0.086^{o}. This suggests that the introduced dopants distort the structure of BST without affecting its lattice parameter (3.953 Å).

4.2. Substrate Selection

BST thin films have been deposited on various substrates such as oxide single crystals, silicon wafers, ceramics, and metallized substrates [12, 33, 108, 109]. These substrates affect the properties of BST in different ways, even if the deposition condition and the thickness of the film are the same. This is due to the differences in the physical properties of the substrates with respect to BST. For example, a stress free and crystalline BST film can be grown on a substrate

that has identical CTE and lattice parameter with BST [110], suggesting the requirement of a careful selection of substrates. Table 4.1 presents some of the frequently used substrates and their parameters that make them essential for BST film growth [12, 33].

Table 4.1. Substrates (SC/PC-single/poly- crystalline) for BST film deposition

Substrate	Structure	Lattice Parameter (Å)	CTE (10^{-6} $^{o}C^{-1}$, at 20 ^{o}C)	Relative permittivity	*tan* δ (at10 GHz)
MgO	SC	4.200	12.8	9.8	2×10^{-5}
$SrTiO_3$	PC	3.906	9.4	~300	5×10^{-4}
$LaAlO_3$	SC	3.793	11.0	25	6×10^{-5}
Sapphire	SC	*a*=4.758, *c*=12.993	7.3	a:9.4 c:11.6	a:$<2\times10^{-5}$ c:$<5\times10^{-5}$
Al_2O_3 (99.6%)	PC	*a*=4.758, *c*=12.993	6.0-8.1	9.9	10^{-4}
Silicon	SC	5.431	2.5	11.9	…
Platinum	SC	3.924	8.9	…	…

Note: the lattice parameter of the undoped BST target is 3.953 Å, and the CTE for the composition of BST used in this work falls between 9-11ppm $^{o}C^{-1}$ [111].

Single crystal oxide substrates (e.g. MgO, $LaAlO_3$, sapphire, etc.) are exceptionally useful to grow an epitaxial BST film with a good crystalline quality. However, the use of these substrates is limited due to the high cost of available single crystalline wafers [33]. On the other hand, alumina (Al_2O_3, 99.6 %) and standard silicon (Si) substrates are cheaply available. Yet, the BST film grown directly on these substrates suffers from residual stress due to the mismatch between the BST and the substrates (Table 4.1). Therefore, the substrate selection is dictated not only by the quality of the grown film but also by its cost effectiveness.

The other important issue of substrate for BST is the selection of suitable bottom electrode. In BST deposition, the bottom electrode is more than an electrical contact; it can be used as a template to facilitate the growth of crystalline film. In general, any bottom electrode should possess the following three properties: (i) high electrical conductivity to minimize active

losses of the device, (ii) it must be inert to any chemical reaction at the film-electrode interface (e.g. oxidation), and (iii) it should be thermally stable to withstand the high BST deposition temperature.

Conducting oxides (e.g. IrO_2 and RuO_2) and noble metals (e.g. Au and Pt) have been used as bottom electrodes for BST film deposition [12]. The conductive oxides are advantageous because they withstand the high substrate temperature and oxygen atmosphere needed for BST deposition. However, they show high electrical resistivity which limits their use for BST thin film. The state-of-the-art bottom electrode for the BST varactor is Pt [105, 112, 113]. The suitability of Pt for the BST varactor arises from its properties that it is highly resistant to chemical reactions, thermally stable, and has good electrical conductivity. Conversely, Pt is highly permeable to oxygen [114, 115], and poorly adhesive to the substrates underneath it. The adhesion of Pt to the substrate is commonly improved by using a few nm of Cr or Ti layers. At high temperature, however, these metals diffuse and promote hillock formation in Pt layers, leading to shorted devices [115]. The problem is overcome by using the oxide forms of the metals (e.g. TiO_2) as an adhesion layer and an additional oxide diffusion barrier [116].

In this dissertation, SiO_2/Si, Pt/TiO_2/SiO_2/Si, and Pt/TiO_2/SiO_2/Al_2O_3 substrates were used. For the platinized substrates, the SiO_2 (~ 500 nm) and TiO_2 (20-50 nm) layers between the platinum and the main substrates (Si or Al_2O_3) are used to suppress diffusion and facilitate adhesion between layers, respectively. The SiO_2/Si (the SiO_2 layer could be native oxide, or deposited via thermal oxidation or PECVD method) substrates were mainly used to optimize the deposition conditions of the BST film. For the electrical characterization platinized substrates were used.

4.3. Film Growth Temperature

Regardless of the method used to deposit the BST film, growing crystalline film is critical to achieve optimal dielectric properties [48]. Particularly, in RF magnetron sputtering, the crystal structure of the BST film is affected by the deposition conditions, including substrate temperature, gas composition and total chamber pressure [33, 61]. While the effect of the latter will be studied in the next chapter, the optimum substrate temperature for obtaining crystalline BST thin film is presented here.

The substrate temperature influences the crystallinity of the grown BST film since it facilitates the mobility of sputtered atoms on the surface of the substrate. In search of an optimum substrate temperature, a series of BST films were deposited from an undoped BST target on six inch SiO_2/Si (100) substrates by varying the deposition temperature from 550 ^oC to 900 ^oC in an interval of 50 ^oC. For each deposition, the total chamber pressure, argon and oxygen gas flow rates were set to 5 mTorr, 60 sccm, and 40 sccm, respectively. The ellipsometery measurement has shown the thicknesses of the films ranging between 80 to 120 nm with good uniformity (~ 5%).

The crystallinity of all the deposited films was analyzed by XRD and their patterns are shown in Figure 4.4. At the lowest deposition temperature (550 ^oC), the grown film has shown poor crystallinity with only one broad peak corresponding to the (110) diffraction plane. However, when the substrate temperature increases, the crystallinity of the film improves. In addition to the dominant peak from the (110) diffraction plane two additional XRD lines were observed for the film deposited at 650 ^oC. At 700 ^oC, the film has shown all the expected patterns for cubic polycrystalline BST [107].

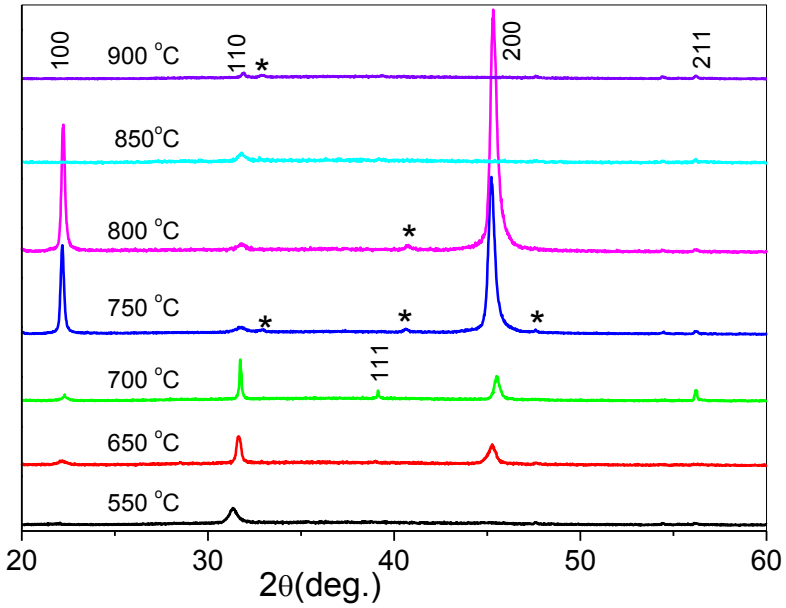

Figure 4.4. XRD patterns of films deposited at variable temperature—extra phases (*)

Interestingly, the films deposited at 750 ^{o}C and 800 ^{o}C have shown two strong XRD peaks corresponding to the (100) and (200) diffraction planes while the (110) diffraction line, which is the strongest peak for a polycrystalline BST, is suppressed. The patterns for both films indicate that they are grown preferentially following the (100) crystallographic plane of silicon substrate. The trend, however, was not maintained for temperatures above 800 ^{o}C. In fact, the films grown above the 800 ^{o}C temperature were of poor crystallinity, which might be related to the increase of oxygen vacancy concentration with temperature.

Despite the strong preferential growth, the films deposited at 750 C and 800 ^{o}C were observed to be contaminated with unintentional extra phases (see the asterisks on the graph). These extra phases may act as a low dielectric oxide mixed with a high dielectric BST and suppress the dielectric constant and tunability of the BST film [12]. Consequently, the optimum temperature selected to grow a polycrystalline BST thin film with no extra phase was 700 ^{o}C.

4.4. BST Self-Buffering

After determining the optimum deposition temperature (700 ^{o}C) it was used to deposit BST thin films on Pt/TiO_2/SiO_2/Si and Pt/TiO_2/SiO_2/Al_2O_3 substrates. During these depositions, as it was the case for silicon wafer, the RF power and the substrate temperature were simultaneously increased to their set points (i.e. 150 W and 700 ^{o}C).The substrate shutter was opened for deposition only after the temperature reached the set point. The crystallinity of these films was studied by grazing incidence XRD (GIXRD) and shown in Figure 4.5 (lines a&b). Unfortunately, as can be seen from the pattern, the grown films did not show any crystalline feature of BST on both substrates.

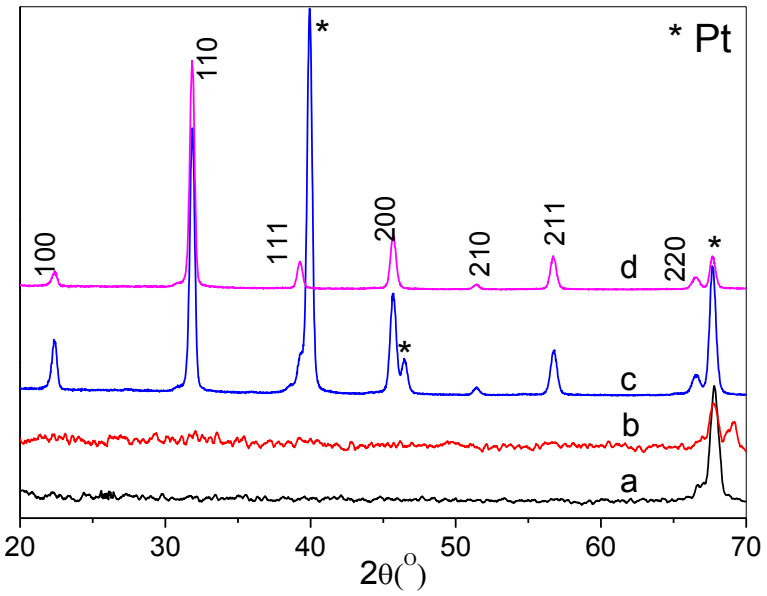

Figure 4.5. GIXRD for BST films deposited on platinized substrates (a,b) without and (c,d) with buffer layers. The Pt/TiO_2/SiO_2/Si is used in (a, c) and Pt/TiO_2/SiO_2/Al_2O_3 used in (b, d)

Doubting that the optimum temperature for BST deposition on SiO_2/Si may not be suitable for platinized substrates, several BST films were deposited at elevated temperatures in search of optimum temperature for platinized substrates. However, none of the grown BST films

have shown crystallinity (the XRD data are not shown), indicating that the Pt surface is not suitable to grow crystalline BST film. The XRD result has shown that despite the best properties that Pt exhibited as bottom electrode for BST, it cannot be used directly without any surface modification.

In an attempt to improve the properties of BST thin films different researchers have forwarded the idea of using buffer layers mainly to reduce the residual stress in the film and grow an epitaxial BST thin film [50, 51, 117, 118]. With this in mind, the $Pt/TiO_2/SiO_2/Si$ and $Pt/TiO_2/SiO_2/Al_2O_3$ substrates were first coated with ~10 nm BST layer (homo buffer) at room temperature. Then the substrate temperature was raised to 700 ^oC to deposit the main body of the BST film. Figure 4.5 (lines c&d) show the GIXRD patterns of the BST films grown on platinized substrates with the buffer layer. Interestingly, the GIXRD patterns of the films have presented all the diffraction lines expected of a polycrystalline BST material [107]. The result has shown a dramatic change in crystallinity of the BST film as a result of a homo-buffer layer coated on Pt surface at room temperature. The assumption is that when the temperature slowly (10 ^oC/min) rises to the set point, the thin BST buffer layer deposited at room temperature crystallizes and acts as a seed layer for the growth of crystalline BST thin film.

The surface morphology and quality of the films deposited on platinized substrates with a buffer layer was also studied by SEM (Figure 4.6). The film deposited on platinized silicon has shown bigger grains than the one on platinized alumina wafer; however, it suffers from cracks (Figure 4.6B). The possible cause of the cracks in the film deposited on platinized silicon substrate is due to the higher CTE and lattice constant mismatch between the BST film and the bottom silicon substrate as well as Pt and silicon layers (Table 4.1).

Conversely, the film grown on platinized alumina wafer is crack free (Figure 4.6A) due to the closer CTE match between alumina and BST as well as Pt. The large CTE mismatch leads to a large thermal stress (tensile in nature) resulting in film cracks [90]. Due to these cracks, the electrical measurements of the films on $Pt/TiO_2/SiO_2/Si$ substrate were not convenient since the devices were shorted out. Numerous experimental attempts to improve the cracking of the film on platinized silicon substrates were unsuccessful. As a result, electrical and dielectric measurements were performed only on platinized alumina wafers.

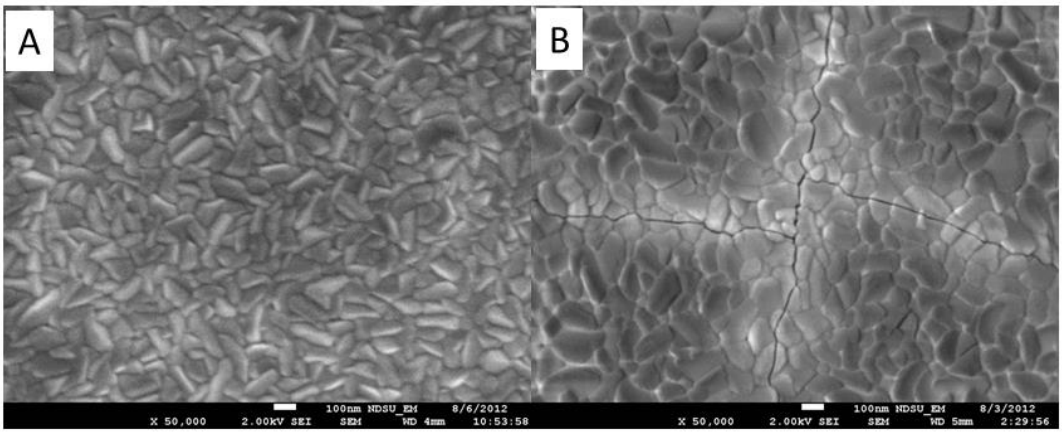

Figure 4.6. FESEM images of BST films on (A) $Pt/TiO_2/SiO_2/Al_2O_3$ and (B) $Pt/TiO_2/SiO_2/Si$

4.5. Conclusions

The standard ceramic reaction method was successfully applied to fabricate doped and undoped BST sputtering targets. The XRD study on the targets has shown that the introduced dopants have reduced crystallite sizes of BST without affecting its unit cell volume. The substrates used in this work were also selected by taking into consideration both the cost and the quality of the film grown on them. Accordingly, while SiO_2/Si was selected for optimizing the deposition conditions, $Pt/TiO_2/SiO_2/Al_2O_3$ was found to be suitable for the final electrical characterization. The optimum substrate temperature to grow polycrystalline BST thin film was

determined to be 700 ^{o}C; however, a crystalline film on platinized substrate was only possible by coating a 10 nm BST buffer layer at room temperature. The buffer layer would crystalize during the increase of substrate temperature to the final value and acts as a seed layer to grow crystalline BST film.

5. STOICHIOMETRY AND PHASE PURITY CONTROL OF BST THIN FILMS

BST thin films have been deposited by numerous techniques, including metal organic chemical vapor deposition (MOCVD) [75-77], metal organic deposition (MOD) [81], as well as physical vapor depositions, such as pulsed laser deposition (PLD) [83], and RF magnetron sputtering [59, 84-86]. The advantages and limitations of each of these methods were presented in section 3.1. Among these, RF magnetron sputtering is widely used to fabricate BST films both for research and in the industrial scale. It is a suitable and relatively simple deposition method with advantages of achieving uniform, highly pure, and reproducible BST thin film. However, one of the longstanding drawbacks of using the RF magnetron sputtering for BST deposition is to maintain a precise control of film stoichiometry [119].

In a numerous studies, it was shown that even small variations of BST film composition, stoichiometry, microstructure, and morphology can significantly alter its dielectric properties (tunability, loss and leakage) [120]. It was found that the highest dielectric constant can be achieved only when the y = (Ba+Sr)/Ti ratio in the BST film is close to unity, implying that the dielectric constant decreases when the film composition is either rich or poor in Ti [42, 60]. Up to 50 % decrease of BST film dielectric constant was observed due to a 10 % change of y ratio [121]. It was indicated that the drop in dielectric constant and tunability due to the y ratio reduction ($y < 0.85$) is accompanied by vanishing of the BST peaks in the film's XRD pattern [48] suggesting that the good film crystallinity is of paramount importance.

Several approaches have been proposed to control the complex oxide film stoichiometry: deposition using non-stoichiometric targets, the off-axis substrate-target orientation, elevated chamber pressure (up to 2.5 Torr), and their combinations [61-63]. Conversely, the stoichiometry of BST films and their dielectric properties can be finely tuned by variation of total (O_2+Ar)

chamber gas pressure (TGP) at fixed O_2/Ar ratio[48] or by changing O_2/Ar ratio at a constant TGP [122] enabling the tunability up to 93 % and loss tangent, tan δ, less than 0.01.

Another unusual property of sputtered BST thin films is the much larger lattice parameters of the $Ba_xSr_{1-x}TiO_3$ film material than those of bulk materials with the same stoichiometry (same x) [95, 107, 123]. Similar effect was observed in PLD fabricated films, and it was ascribed to the presence of large number of oxygen vacancies that reduce the Columbic attraction between cations and anions [83, 124]. However, with the increase of oxygen partial pressure (OPP) the lattice parameter has an overall tendency to decrease suggesting that the oxygen vacancies were partially annihilated.

For the RF sputtered films the increase of OPP in the deposition chamber at fixed TGP has a detrimental effect on BST film dielectric properties [122]. In contrast, effective increase of OPP with increase of TGP at fixed O_2/Ar ratio has the opposite effect on tunability [48]. The reason for these discrepancies remains unclear, partially due to the lack of detailed XRD structural analysis. In this chapter the effects of OPP and TGP on the crystal structure of RF sputter deposited BST films and their phase purity were systematically studied.

5.1. Experiment Description and Characterization

BST thin films were deposited from two undoped $Ba_{0.45}Sr_{0.55}TiO_3$ targets (fabricated according to the procedure in Chapter 4) on SiO_2/Si or platinized alumina ($Pt/TiO_2/SiO_2/Al_2O_3$) substrates. The base pressure, throw distance, substrate temperature, and RF power were set to 2×10^{-8} Torr, 16.5 cm, 700 ^oC, and 150 W, respectively. The total chamber gas pressure (TGP) and the Ar/O_2 gas composition were variable in the experiment. In order to grow good crystalline film, a self-buffer layer (~10 nm, Chapter 4) was deposited.

The crystallinity and phase purity of the films were characterized by XRD in grazing incidence X-ray diffraction (GIXRD) mode. The chemical composition of the deposited BST thin films was examined using Rutherford backscattering spectrometry (RBS) and Inductive coupled plasma optical emission spectroscopy (ICP-OES). Since RBS sensitivity to oxygen is poor, the Ba/Sr and (Ba+Sr)/Ti atomic ratio are used for BST films composition analysis. The dielectric and electrical measurements were conducted on films grown on $Pt/TiO_2/SiO_2/Al_2O_3$ substrate in a metal-insulator-metal (MIM) capacitor structure.

5.2. Oxygen Partial Pressure

To study the effect of oxygen partial pressure (OPP) on the properties of RF magnetron sputter deposited BST thin films, five films were deposited at a fixed total chamber gas pressure (TGP) of 5 mTorr, but variable Ar to O_2 flow rates. The Ar/O_2 flow rates were set to 90/10, 80/20, 70/30, 60/40, 50/50 (in sccm) leading to a variable OPP ranging between 0.5 to 2.5 mTorr in an interval of 0.5 mTorr. In this section, the effects of variable OPP at a constant TGP on the crystallinity and phase of the deposited BST films are studied.

The GIXRD patterns of the films deposited on SiO_2/Si substrates at OPP ranging from 0.5 to 2.5 mTorr are shown in Figure 5.1. All the observed XRD patterns are characteristic for the polycrystalline single phase cubic BST [107]. However, the peak positions of the films are shifted to lower 2θ value compared to those of the target (Figure 5.1, bottom black line) implying larger lattice constants than that of the deposition target (a_{target}=3.953 Å). Additionally, the XRD lines of the films are substantially broadened suggesting smaller crystallite sizes than that of the bulk BST target.

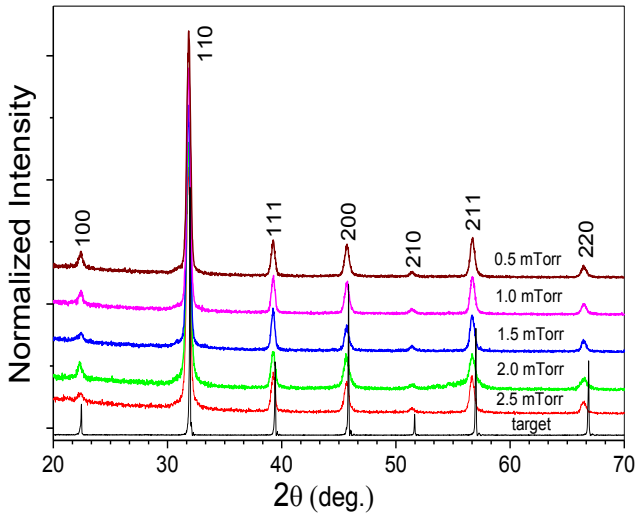

Figure 5.1.GIXRD of films deposited at 5 mTorr TGP and OPP ranging from 0.5 to 2.5 mTorr

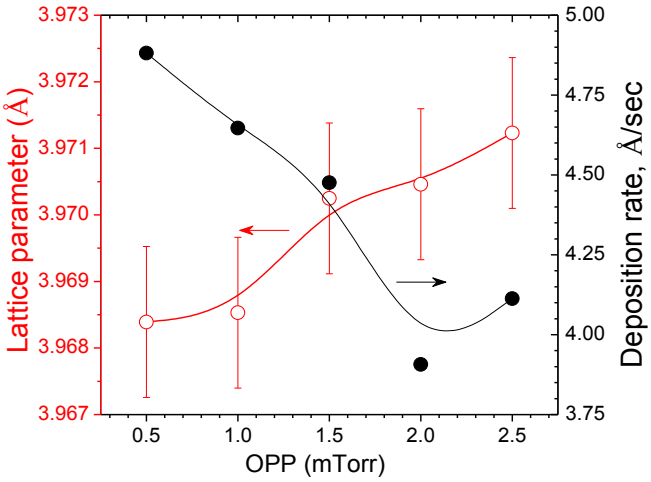

Figure 5.2. Lattice constant (o) and deposition rate (•) versus OPP

The film lattice parameters were evaluated using the Bragg's equation from the (110) diffraction plane [97] for each deposition, and plotted vs. the OPP in Figure 5.2 (–o–). Despite the relatively large error in the lattice parameter (~0.001 Å) the tendency toward its increase with increase of OPP is clearly observed. This finding contradicts the generally accepted idea [59, 83] that the increase of OPP in deposition chamber facilitates the oxygen vacancy healing, resulting in the shrinking of the BST film's unit cell closer to that of the target. Similar XRD peak position

shifts with increase of OPP (although not discussed) have been reported by other groups [125, 126].

Interestingly, the film deposition rate decreases almost linearly with the increase of OPP (Figure 5.2,–•–) in the chamber despite TGP (and other deposition conditions) remaining the same. Similar BST deposition rate reduction with OPP at a fixed TGP was attributed to oxygen ion bombardment of the growing BST surface [85]. It is known that the presence of oxygen in the chamber or target material may cause re-sputtering of the film by high energy oxygen atoms resulting in reduced deposition rate as well as surface damage [127-129].

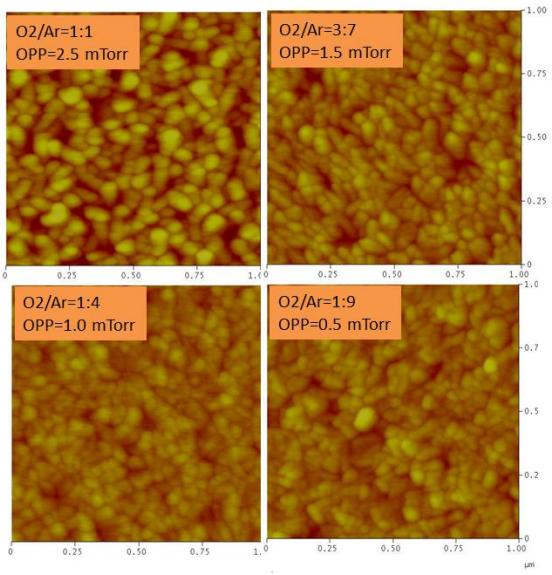

Figure 5.3. AFM images of the films deposited at 5 mTorr with variable OPP

The effect of OPP on the surface of the films was analyzed via tapping mode AFM. The AFM images taken from scan area of 1x1 μm^2 for each sample are shown in Figure 5.3 and the calculated surface roughness is presented in Table 5.1. With the increase of the OPP in the process chamber, the surface roughness of the films was observed to increase [125], verifying the presence of the bombardment of the growing BST surface by the highly energetic oxygen

ions. Therefore, the increase in the lattice parameter with OPP can be qualitatively explained in terms of the oxygen vacancies that are created as a result of the BST film surface bombardment by the negative oxygen ions [130, 131].

Table 5.1. Root mean square (RMS) surface roughness of the films at variable OPP

OPP (mTorr)	2.5	1.5	1.0	0.5
Ar:O_2	1:1	7:3	4:1	9:1
Roughness (nm)	4.33 ± 0.07	2.48 ± 0.09	2.22 ± 0.03	2.08 ± 0.01

To elucidate the effect of OPP on the BST elemental composition, which could be also altered by the negative oxygen ion bombardment, the elemental analyses of the BST films deposited at 5 mTorr TGP and variable OPP were performed using RBS and ICP-OES methods. The results in terms of Ba/Sr and y = (Ba+Sr)/Ti molar ratios are shown in Figure 5.4. Despite the slight underestimation of metal concentrations by RBS method, both analytical techniques have shown: i) a substantially lower Ba/Sr ratio with respect to that in the target material, which further decreases with increase of OPP; ii) an improving y ratio with OPP increase towards the optimal unity value. The decrease in Ba/Sr ratio with OPP indicates that the film has been further enriched with Sr. This behavior has been attributed to the lower sticking coefficient of Ba than Sr to the substrate during the sputtering process [95]. It is conceivable to assume that the bombardment of the growing BST surface with energetic oxygen ions could exacerbate the sticking problem of Ba, and therefore, decrease (albeit slightly) the Ba concentration in the films upon OPP increase. As mentioned above, the deviation of y below unity indicates that the thin film is Ti-rich. In this case the excessive Ti ions tend to form a low-permittivity amorphous TiO_x at the BST grain boundaries that may have a detrimental effect on the film tunability [42, 75]. Thus, the OPP increase substantially improved the y value (y = 0.99 at 2 mTorr OPP) and

potentially tunability, while the enrichment of the BST film with Sr may cancel this positive effect [132].

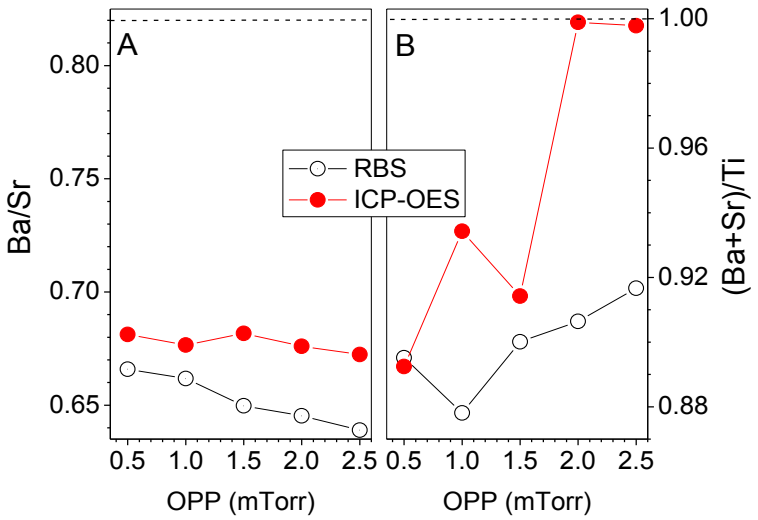

Figure 5.4. The Ba/Sr (A) and (Ba+Sr)/Ti (B) ratios vs. OPP for the BST films deposited at 5 mTorr TGP. The corresponding molar ratio values for the $Ba_{0.45}Sr_{0.55}TiO_3$ target (0.82 and 1.00, respectively) are shown as dashed lines

The ferroelectric transition temperature of BST shifts toward the lower temperatures with reduction of Ba content, *x*, shifting the permittivity maximum further away from the operational temperature (about 300 K). Since the tunability is the highest in the vicinity of the transition, its shift to lower temperatures may result in lower tunability at the operational temperature. The elevation of the TGP may help to suppress the oxygen and barium ions re-sputtering due to the BST film surface bombardment by the high energy oxygen atoms [48, 62, 63]. In what follows the effects of the TGP on the stoichiometry of the BST film are presented.

5.3. Total Chamber Gas Pressure

In this section five BST films were deposited by varying the TGP as 5, 10, 20, 30, and 40 mTorr and fixing the Ar/O_2 flow rates to 80/20 sccm or ($Ar:O_2$=4:1). The corresponding GIXRD patterns of the BST films deposited on SiO_2/Si substrates are shown in Figure 5.5. The XRD

patterns of films deposited at 5 and 10 mTorr TGP are consistent with those for the polycrystalline single phase cubic BST material [107]. In contrast, at 20 mTorr, extra phase(s) are clearly observed in the film GIXRD in addition to the anticipated BST phase. The peaks showing the secondary phases are positioned at 26.9°, 28.0°, 43.4°, and 48.8°. The search performed by the JADE software assigned these peaks to BaO_2, TiO, and Ti_2O_3 extra crystalline phases. The films deposited at 30 and 40 mTorr TGP have shown no peaks that could be assigned to any BST phase. It should be noted that despite a fixed Ar/O_2 gas flow ratio the increase of TGP is obviously accompanied by significant increase of the OPP (from 1 mTorr for 5 mTorr TGP up to 8 mTorr for 40 mTorr TGP). The XRD data analysis suggested that OPP > 2 mTorr facilitates the secondary phase (s) growth [132].

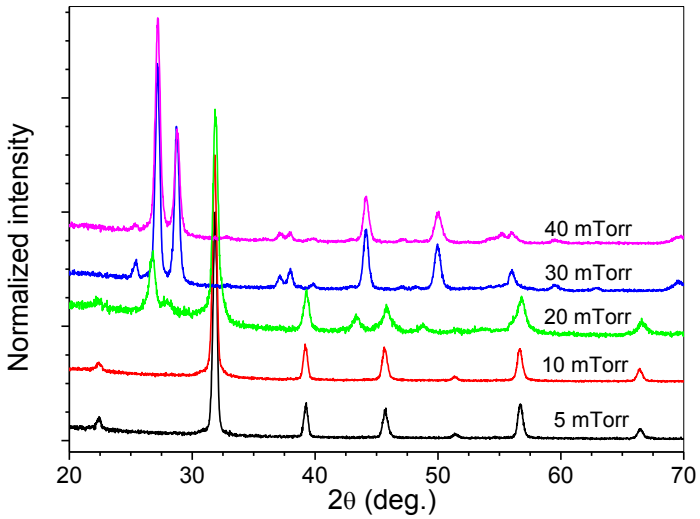

Figure 5.5. GIXRD of BST films deposited at TGP of 5, 10, 20, 30 and 40 mTorr at Ar/O_2 of 4:1

To verify this hypothesis BST films were deposited at TGP of 10 and 20 mTorr and Ar/O_2 flow rate ratios of 9:1 and 3:2 corresponding to OPP of 1 and 4 mTorr for 10 mTorr TGP; and 2 and 8 mTorr for the 20 mTorr TGP, respectively. The GIXRD patterns for the films deposited at 10 and 20 mTorr TGPs are presented in Figure 5.6A&B. The pure phase

polycrystalline BST film can be grown only when both TGP and O_2/Ar gas flow ratio secure the OPP of 2 mTorr or less. From this result, when OPP ≥ 4 mTorr, the grown film is either BST mixed with other phases (see the blue line for 10 mTorr TGP film, in Figure 5.6A, and red line for the 20 mTorr TGP film, in Figure 5.6B) or non-BST phase (see blue line in the 20 mTorr TGP film, Figure 5.6B). A summary of the obtained BST phase purity at the 10 and 20 mTorr TGPs but variable OPPs in the chamber is shown in Table 5.2. Therefore, exceeding 2 mTorr OPP in the chamber facilitates the growth of secondary phases at the expense of BST phase.

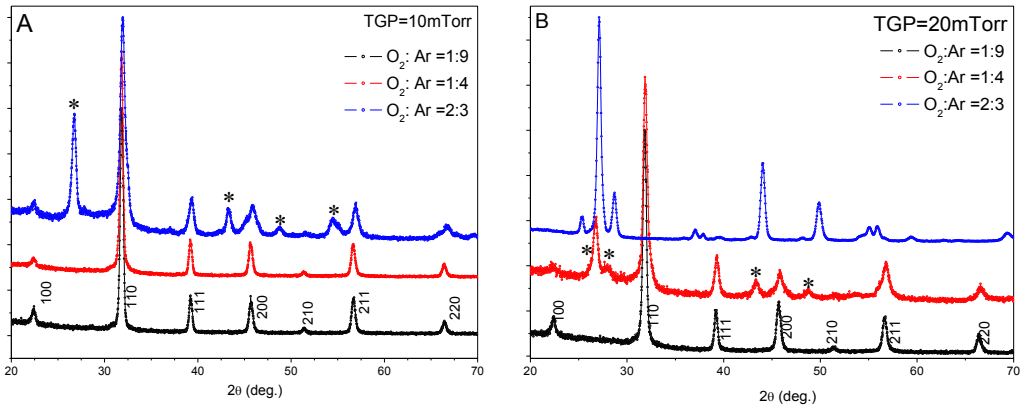

Figure 5.6. GIXRD of BST films deposited at TGP of 10 mTorr (A) and 20 mTorr (B) with variable O_2/Ar ratio. Peaks for the secondary phases are marked with an asterisk

Table 5.2. Summary of BST deposition conditions and phase purity

TGP, mTorr	O_2/Ar	OPP, mTorr	BST film phase purity
10.0	1:9	1.0	pure
	1:4	2.0	pure
	2:3	4.0	mixed phase
20.0	1:9	2.0	pure
	1:4	4.0	mixed phase
	2:3	8.0	non-BST phase

With the aim of obtaining an extra phase free BST film, another batch of depositions were performed at 5, 10, 20, 30, 40, and 50 mTorr TGP by fixing the OPP to 2 mTorr (identified

as a threshold OPP value). The GIXRD patterns corresponding to these films are shown in Figure 5.7. The XRD patterns of the films deposited at up to 30 mTorr TGPs are similar to that of a single phase polycrystalline BST. Conversely, at TGP > 30 mTorr the BST film XRD pattern is contaminated with other phases. In addition, the related BST peak patterns (at 40 and 50 mTorr) are shifted towards higher angles close to the position of the corresponding peaks in the target material (see Figure 5.7, inset).

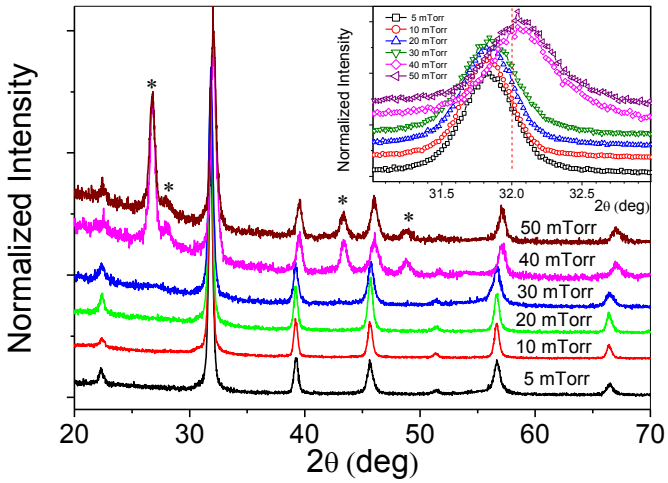

Figure 5.7. GIXRD of BST films deposited at TGP of 5, 10, 20, 30, 40, and 50 mTorr and fixed OPP to 2 mTorr. The secondary phase peaks are marked by asterisks. The inset are (110) plane peaks at different TGPs; a dashed line indicate (110) peak position of the target

Using the Bragg's equation and Scherrer's formula [97] the BST films lattice constants and crystallite sizes can be evaluated from the 2θ and FWHM values of the strongest (110) peaks, and their dependencies on TGP are shown in Figure 5.8A. For films deposited at TGP ≤ 30 mTorr very little, if any, lattice constant dependence on TGP is observed. However, above 30 mTorr, the film lattice constants abruptly decrease approaching that of the target material, implying a substantial improvement of Ba ions adhesion to the film surface. Unfortunately, some adverse contamination of the BST films with other phases as well as a decrease of BST

crystallite sizes suggest that the growth condition yet needs to be finely tuned. The deposition rate of the BST films deposited at variable TGP and OPP of 2 mTorr is shown in Figure 5.8B. The rate continuously decreases with increasing TGP most probably due to a decrease of sputtered particle mean free path with the increase of pressure in the chamber.

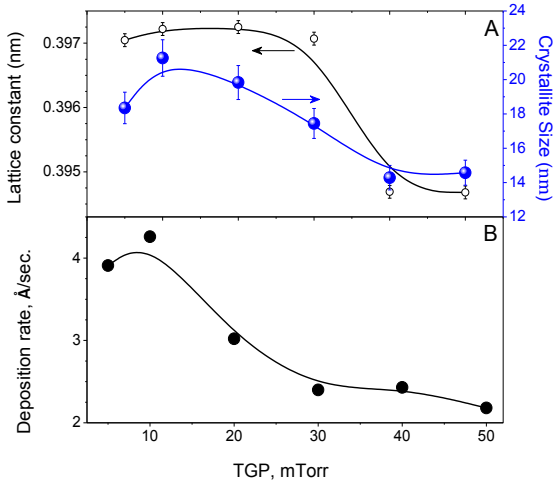

Figure 5.8. The BST film lattice parameter, crystallite sizes (A), and deposition rate (B) vs.TGP

To correlate the XRD data with the film elemental composition the ICP-OES analysis results in the form of Ba/Sr and (Ba+Sr)/Ti ratios as a function of TGP at fixed OPP of 2 mTorr are shown in Figure 5.9. As expected, the Ba/Sr ratio gradually increases with TGP and approaches the deposition target value of 0.82 at 30 mTorr. In contrast, the (Ba+Sr)/Ti ratio deviates from unity at 10 and 20 mTorr TGP suggesting the presence of oxygen vacancies. Very little change in lattice parameters at these TGPs despite the Ba/Sr ratio growth and anticipated lattice shrinkage indirectly confirm their (oxygen vacancies) presence. Above 30 mTorr TGP, the Ba/Sr ratio drops while the (Ba+Sr)/Ti ratio continues growing above unity in accord with the formation of secondary contamination phases at the expense of BST. Thus, at the deposition

conditions, TGP of 30 mTorr and OPP of 2 mTorr, a BST film close to the target material was realized, though some oxygen vacancies still may not be healed [132].

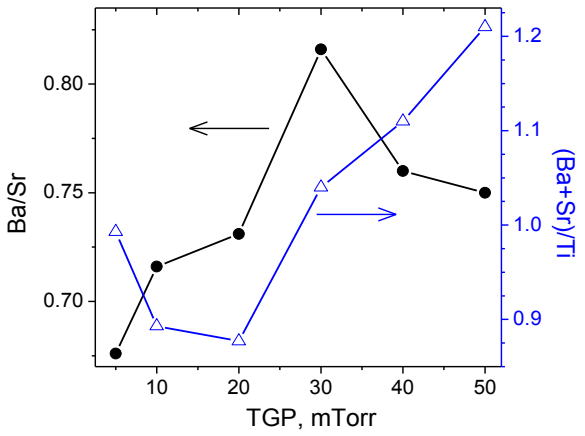

Figure 5.9. ICP-OES elemental analysis of the films deposited at variable TGP from 5 to 50 mTorr and at fixed OPP of 2 mTorr

5.4. Dielectric Tunability and Loss Measurements

To elucidate the effect of improved BST film stoichiometry, microwave dielectric property measurements were performed on two films (~250 nm) deposited at 5 and 30 mTorr TGPs on platinized alumina substrates. Both films were deposited at a fixed OPP of 2 mTorr to avoid the extra phase contamination. The results on the relative permittivity, ε_r, and loss tangent, *tan* δ, of two representative capacitors measured at 30 MHz vs. bias field are shown in Figure 5.10. At zero bias, the permittivity of the film deposited at 30 mTorr is about 30 % larger than that of the 5 mTorr film confirming that both the precise film stoichiometry and phase purity achieved via optimization of OPP and TGP have a significant effect on BST film dielectric properties. The studied films composition and dielectric properties are summarized in Table 5.3. The enhanced permittivity results in higher tunability; at 640 kV/cm bias the 30 mTorr film has

demonstrated tunability of 68.7% while that for 5 mTorr TGP film is only 61.4%. Conversely, no significant changes in the loss tangent of the 30 mTorr film were observed. It should be noted that the lattice parameters of the 5 and 30 mTorr TGP films are very close and larger than that of the source target.

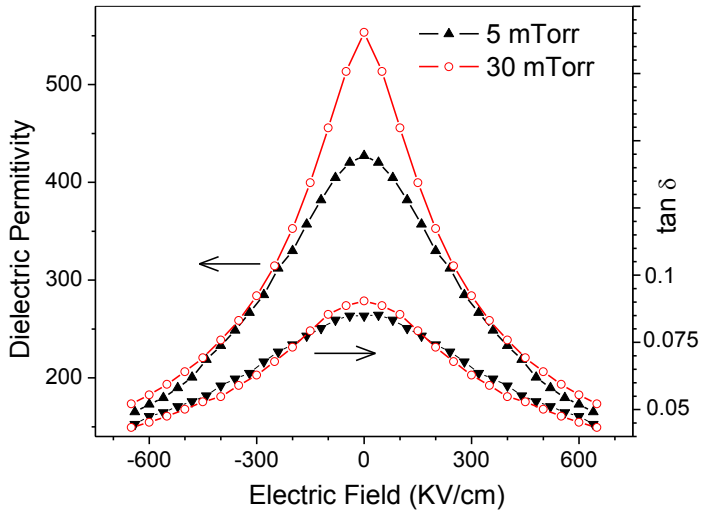

Figure 5.10. Relative permittivity, $\varepsilon_{r,}$ and dielectric loss, tan δ, vs. bias field for BST films deposited at 5 mTorr (open symbol) and 30 mTorr (closed symbol) TGPs, respectively

Table 5.3. Properties of BST films deposited at 5 and 30 mTorr TGPs and 2 mTorr OPP

TGP, mTorr	Ba/Sr	(Ba+Sr)/Ti	ε_r	η (30 MHz)	*tan* δ
5	0.68	1.00	427	61.4 %	0.045
30	0.82	1.04	553	68.7 %	0.043

It is conceivable to assume that despite achieving a desired stoichiometry at 30 mTorr TGP, this pressure is not enough to suppress the oxygen vacancies generation most probably via oxygen ion re-sputtering. The presence of oxygen vacancies are responsible for the formation of Ti^{3+} ions [12]. At high deposition temperature the corresponding equilibrium between the oxygen vacancy and Ti^{3+} ion in the crystal can be represented by the Kroger-Vink notation as

$$O_O^x \leftrightarrow V_O^{\bullet\bullet} + 2e' + \frac{1}{2}O_2, \quad (5.1a)$$

and

$$Ti_{Ti}^x + e' \leftrightarrow Ti'_{Ti}, \quad (5.1b)$$

where, O_O^x and Ti_{Ti}^x are the oxygen and titanium ions sitting on their normal sites with neutral charges, $V_O^{\bullet\bullet}$ and e' are the oxygen vacancy and free electron, and Ti'_{Ti} is the titanium ion sitting on its normal site with one negative charge in excess. The oxygen vacancy in the film generates electrons (Eq. (5.1a)) that reduce Ti^{4+} to Ti^{3+} according to Eq. (5.1b). The hopping of electrons between different Ti^{4+} ions most probably is one of the mechanisms that contribute to the dielectric loss in both films. Interestingly, the lattice constant of 40 mTorr BST film (despite the presence of secondary phases) is close to that of the target, suggesting the suppression of oxygen vacancies.

5.5. Conclusions

The effects of OPP and TGP on the stoichiometry, crystal structure, and phase purity of the RF sputtered BST films were studied. It was confirmed that the increase of TGP enables a better match of the film and target stoichiometry. However, the O_2/Ar ratio should be utilized cautiously since exceeding a threshold OPP (2 mTorr) may facilitate secondary phase formation. At 30 mTorr TGP and 2 mTorr OPP, a BST film with an exact compositional match to the target material was obtained and enhanced the permittivity and tunability ~by 30 % and 11 %, respectively, compared with the film with deviated composition. The presence of oxygen vacancies—confirmed indirectly by the deviance of the film lattice constant from that of the source target—was identified as a probable cause of losses. A further fine tuning of the OPP and TGP may still be necessary to significantly reduce the oxygen vacancy concentration.

6. CONCURRENT ACCEPTER AND DONOR DOPED BST THIN FILMS

In applying ferroelectric thin films of barium strontium titanate (BST) for tunable microwave devices, obtaining large tunability accompanied by low dielectric loss is vital [12, 31]. However, attaining both large tunability and low dielectric loss in parallel remains a challenge since large tunability is often followed by high dielectric loss and vice versa [83].

Numerous studies have shown that incorporating small amount of aliovalent (e.g. Mg^{2+} [68], La^{3+} [64], Al^{3+} [67] , Ce^{3+} [66, 133, 134], Nb^{5+} [67, 135]) or isovalent (e.g. Zr^{4+}, Sn^{4+}, Ge^{4+} [136]) ions into a BST lattice effectively modifies the dielectric properties (tunability and dielectric loss) of the BST film [137]. Mg^{2+} and Nb^{5+}, which are acting as an electron accepter and donor, respectively, by replacing the B site of the ($A^{2+}B^{4+}O_3^{2+}$) perovskite, have received the most attention because of their drastic effect in altering the dielectric properties of the BST film [67, 68, 79, 135, 138-140]. Individually, each ion improves either the tunability or the loss and insulating properties of BST film—not both at a time. Adding Mg^{2+} (~1-5 mol. %) suppresses the dielectric loss and the leakage current; but, these come with a huge drop in dielectric constant and tunability of the BST film [68, 79]. Conversely, introducing Nb^{5+} (~ 5 mol. %) increases the dielectric constant and tunability [69, 135, 138], however, these are accompanied by the increase of dielectric loss and leakage current, mainly due to the excess electron that Nb donates when it substitutes a Ti site [67, 139, 140].

Doping BST with Mg^{2+} and Nb^{5+} concomitantly may improve both the tunability and insulating properties of BST. One of the few studies in this area has shown that the leakage current was reduced to a minimum when a metalorganic deposited BST films is co-doped with Mg and Nb at the donor/acceptor compensated concentration[70]. Similarly, introducing barium magnesium niobate ($BaMg_{1/3}Nb_{2/3}O_3$ (BMN)), containing both Mg and Nb, into $BaTiO_3$ (BTO)

has significantly increased its dielectric constant [106, 141, 142]. BMN, by itself, is a complex perovskite oxide known to exhibit high dielectric constant, low dielectric loss, and a small temperature coefficient that makes it a material of interest for communication satellite and radar detector applications [143]. When used as a dopant, it ensures the total charge neutrality (realized when $[Mg''_{Ti}] = 2[Nb^{\bullet}_{Ti}]$), a desirable condition to obtain the minimum leakage current in the BST film [144].

This chapter addresses the effect of concurrent Mg/Nb co-doping on the structure, microstructure, residual stress, dielectric and electrical properties of the BST films. The $BaMg_{1/3}Nb_{2/3}O_3$ (BMN) doped and undoped $Ba_{1-x}Sr_xTiO_3$ (x=0.55) thin films were sputter deposited on platinized alumina ($Pt/TiO_2/SiO_2/Al_2O_3$) wafers from the respective targets. During the deposition of each film, the base pressure, throw distance, substrate temperature, and RF power were set to 2×10^{-8} Torr, 16.5 cm, 700 ^{o}C, and 150 W, respectively. The Ar/O_2 was chosen to be 60/40 sccm to produce a TGP of 5 mTorr, ensuring the 2 mTorr OPP (threshold OPP to grow pure phase BST). The thickness of both films was measured from five spots (center, left, right, top, and bottom) on each wafer by ellipsometer and averaged to be ~ 250 nm with a reasonably good uniformity (~1.4 %) across each wafer. The uniformity was achieved by rotating the substrates at 20 RPM during the deposition. Out of the total 250 nm thickness, 10 nm is a BST self-buffer layer grown at room temperature to improve the crystallinity of the films (Chapter 4).

6.1. X-Ray Diffraction Analysis of the Films

The grazing incidence XRD (GIXRD) patterns of the BMN doped and undoped BST films deposited on $Pt/TiO_2/SiO_2/Al_2O_3$ substrates are shown in Figure 6.1. The XRD patterns of the doped and undoped BST targets are also included in the graph for comparison purposes. For

both doped and undoped films, the patterns are characteristics of the perovskite cubic polycrystalline phase BST thin film [107]. However, the diffraction peak positions of the films are substantially shifted to the lower angles compared with those for the corresponding targets (see in Figure 6.1c&d), indicating that the films' lattice parameters are larger than that of the targets. The inset in the graph shows the shift of the films (110) diffraction plane peak position compared to that of the targets. The observed shift in peak positions of the films may be attributed to the deviation of films' composition from the target, and the presence of residual stress and oxygen vacancies in the film [123].

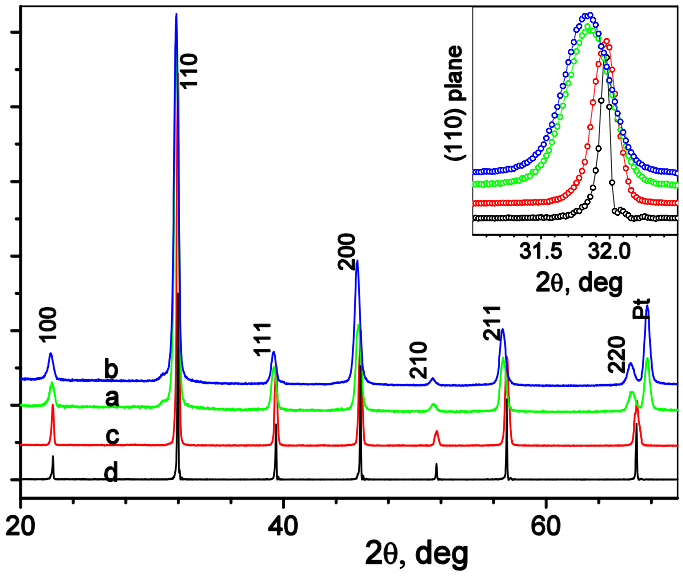

Figure 6.1. GIXRD patterns of undoped (a) and BMN doped (b) BST films; XRD patterns of undoped (d) and BMN doped (c) BST targets. Inset: the (110) peaks in a larger scale

6.1.1. Effect of Stoichiometry on the XRD Peak Shift

It is known that the lattice parameter of BST decreases when the concentration of strontium increases (or the ratio of Ba/Sr decreases) [123] due to the smaller radius of Sr than Ba. The left shift of the films' peak positions compared to the targets suggests that the films are barium rich. To prove or disprove this, the stoichiometric composition of the undoped BST film

and target material were analyzed by Rutherford backscattering spectroscopy (RBS) [48] and Inductive coupled plasma-Optical emission spectroscopy(ICP-OES). For the undoped BST target, the ICP-OES elemental analysis showed that the Ba/Sr and (Ba+Sr)/Ti ratio are 0.82 and 1.0, respectively, which are the same as the theoretical values. Since platinized substrates are not very suitable for RBS analysis due to the Ti, Sr, Ba and Pt signal overlap, the undoped BST film was deposited on a Si wafer covered with ~500 nm of amorphous SiO_2 using the same deposition parameters as for the platinized alumina substrate case. The GIXRD patterns of the films deposited on platinized alumina and Si wafers were practically identical.

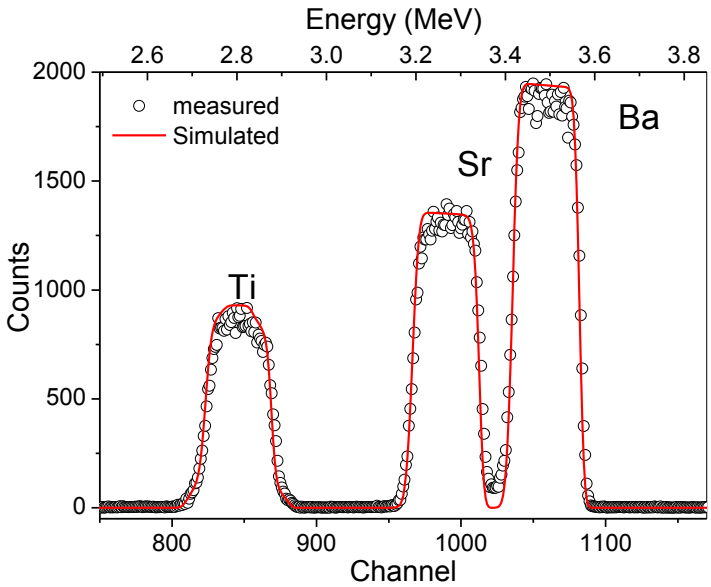

Figure 6.2. RBS spectrum for the undoped BST thin film deposited on SiO_2/ Si substrate

Figure 6.2 shows the measured and simulated RBS data for the undoped BST thin film. The RBS analysis revealed three intense and well resolved peaks with abrupt edges corresponding to Ti, Sr and Ba components indicative of structures with a sharp interface between the film and substrate [68]. The data obtained from the RBS were analyzed using SIMNRA simulation software [145] with the detector resolution set to 18 keV. The experimental

data are best fitted with the simulated one (see Figure 6.2) when the Ba/Sr and (Ba+Sr)/Ti ratios are 0.64 and 0.92, respectively. Similar analysis on the film by ICP-OES have shown the Ba/Sr and (Ba+Sr)/Ti ratios of 0.68 and 0.99, respectively, which is within the experimental error compared to the result obtained from the RBS data. The result from both analyses indicates that the BST film is more strontium rich than the target material. With this composition, the film is expected to have a lattice parameter lower than the target it is deposited from [123], and the XRD lines of the BST thin film should have been shifted to the higher angular position as compared to the target. However, the observed BST lattice constant of the film is about 1 % larger than that expected for the bulk BST with the obtained Ba/Sr ratio [95], implying that other factors such as stress and oxygen vacancies should be examined.

6.1.2. Residual Stress in BST Thin Films

The analysis of residual stress built in BST film has great technological importance because it has detrimental effects on the mechanical, optical, and electrical properties of the BST film. Studies have shown that a residual stress in BST film induces the hardening of the soft mode frequency, which drastically affects the ferroelectric phase transition of the material, and reduces the dielectric constant of the film[12, 41, 44]. In extreme cases, the residual stress can result in cracking (tensile stress) or buckling (compressive stress) and influences the performance, reliability, and life time of ultimate devices made from the BST film [146].

Residual stress in thin film can be evaluated by numerous techniques such as curvature method, Raman spectroscopy, and X-ray or neutron diffraction methods [147]. Among these, the X-ray diffraction method is widely used for determining residual stress built in a crystalline material. The residual stress built in both undoped and BMN doped BST films was calculated using the $g\text{-}sin^2\psi$ method [148, 149] which is suitable for the grazing incidence angle XRD

(GIXRD) pattern. The method relates the stress modified lattice parameter of a film to a biaxial residual stress, σ, by the following equation:

$$a = a_0\sigma\left(\frac{1+\upsilon}{E}\right)sin^2\,\psi + a_0\left(1-\frac{2\upsilon\sigma}{E}\right), \tag{6.1}$$

where, $a_{0,}$ σ , E, and ν are the stress free lattice parameter, residual Stress, Young's modulus, and Poisson ratio of the material (BST). The angle ψ is defined as the difference between the Bragg angle, θ_{hkl}, and the constant grazing incident angle, γ as

$$\psi_{hkl} = \theta_{hkl} - \gamma. \tag{6.2}$$

Calculating the lattice parameters from all the Bragg angles of the corresponding (*hkl*) planes and plotting them vs. $\sin^2\psi$, an unstressed lattice parameter (a_0) and the residual stress (σ) can be estimated from the slope $\left(\frac{\partial \mathrm{a}}{\partial \sin^2\psi}\right)$ and intercept of the linear fit.

To evaluate the residual stress in both films, five diffraction peaks (Figure 6.1) corresponding to (110), (111), (200), (210) and (211) were used. Accordingly, the calculated lattice parameters versus $\sin^2\psi$ graph fitted linearly for BMN doped and undoped BST films are shown in Figure 6.3. The positive slope for both films indicates they experience a tensile residual stress [148-150]. Using the Young's modulus and Poisson ratio of 107 GPa and 0.3, respectively [151], for the BST material, the residual stress, and stress free lattice parameter (a_0) for both films are estimated and presented in Table 6.1. Interestingly, the residual stress although relatively small for both films is notably lower in the undoped BST film than in the BMN doped film.

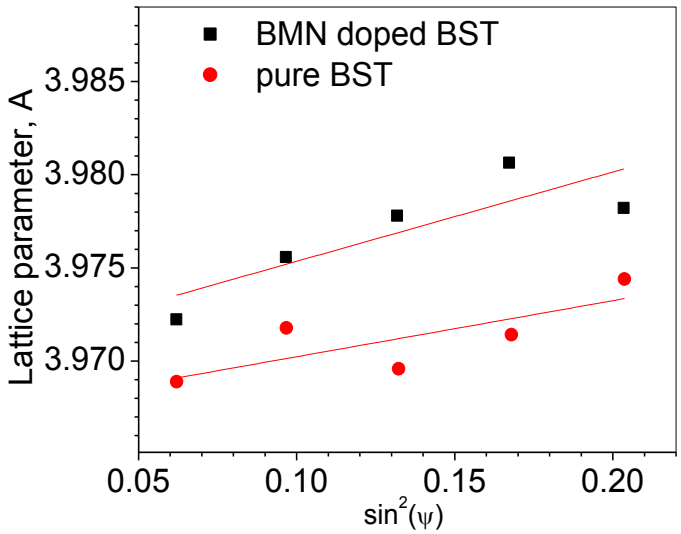

Figure 6.3. Lattice Parameters vs. $\sin^2\psi$ (g- $\sin^2\psi$) for the undoped and BMN doped BST thin films deposited on platinized alumina substrates

Table 6.1. Total residual stress, grain sizes and thermal stress in the BST films

Samples	Residual stress, MPa	Stress free lattice parameter, nm	SEM grain size, nm	Thermal stress, MPa	
				BST/Pt	BST/Al_2O_3
BST	138 ± 48	0.3980	58 ± 4	271	294
BMN doped BST	381 ± 92	0.3993	39 ± 2		

The residual stress in a thin film is originated from various sources mainly the lattice parameter and CTE mismatch between the film and substrate [51, 152], incorporation of impurities (dopants), grain growth, etc. [45, 90, 153-155]. The total stress (σ_{tot}) built in the BST films can be expressed as a superposition of three main components [150, 156]

$$\sigma_{\mathrm{tot}} = \sigma_{\mathrm{Latt}} + \sigma_{\mathrm{th}} + \sigma_{\mathrm{int}}, \tag{6.3}$$

where, σ_{Latt}, σ_{th}, and σ_{int} are stresses due to lattice misfit, CTE mismatch and intrinsic stress, respectively. The intrinsic stress component is mainly caused by the grain growth as a result of necking or cohesion between different particles during film crystallization [157].

Table 6.2. CTE of BST, platinum and alumina

Materials	CTE of the materials, $\times 10^{-6}$ (K^{-1} or $^oC^{-1}$)
BST	10.5
Pt	$7.53 + 4.72 \times 10^{-3}(T - 291) + 2.36 \times 10^{-9}(T - 291)^2$, (T in K)
Al_2O_3	$7.42 + 6.43 \times 10^{-4}T - 3.21\, exp(-2.59 \times 10^{-3}T)$, (T in ^oC)

The lattice mismatch between platinum (3.926 Å) [158] and our BST target (3.953 Å) is negligible; suggesting that the main sources of the stress built in both films are from CTE mismatch and crystallite grain growth. The thermal stress (stress component due to the CTE mismatch between the film and the substrate) can be estimated for a two layer system such as film-substrate layer as [90,155]

$$\sigma_{th} = \frac{E}{1-\upsilon}\int_{T_R}^{T_D}(\alpha_f - \alpha_s)dT, \tag{6.4}$$

where, E, α_f, α_s, ν, T_R, T_D represent the film Young's modulus, film and substrate CTEs, film Poisson's ratio, deposition and room temperature, respectively. The CTEs of BST [111], Pt [158], and Al_2O_3 [159] are presented in Table 6.2. Using Eq. (6.4) along with the CTE expressions in Table 6.2 the thermal stress between BST/Pt and BST/Al_2O_3 film/substrate interfaces was calculated and presented in Table 6.1. Since the substrate used for depositing both BMN doped and undoped BST thin film are identical, the CTE mismatch (presuming the dopants don't change the CTE of BST significantly) between the BST and the substrate does not cause a difference in stress between the films.

The other source of residual stress in the BST thin film results from the grain growth of the film [157, 160]. Grain growth during crystallization occurs as the crystallite swells into the

neighboring grain boundary region typically inducing a large compressive stress for larger grains. The stress generated by the grain growth process is related to the amount of grain boundary area (Δa, negative in sign) that is lost or annihilated during the grain growth, the initial (d_0) and final (d_f) grain sizes through the expression [157, 161]:

$$\sigma_{grain} = \frac{E}{1-\nu}\Delta a\left(\frac{1}{d_i} - \frac{1}{d_f}\right), \tag{6.5}$$

where, σ_{grain}, E, and ν are the residual stress due to grain growth (intrinsic stress), Young's modulus, and Poisson ratio, respectively.

In order to evaluate the residual stress built in the films due to the grain growth, scanning electron microscopy (SEM) studies were performed on both BMN doped and undoped BST films. The SEM images of the two films are shown in Figure 6.4. It is evident from the images that both films are crack free, but the BMN doping in the BST has significantly suppressed the grain growth of the BST film, presumably due to a pinning effect on the grain boundary. A similar grain growth inhibition effect due to the Mg and Nb ions in a BST films was observed elsewhere [34, 70]. The average grain size in both films (d_f) was estimated using the lineal intercept method in accordance with the ASTM E-112-84 standard [162] and is reported in Table 6.1.

The annihilated boundary (excess volume per unit grain boundary area), Δa, is unknown for BST; therefore, for stress evaluation purposes the value of 0.17 nm for Pd metal [163] was used. Since the d_i value for both films is also unknown, determining the absolute residual stress due to the grain growth is impossible. However, considering the initial grain size and excess volume per unit grain boundary area for both films to be the same for both films, the difference in stress due the grain growth between the undoped and BMN doped BST films

$\left(\sigma_{grain}^{doped} - \sigma_{grain}^{undoped}\right)$ can be calculated. Using the d_f values from Table 6.1, the grain growth stress difference between the two films was found to 227 MPa.

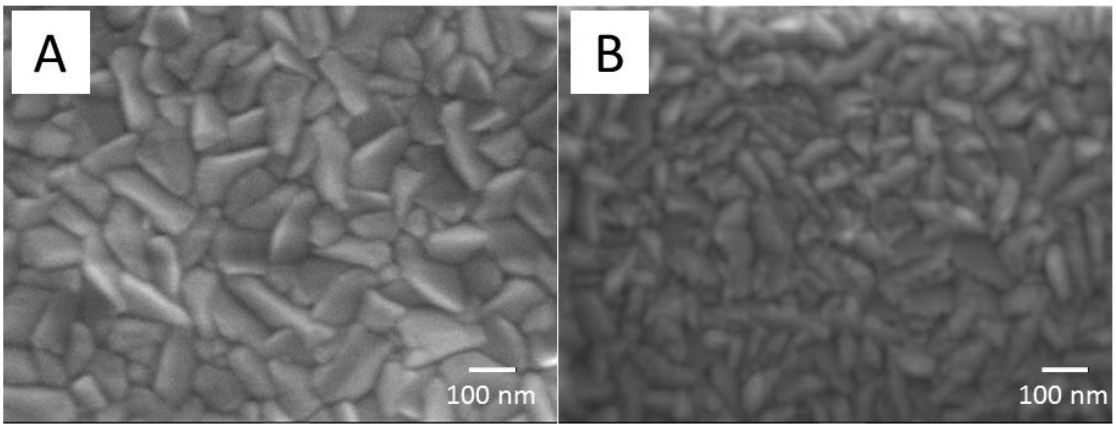

Figure 6.4. FESEM images of the undoped (A) and BMN doped (B) BST thin film on platinized alumina wafers

The obtained positive value $\left(\sigma_{grain}^{doped} - \sigma_{grain}^{undoped} = 227MPa\right)$ suggests that the undoped BST film experiences a higher compressive (negative) stress than the BMN doped film due to larger grains. Since the residual stress is a superposition of stresses of different origins and signs, the lower residual stress value in undoped BST film ($\sigma_{BMN} - \sigma_{BST}$ = 243 MPa, difference of total stress, see Table 6.1) is in accord with more efficient compensation of the tensile stress by higher grain size related compressive stress. Thus, despite the sizable effect of doping on the residual stress absolute value, the very small line slopes in the lattice parameters vs. $\sin^2\psi$ plot for both undoped and doped BST films imply that its influence on the BST film crystal structure is insignificant.

6.1.3. Effect of Oxygen Vacancies

The other factor responsible for XRD peak position shift compared to its target is the presence of oxygen vacancies. Given the high deposition temperature for BST thin films as well

as the re-sputtering of the films from the substrate by the energetic negative oxygen ions in the sputtering chamber (see discussions in Chapter 5), the occurrence of oxygen vacancies in our films is highly likely. The presence of an oxygen vacancy increases the lattice constant (unit cell volume) by increasing the Columbic repulsion between the metal ions (Ba^{2+}, Sr^{2+}, and Ti^{4+}). A similar XRD peak shift observed on BST films deposited by the PLD method [83, 124] was attributed to the presence of oxygen vacancies.

6.2. Surface Morphology of the Films

Understanding the surface morphology and roughness of the films has particular significance since the dielectric properties as well as device performance are affected not only by the well-defined microstructure but also by the quality of the electrode-film interfaces [34, 164]. The surface morphology and roughness of the BST films were evaluated via tapping mode atomic force microscopy (AFM) over a 1x1 μm^2 scan area for each sample. The 3D AFM images of both the undoped and BMN doped BST thin films presented in Figure 6.5 show that both films exhibited a well crystallized microstructure with no cracks, defects, and visible pinholes on the surface.

However, the AFM experiment demonstrated that the doping appreciably suppresses the film surface roughness reducing it from 7.19 nm for undoped BST down to 4.53 nm, which is consistent with the smaller grain size in the BMN doped BST film (see also Figure 6.4). When the film surface is rough, the film-electrode interface quality is poor and contributes to the conductor loss of the device, which in turn manifests itself into higher device insertion loss [34]. Thus, in order to maintain a low device loss a smooth film surface is required, suggesting that the BMN doped film with smoother surface has lower dielectric loss compared to the undoped BST film. Moreover, studies have shown that the film surface roughness has a detrimental effect on

the value of leakage current or film resistivity [164, 165]; therefore, the fact that the BMN doped film is smother than the undoped BST film is consistent with lower leakage current obtained for the BMN doped film in this work (see section 6.6).

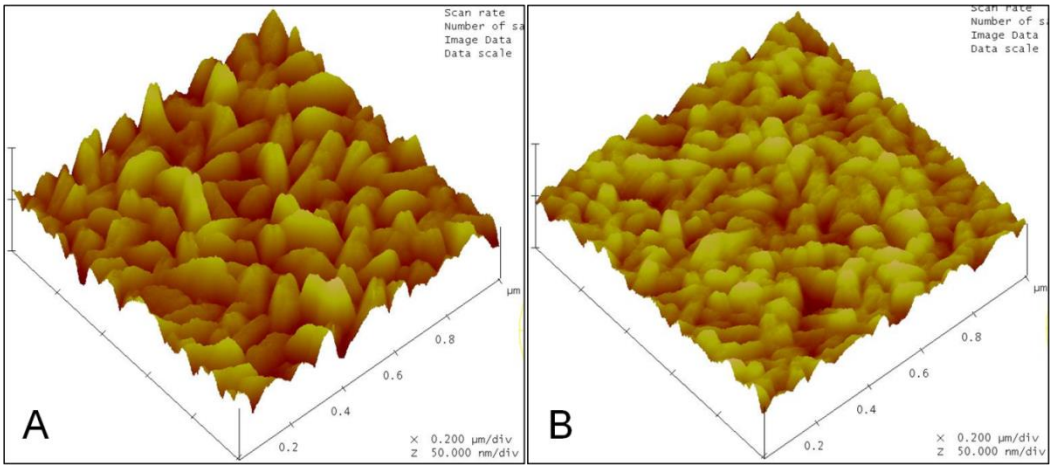

Figure 6.5. AFM images of the undoped BST (A) and BMN doped BST (B) films on platinized alumina wafers

6.3. Raman Spectroscopy of the Films

The lattice dynamical properties of the two BST films were analyzed by Raman spectroscopy at room temperature in a backscattering mode. The Raman spectroscopy is complementary to the XRD method since it provides information on composition (impurity), phase fraction, residual stress, and crystal symmetry of the films. In order to get the complete picture of the Raman spectra of the BST thin films, it is important to start with the Raman spectra of bulk BTO and STO. Figure 6.6 shows the Raman spectra of the BTO and STO powder samples and undoped BST target material.

Any ABO_3 type perovskite crystal has five atoms (one formula unit) per unit cell, leading to 3N (=15, N being number of atoms) degrees of freedom; out of which 12 are optical modes while the remaining 3 are acoustic branches. Above the ferroelectric phase transition

temperature, the BTO, STO, and BST have cubic paraelectric structure with O_h-symmetry in which the optical phonons are compactly written as $\Gamma_{cube} = 3F_{1u} + F_{2u}$ irreducible representation. Each F_u mode is triply degenerate, and in cubic phase, neither F_{1u} nor F_{2u} modes are Raman active (no first order Raman lines) because of odd symmetry with respect to inversion[166].

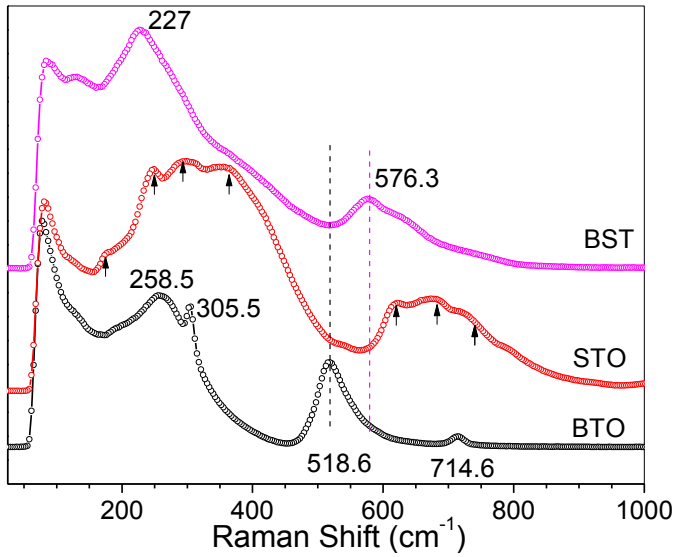

Figure 6.6. Raman spectra of the BTO and STO powders and undoped BST target

Upon transition to tetragonal phase (C_{4v} symmetry), each F_{1u} mode splits into E and A_1 modes, and the F_{2u} mode gives rise to B_1 and E modes. Since the E modes are doubly degenerate, the resulting phonons are presented as $\Gamma_{tetr} = 3A_1 + 4E + B_1$ irreducible modes. All A_1 and E modes are both Raman and IR active, while B_1 mode is only Raman active [166]. Furthermore, due to the long range electrostatic interaction associated with lattice iconicity each A_1 and E modes split further into the transverse optical (TO) and longitudinal optical (LO), i.e. $A_1 \rightarrow A_1(TO) + A_1(LO)$ and $E \rightarrow E(TO) + E(LO)$ [167].

In this experiment, the measurement was performed at room temperature; therefore, BTO is well within the temperature range that it exhibits a tetragonal ferroelectric phase [35], suggesting that all the existing phonon modes are Raman active. For the BTO powder, the Raman peaks observed at 258.5 cm^{-1}, 305.5 cm^{-1}, 518.6 cm^{-1}, and 714.6 cm^{-1} are identified as A_1(2TO), E(3TO+2LO)+B_1, A_1(3TO)+E(4TO), and E(4LO)+A1(3LO), respectively [167, 168]. The peaks that are observed at 305.5 cm^{-1} and 714.6 cm^{-1} are indicative of the tetragonal structure of the BTO which would disappear when the material is in its paraelectric phase. Contrary to BTO, STO is an incipient ferroelectric material which remains paraelectric down to low temperatures. Therefore, all the Brillouin zone center optical phonons are Raman inactive, and there is no first order Raman spectrum that could be measured for the STO crystal. The observed Raman spectrum for the STO (Figure 6.6) is dominated by second order Raman lines which involve the creation and distraction two phonons anywhere in the Brillouin zone provided that momentum is conserved [166].

The Raman spectrum of the solid solution of BTO and STO, $Ba_xSr_{1-x}TiO_3$ (x=1, BTO, and x=0, STO) has been shown to be composition dependent [169] as is the case for the lattice parameter. For the bulk undoped BST target (Figure 6.6), two major Raman peaks are observed at 227 cm^{-1}, and 576.3 cm^{-1}. The absence of the Raman peaks around 305 cm^{-1} and 715 cm^{-1} signifies that target BST material is a cubic BST structure at room temperature as was confirmed by the XRD. The E(4LO)+A1(3LO) mode that appeared at 518.5 cm^{-1} for BTO has shifted to 576.3 cm^{-1}, while the A_1(2TO) mode appeared at 258.5 cm^{-1} for BTO is shifted to 227 cm^{-1} due to the formation of solid state reaction between the BTO and STO.

The Raman spectra of the doped and undoped BST films along with the undoped BST target are shown in Figure 6.7. The Raman peak frequency and the corresponding band

assignment for the films and bulk material is presented in Table 6.3. The two major peaks that were observed around 227 cm^{-1} and 576 cm^{-1} for the BST target are also present in the films, but the former is changed to an observable shoulder while the latter is shifted towards a small wavenumber for the films. As opposed to the bulk material, there are two Raman peaks around 750 cm^{-1} and 870 cm^{-1} for both thin films.

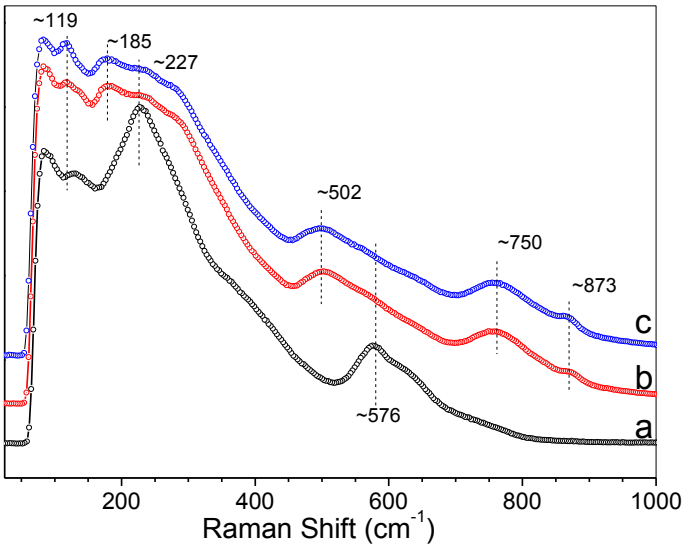

Figure 6.7. Raman spectra of (a) BST target, (b) undoped BST (c) BMN doped BST thin film

Compared to BTO, the Raman peak at 750 cm^{-1} is blue shifted, and indicates the presence of a fraction of tetragonal phase BST material in both thin films as opposed to the XRD results in the films. The down shift in peak position and indication of tetragonal phase BST in films are indicative of the presence of residual stress in both films [170, 171]. The weak peak at 870 cm^{-1} has originated probably as a result of the residual stress at the interface [171]. There is also a low frequency peak (~119 cm^{-1}) that appears to be shifted to a small wavenumber from the bulk BST material. This is may be caused due to a disorder activated scattering from the transverse acoustic (TA) and longitudinal acoustic (LA) phone branches [167, 171].

Table 6.3. Observed phonon modes (cm^{-1}) in the BST thin films and undoped BST target

	Disorder activated	E(TO+ LO)	A_1(2TO)	A_1(3TO)+ E(4TO)	E(4LO)+ A1(3LO)	Interface stress
Undoped BST target	132	….	227	576.3	…	…
Undoped BST film	118.5	185.2	226.2	502.3	749.1	872.9
BMN doped BST film	118.5	185.2	229.4	496.2	755.1	872.9

6.4. Dielectric Properties Characterizations

Following the analytical characterizations (sections 6.1 to 6.3); the metal-insulator-metal capacitor structures were lithographically fabricated on both films (see details in appendix A). Then, dielectric measurements were performed on 2432 uniformly distributed devices consisting of two 0.5×0.5 mm^2 top electrodes separated by a 0.2 mm gap (equivalent to two capacitors connected in series, section 3.2.4). In this section, the results on the relative permittivity, tunability, and dielectric loss (quality factor) of the two films are presented.

The relative permittivity, ε_r, loss tangent, tan δ, and relative tunability, $n_{r,}$ defined by Eq. (2.25) for the representative undoped and BMN doped BST based capacitors as a function of applied bias field, *E*, are shown in Figure 6.8. The bell-shaped dependence of permittivity on bias field verifies that both films are in a paraelectric phase, suggesting that they don't exhibit a hysteresis behavior which is undesirable for agile microwave devices [30]. For these representative devices, at zero bias field, the maximum dielectric constant for the undoped and BMN doped films are about 425 and 320, respectively. The decrease in dielectric constant of the doped film has been attributed to the reduced grain growth observed in the doped BST film due to the grain pinning effects of both Mg and Nb ions [144].

The increase of tunability with the applied electric field for both films is shown in Figure 6.8 (bottom). The tunability of the BMN doped film is slightly lower than that of the undoped film in the entire field region. At the maximum applied bias field (640 kV/cm), 61 % and 55 % tunability values were measured for the undoped and doped BST films, respectively. Moreover, the BMN doping has resulted in a remarkable decrease in the dielectric loss of the BST film. Compared with the undoped film, the loss tangent of the BMN doped film is reduced by ~38 % (loss tangent reduced from 0.048 to 0.03).

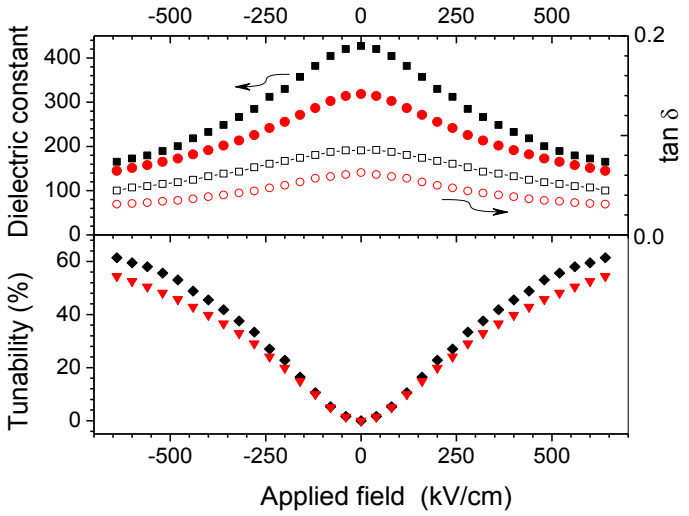

Figure 6.8. The relative permittivity, ε_r, tan δ, and tunability for the representative undoped (black) and BMN doped (red) BST film as a function of bias field, E. The measurement is performed at a constant, 30 MHz, frequency

From the device point of view for microwave application, the trade-off between tunability and dielectric loss is crucial. A figure of merit (FOM),which relates the tunability and dielectric loss of the film as in Eq. (2.27), is a simple and handy parameter to reflect the trade-off between these two quantities [12]. Figure 6.9 presents the FOM of the doped and undoped BST films as a function of applied field. Due to the slight decrease in tunability, but substantial drop in the dielectric loss, which is resulted from the BMN dopant in BST, the FOM for the

BMN doped BST film is notably higher than that of the undoped BST film. This suggests that the accepter (Mg^{2+}) and donor (Nb^{5+}) co-doping through the complex BMN oxide leads to a good quality BST film which can be better applied to manufacture tunable microwave devices as compared to the undoped film.

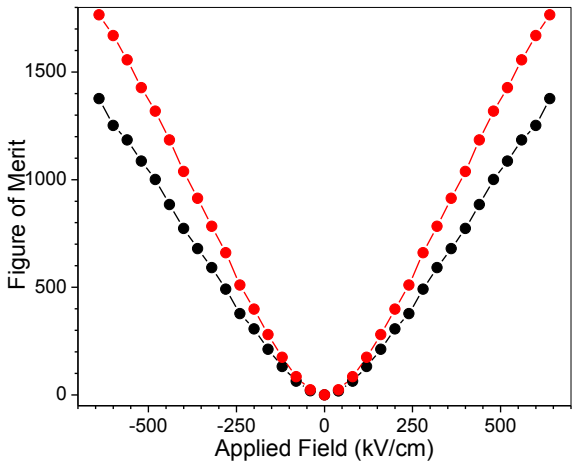

Figure 6.9. FOM for undoped (black) and BMN doped (red) BST films vs. bias field, E

The tunability (at 640 kV/cm) distribution histograms for all capacitor devices fabricated on undoped and BMN doped BST films (> 2000 devices for each film) are shown in Figure 6.10. A relatively wide spread result was measured for the undoped BST film compared to the BMN doped BST film. The primary, secondary, and tertiary frequency peaks represent more than 80 % of devices with tunability value within the intervals of 50-65 % and 45-60 % for undoped and BMN doped BST films, respectively. Presuming the normal distribution the corresponding average tunability values are 56.8 % and 52.5 %, while about 0.5 % of devices demonstrated tunability exceeding 70 %.

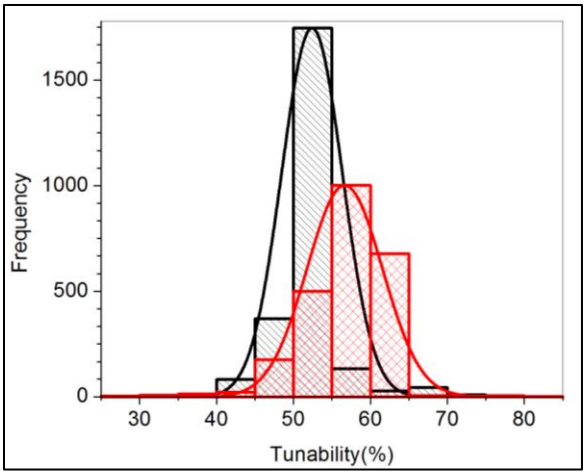

Figure 6.10. The tunability distribution histograms for undoped (red) and BMN doped (black) BST devices

Comparing the tunability for the two films, the value obtained for the doped film is lower by ~ 8.0 %. As mentioned above, Mg^{2+} doping of BST films allows significant suppression of dielectric losses and enhancement of insulation properties but at the expense of a substantial drop both in permittivity and tunability (up to 40 % at 5 mol % doping level [68]). While the presence of Mg ions (in BMN) in this film also caused a drop in tunability, its effect is less severe; suggesting that the negative effect of Mg is partially compensated by Nb ions. It is known that the nonlinear behavior of BST's dielectric constant—making it essential for microwave applications—with the applied electric field is due to the displacement of Ti ion within an oxygen octahedron (O_h) [35]. Because of the fixed space within the oxygen octahedron, the sizes of the ions that substitute Ti^{4+} have direct impact on altering the dielectric properties of BST. In this particular case, replacing Ti^{4+} ((r (Ti^{4+}) = 0.75 Å) with Mg^{2+} (r(Mg^{2+}) = 0.86 Å > r (Ti^{4+})) and Nb^{5+}((r (Nb^{5+}) = 0.69 Å < r (Ti^{4+})) results in two opposing effects. The large Mg^{2+} occupies a wider space which ultimately limits its rattling at the center of the oxygen octahedral. On the other hand, the small Nb^{5+} resides in a lesser space and promotes ionic displacement [137, 172]. The contending effect of the two ions in the oxygen octahedron minimized the drop in tunability

that would be caused by Mg. Conversely, the decrease in dielectric loss is related to the coupling of Mg charged defect with oxygen vacancy. When an oxygen vacancy couples with a Mg defect forming defect dipole (vide infra), hopping of electrons generated from the oxygen vacancy between different Ti ions [64, 173] is inhibited and thus lowers the dielectric loss.

An average dielectric constant (measured at zero bias) of 398 and 336 was measured from the undoped and doped BST films, respectively. The 16 % reduction of the dielectric constant of BMN doped BST films is attributed to the decrease of the grain size as a result of Mg and Nb ions [34, 70]. It is known that thin ferroelectric films electromechanical response is much more sensitive to the grain and crystallite size than that in the corresponding bulk ceramics [174]. In ferroelectric materials this effect is usually associated with the grain mosaic structure in the films, which reduces the crystalline coherence [175] causing the permittivity drop and T_c low temperature shift. The grain size dependence of paraelectric BST films is usually related to a super-paraelectric behavior [174]; and can be explained within the Binder model [176] presuming the presence of interior and surface components in the grain with the latter having reduced permittivity while still being ferroelectrically active [177]. Due to a higher contribution of the surface component, the permittivity of films with smaller grains is also lower.

6.5. Interface Capacitance and Dead Layer Thickness

One of the major factors that degrade the dielectric properties of the thin films compared to the bulk material is the interfacial capacitance or the dead layer. In this section, the interfacial capacitance and the dead layer thickness of the doped and undoped BST films were determined to understand the effect of the BMN dopant on the interface, if at all.

The interface capacitance is commonly estimated by measuring the capacitance of multiple films with variable thickness, and plotting the inverse of the measured capacitance

against the thickness to obtain a non-zero intercept [47, 178], interfacial capacitance. The active and the "dead" portion of the BST film are commonly described by a series capacitor model as shown in Figure 6.11. The regions I and III are the dead layers corresponding to the top and bottom electrode interfaces, respectively, each with a width of X_d and constant permittivity of ε_d. The interior region II, of width of t-$2X_d$, t being the total thickness of the film, represents the region of the BST film whose dielectric permittivity changes with electric field ($\varepsilon_b(E)$), and behaves similar to the bulk BST material. From this model, the total measured (C_{meas}) capacitance of the film can be related to the capacitances from the bulk like region (II) and the interfaces (I&III) as

$$\frac{A}{C_{meas}(E)} = \frac{2X_d}{\varepsilon_d} + \frac{t-2X_d}{\varepsilon_b(E)}, \tag{6.6}$$

where, A is the area of the capacitors.

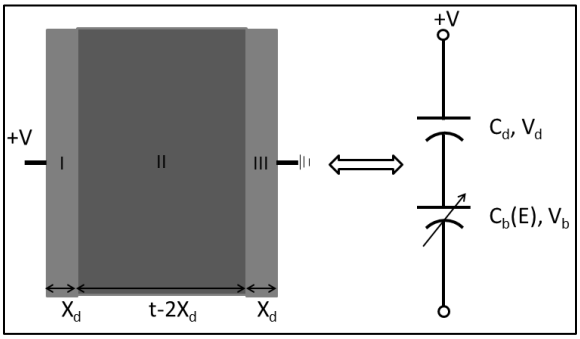

Figure 6.11. Schematic showing the two dead interfaces of the BST film of width X_d, and interior region, of width t-$2X_d$. The equivalent circuit is presented on the right

To use Eq. (6.6) in determining the interfacial capacitance density, one needs to deposit multiple films with varying thickness and plot a graph of the term on the left hand side versus the thickness of the film [47]. This approach is evidently expensive as it requires the deposition of many samples and its reproducibility may also be tough. The other alternative approach that can

be used in estimating the interfacial capacitance, dead layer thickness and permittivity, is the phenomenological Landau-Ginzberg-Devonshire (LGD) theory [31, 179, 180].

As presented in section 2.2.3, in LGD theory, the Helmholtz free energy for the ferroelectric materials is expressed in terms of polarization, *P*, (see Eq. (2.20)); from which the equation of state $\left(i.e.\ {}^{\partial \mathrm{F}}/_{\partial P} = E\right)$ leads to the relation between the polarization and electric field written as

$$\mathrm{E} = \beta P + \gamma P^3. \tag{6.7}$$

From this equation the field dependent dielectric permittivity ($\varepsilon_b(E)$) of the interior region (II) can be defined as [31]

$$\varepsilon_b(E) = \frac{\partial P}{\partial E} = \frac{1}{\beta + 3\gamma P^2}. \tag{6.8}$$

Furthermore, using a simple hyperbolic identity

$$(\sinh\varphi)^3 + \frac{3}{4}\sinh\varphi - \frac{1}{4}\sinh 3\varphi = 0, \tag{6.9}$$

Eq. (6.7) can be explicitly solved to express the polarization in terms of the electric field. To find this, let's define the polarization, *P*, with a sine hyperbolic function as

$$P = B\sinh\varphi. \tag{6.10}$$

Substituting Eq. (6.10) into Eq. (6.7) gives

$$(\sinh\varphi)^3 + \frac{\beta}{\gamma B^2}\sinh\varphi - \frac{E}{\gamma B^3} = 0. \tag{6.11}$$

By comparing Eqs. (6.9) and (6.11) one can obtain

$$B = \sqrt{{}^{4\beta}/_{3\gamma}} \tag{6.12a}$$

and

$$\varphi = \frac{1}{3}\sinh^{-1}\left(\sqrt{\left(27\gamma/4\beta^3\right)}\ E\right), \tag{6.12b}$$

which along with Eq. (6.10), results in an explicit expression for the polarization as a function of electric field

$$P(E) = \sqrt{\left(\frac{4\beta}{3\gamma}\right)}\ \sinh\left(\frac{1}{3}\sinh^{-1}\left(\sqrt{\frac{27\gamma}{4\beta^3}}\ E\right)\right). \tag{6.13}$$

Finally, the expression for the measured capacitance density can be presented as

$$\frac{A}{C_{meas}(E)} = \frac{2X_d}{\varepsilon_d} + \beta(t - 2X_d)\left\{1 + 4\left(\sinh\left(\frac{1}{3}\sinh^{-1}\left(\sqrt{\frac{27\gamma}{4\beta^3}}\ E\right)\right)\right)^2\right\}, \tag{6.14}$$

by substituting Eq. (6.13) into (6.8), and the resulting expression into Eq. (6.6). This equation can be fitted to the experimentally measured inverse capacitance density versus applied electric field to extract the X_d, ε_d, β and γ parameters.

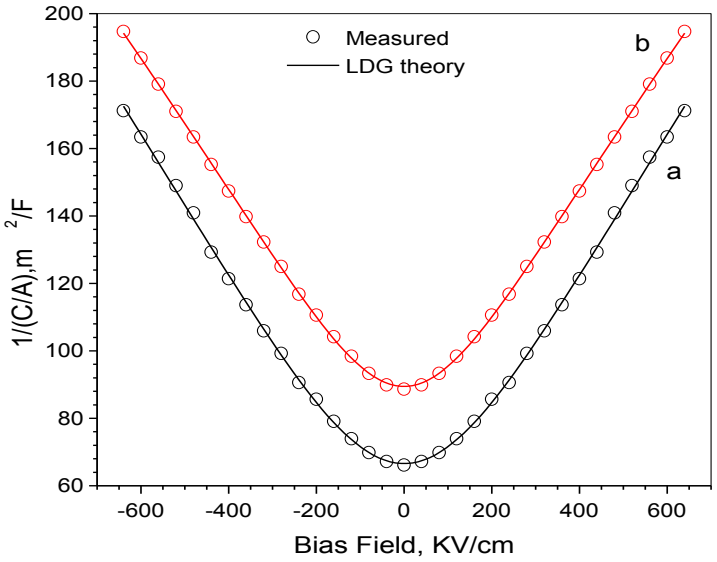

Figure 6.12. Inverse capacitance density vs. electric field: a) pure and b) BMN doped BST film

Figure 6.12 shows the fitting of the measured data for the undoped and BMN doped BST thin films to Eq. (6.14). The LDG line has fitted reasonably well to the measured data and the

extracted parameters are presented in Table 6.4. The coefficients, β and γ, obtained from the fitting are comparable with values reported in the literature [179]. Wider dead layer thickness accompanied by lower non-tunable permittivity for the BMN doped film leads to lower capacitance density at the interface, which might be due the weakening of ferroelectricity as a result of magnesium ions [68].

Table 6.4. Extracted fitting parameters for the doped and undoped BST films

Samples	β (m^2/F)	γ (m^5/C^2F)	ε_d	X_d (nm)	Interface capacitance (fF/$um^{2)}$
Undoped BST	$3.2x10^8$	$6.7X10^9$	$86.6\varepsilon_0$	6.8	112.7
BMN doped BST	$2.6x10^8$	$6.1X10^9$	$72.4\varepsilon_0$	9.5	67.3

It is known that the presence of the dead layer at the interface reduces the overall permittivity and tunability of the ferroelectric film [181]. In an ideal condition where there is no dead layer (i.e. X_d=0) at the interfaces, $\varepsilon_{meas} = \varepsilon_b$, and the tunability can be written as

$$n_{ideal} = \frac{\varepsilon_b(0)}{\varepsilon_b(E)}. \quad (6.15a)$$

Here n_{ideal} represents the tunability in the absence of the dead layer. In the presence of the dead layer ($X_d \neq 0$), $\varepsilon_{meas} \neq \varepsilon_b$ and rearranging Eq. (6.6), the measured permittivity can be written as

$$\varepsilon_{meas}(E) = \frac{t\varepsilon_d\varepsilon_b(E)}{2X_d\varepsilon_b(E)+\varepsilon_d(t-2X_d)}. \quad (6.15b)$$

The tunability of the non-ideal film can be expressed as

$$n_{meas} = \frac{\varepsilon_{meas}(0)}{\varepsilon_{meas}(E)} = \zeta(E)n_{ideal}, \quad (6.15c)$$

where,

$$\zeta(E) = \frac{2X_d\varepsilon_b(E)+\varepsilon_d(t-2X_d)}{2X_d\varepsilon_b(0)+\varepsilon_d(t-2X_d)}. \quad (6.15d)$$

Since, $\varepsilon_b(0) > \varepsilon_b$ (E), $\zeta(E) < 1$, indicating the reduction in tunability, $n_{meas} < n_{ideal}$.

For the particular devices used in this analysis, a tunability of 61 % for the undoped and 55 % for the BMN doped film was measured. Using the parameters in Table 6.4, the tunability that would be obtained without dead layer is estimated to be 69 % for the undoped and 64 % for the BMN doped films, showing an improvement by 11% and 16 %, respectively. Similarly, when the dead layer is corrected, the dielectric constant at zero bias field for the undoped BST film increases from 427 to 552 while that of the BMN doped film rises from 319 to 443—showing an increase by 30 % and 40 %, respectively. The reduction in tunability and permittivity shows the deteriorating effects of the dead layer on tunable devices. This influence is observed to be more pronounced on the doped film which could be due to the presence of the Mg dopant.

6.6. Leakage Current and Carrier Transport Mechanisms

The leakage current dependence on the applied voltage and temperature in both doped and undoped BST thin films were measured using an Agilent B1500A Semiconductor Device Analyzer and a hotplate whose temperature was monitored by an external thermocouple. Figure 6.13 shows the leakage current versus voltage plots of the undoped (Figure 6.13a) and BMN doped (Figure 6.13b) BST thin films in a temperature range of 300-450 K. It is observed that the leakage current measured for the BMN doped film is lower than the undoped film, suggesting that the Mg/Nb co-doping that ensures the charge neutrality compensation (i.e. $[Mg''_{Ti}] = 2[Nb^{\bullet}_{Ti}]$) reduces the leakage current of the BST film [70, 144].

The leakage current data (Figure 6.13) has shown strong dependence on temperature and presented two voltage regimes. In the low voltage regime, the leakage current is insignificant and remains nearly constant with voltage. However, beyond a certain minimum bias voltage, the leakage current rises exponentially. The minimum bias voltage above which the BST capacitor leaks appreciably is found to decrease (see the

shifting of the I-V profiles left) with the increase of temperature for both films, suggesting an increase of free carriers' concentration due to the rise of thermal excitation in the material. Interestingly, the BMN doped film required higher voltage, compared with the undoped BST film, to allow the rise of leakage current significantly; confirming the improvement of the insulating properties in the BMN doped BST.

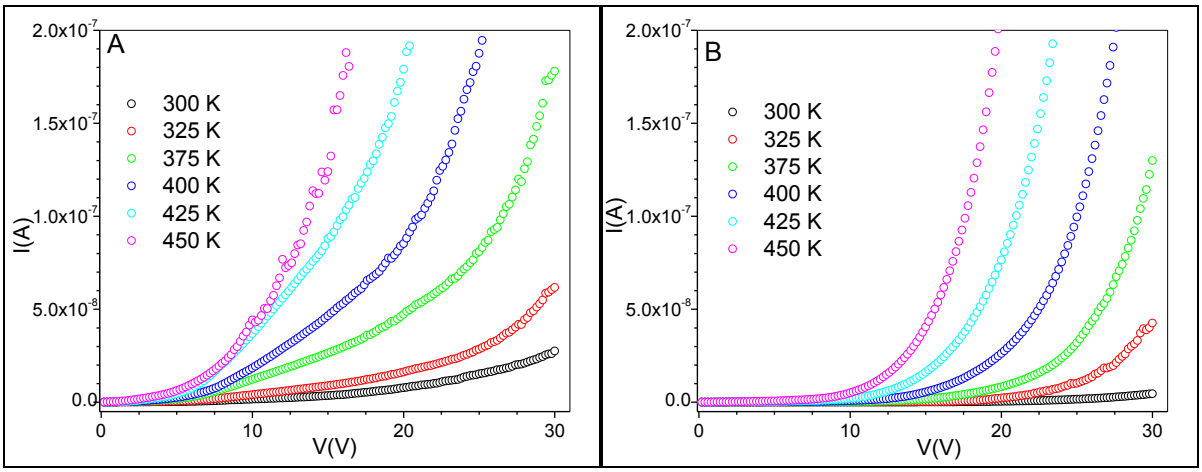

Figure 6.13. I-V relation at variable temperature for undoped (A) and doped BST films (B)

The carrier transport in BST film has been attributed to mechanisms which can be broadly classified as the interface and bulk limited conduction mechanisms. The interface limited conduction mechanisms control the transfer of carriers from electrode to the ferroelectric film through the potential barrier created at the interface. Schottky thermionic emission[182-184] and Fowler-Nordheim tunneling [182, 184] are typical conduction mechanisms that belong to the interface controlled transport mechanisms. In the bulk limited mechanisms, the conduction of carriers is limited by the properties of the film (e.g. the presence of shallow trap levels in the forbidden gap). Space charge limited conduction (SCLC) [184] and Poole-Frenkel emission [184-186] are some of the models that are used to describe the bulk limited conduction mechanisms. Even though no single mechanism can fully describe the nature of carrier transport

in BST, the strong temperature dependence (see Figure 6.13) suggests that either the Schottky thermionic emission (SE) [182, 183] or the Poole-Frenkel emission (PF) [185, 186] dominates the conduction mechanism in BST films.

To identify the transport mechanisms in the BST films, the leakage current data were tested in light of both the SE and PF conduction mechanisms. The relation between current density J and applied electric field E for the SE and PF are given by

$$J = A^{*}T^{2}exp\left(-q\left(\varphi_b - \sqrt{qE/4\pi\varepsilon_o\varepsilon_r}\right)\Big/_{kT}\right), \tag{6.16a}$$

and

$$J = q\mu N_C E exp\left(-q\left(\varphi_t - \sqrt{qE/\pi\varepsilon_o\varepsilon_r}\right)\Big/_{kT}\right), \tag{6.16b}$$

respectively, where A* is the Richardson constant, q is electronic charge, T is the temperature, $q\varphi_b$ is the Schottky barrier height, μ is the electron mobility, N_C is the effective electron density of states in the conduction band, $q\varphi_t$ is the trap ionization energy, ε_o is the permittivity of free space, and ε_r is the dynamic permittivity (high frequency permittivity) of the BST film. In each case, the applied electric field lowers the potential barrier (SE) or trapping potential (PF) for the electrons to escape. The two mechanisms are due to the Columbic interaction between the escaping electron and a positive charge; but, they differ in that the positive charge is fixed for the Poole-Frenkel trapping barrier, while it is a mobile image charge for the Schottky barrier [184].

In order to simplify the current data analysis, Eqs. (6.16a&b) can be linearized with respect to $\sqrt{E}$ as [182]

$$ln\left(\frac{J}{T^2}\right) = F(T) + \left(\frac{1}{kT}\sqrt{\frac{q^3}{4\pi\varepsilon_o\varepsilon_r}}\right)\sqrt{E}, \tag{6.17a}$$

and

$$\ln\left(\frac{J}{E}\right) = G(T) + \left(\frac{1}{kT}\sqrt{\frac{q^3}{\pi\varepsilon_o\varepsilon_r}}\right)\sqrt{E}, \qquad (6.17b)$$

If the current conduction is dominated by the SE, the graph of $\ln(J/T^2)$ versus $\sqrt{E}$ should be a straight line where the slope results in a dynamic dielectric constant, while the intercept, $F(T) = \ln(A^*) - \frac{q\varphi_b}{kT}$, can be used to estimate the potential barrier height. Likewise, if the conduction is controlled by the PF model, the $\ln(J/E)$ versus $\sqrt{E}$ will be linear and the slope is used to extract the dynamic dielectric constant, while the intercept, $G(T) = \ln(q\mu N_C) - \frac{q\varphi_t}{kT}$, is used to approximate the trap ionization potential.

Figure 6.14 shows the plot of $\ln(J/T^2)$ versus $\sqrt{E}$ for undoped BST film. The current data, particularly at higher field region, satisfy the SE well; however, for the SE to dominate the conduction mechanism in the film, the physical parameters (dynamic dielectric constant and potential barrier) that are extracted from the slopes and intercepts of the linear fit must deliver a physical meaning. The dynamic dielectric permittivity calculated from the slopes of the linear fit at all the temperature range for both films is presented in Table 6.5.

Table 6.5. Dynamic dielectric permittivity extracted from SE and PF fitting

	SE: $\ln(J/T^2)$ vs. $\sqrt{E}$		PF: $\ln(J/E)$ vs. $\sqrt{E}$	
Temperature (K)	ε_r- undoped BST(Fig. 6.14)	ε_r-BMN doped BST (data not shown)	ε_r-undoped BST (data not shown)	ε_r-BMN doped BST (Fig. 6.15)
300	5.76	1.51	54.40	8.85
325	4.84	0.73	21.55	4.65
375	4.75	0.78	16.87	4.59
400	3.67	0.65	9.54	3.89
425	2.20	0.60	6.54	3.46
450	1.49	0.47	8.67	3.82

The refractive index of BST, determined by optical method at a wavelength of 640 nm, is roughly 2.0 so that the dielectric permittivity value, $\varepsilon_r = n^2$, is about 4 [187]. The values of ε_r extracted from the SE plots for the undoped BST film are in the range of 5.76 to 1.49, decreasing with the increase of temperature from 300 to 450 K. These ε_r values agree well with the reported results ranging between 3.5 and 6.0 [183, 186-189]. The well fitted curve along with the sensible ε_r values confirms that the SE model is the dominant conduction mechanism in the undoped BST film. On the other hand, the ε_r values extracted from SE plots (data not shown) for the BMN doped BST thin film were found to be unrealistically small (ranging 1.50 to 0.47, see Table 6.5), suggesting that SE model cannot control the conduction mechanism in the doped BST film.

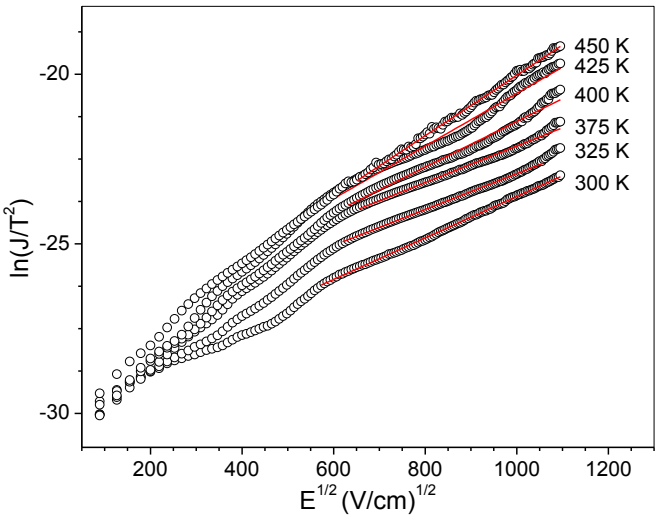

Figure 6.14. $\ln(J/T^2)$ vs. $\sqrt{E}$ for the undoped BST film

The current data of the BMN doped BST thin film was further tested against the PF conduction mechanism. Figure 6.15 shows the graph of $\ln(J/E)$ versus $\sqrt{E}$ for the BMN doped BST film. The high field region data fit well with PF model at all temperature ranges, leading to dynamic dielectric permittivity ranging from 8.85 to 3.85 (see Table 6.5) that fall well within the normal range[183, 186-189]. The result suggests that, unlike the SE model, the PF

model is the dominant conduction mechanism in the doped BST thin film. A similar analysis on the undoped BST film (data not shown) indicates that the conduction mechanism in the film cannot be dominated by the PF conduction mechanism since the extracted ε_r parameters are unrealistically large (54.4 to 9.0, see Table 6.5).

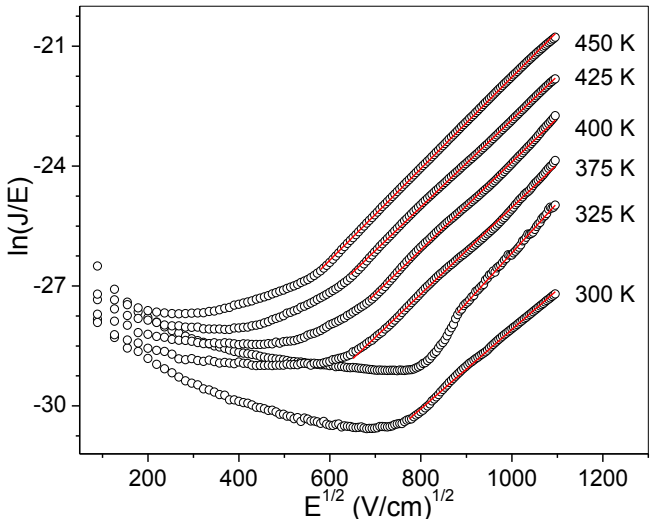

Figure 6.15. $\ln(J/E)$ vs. $\sqrt{E}$ for the BMN doped BST film

The potential barrier height, $q\varphi_b$ for the undoped BST film, and trap ionization potential, $q\varphi_t$ for the BMN doped BST, were estimated from the intercepts (*F(T)* and *G(T)*) of the linear fits of the SE and PF models, respectively. Figure 6.16 shows the graph of *F(T)* and *G(T)* versus 10^3/T. By linear fitting the data for F(T) and G(T), the potential barrier height of 0.42 eV and trap ionization potential of 0.57 eV were extracted from their slopes for the undoped and BMN doped BST film, respectively. The numbers are found to be comparable with reported barrier height for the SE model [183, 190], and trap ionization energy for PF model [186, 190] for BST thin films.

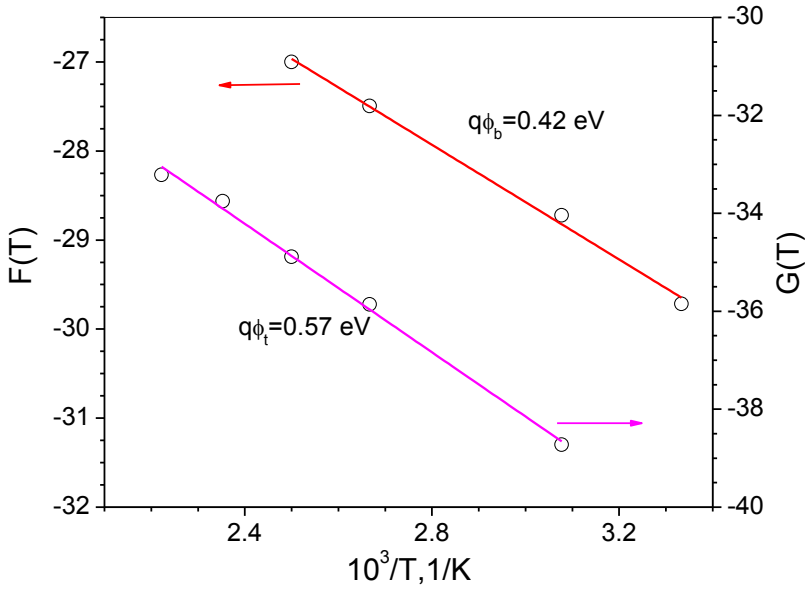

Figure 6.16. F(T) and G (T) vs. 10^3/T

The co-doping of BST with Mg^{2+}/Nb^{5+} has resulted in a significant improvement of the leakage current. In order to interpret this, the behavior of the BMN dopant in BST was proposed to follow the defect reaction (using Kroger-Vink notation) shown in Eq. (6.18a)

$$3BaMg_{1/3}Nb_{2/3}O_3 + BaO \xrightarrow{3TiO_2} 4Ba_{Ba}^{\times} + Mg_{Ti}'' + 2Nb_{Ti}^{\bullet} + 10O_O^{\times}. \qquad (6.18a)$$

This reaction scheme shows that when Mg^{2+} and Nb^{5+} substitute Ti^{4+}, they form Mg_{Ti}'' and $Nb_{Ti}^{\bullet}$ charged defects due to the differences between the charges of the dopants and the titanium ion. In addition to these extrinsic charged defects, the absence of oxygen from its crystallographic site forms an intrinsic charged defect, oxygen vacancy ($V_O^{\bullet\bullet}$), as indicated in Eq. (6.18b).

$$O_O^{\times} \rightarrow V_O^{\bullet\bullet} + \frac{1}{2}O_2 + 2e'. \qquad (6.18b)$$

It is known that when oppositely charged defects are incorporated in a ferroelectric crystal, they form defect dipoles in order to minimize the total electrostatic energy of the crystal [70, 173, 191]. In this case, owing to the presence of two donor type defects ($Nb_{Ti}^{\bullet}$ and $V_O^{\bullet\bullet}$) and

one accepter type defect ($Mg_{Ti}^{''}$), two types of defect dipoles may be formed as $(Mg_{Ti}^{''} \rightarrow 2Nb_{Ti}^{\bullet})$ [70] and $(Mg_{Ti}^{''} \rightarrow V_O^{\bullet\bullet})$ [173] that act as insulating layer or enhance the potential barrier of BST and thus responsible for the decrease of dielectric loss and leakage current of BST.

In this work, the relation between concentration of Mg and Nb is fixed to satisfy the neutrality condition. This means that every $Mg_{Ti}^{''}$ is coupled with $Nb_{Ti}^{\bullet}$; but, due to the small distance between $Mg_{Ti}^{''}$ and $V_O^{\bullet\bullet}$ in the BST perovskite, the coupling between $Mg_{Ti}^{''}$ and $V_O^{\bullet\bullet}$ is highly favorable than the one between $Mg_{Ti}^{''}$ and $Nb_{Ti}^{\bullet}$, suggesting that there are uncoupled $Nb_{Ti}^{\bullet}$ defects that sit at the shallow donor level in the forbidden gap of the BST. These $Nb_{Ti}^{\bullet}$ defects act as a fixed positive trapping center [20] for electrons; thus, localizing free carriers injected from the contacts and substantially extending the device control voltage. Besides, the carrier transport in the BMN doped film is dominated by the PF mechanisms due to the niobium traps.

6.7. Conclusions

Composition, microstructure, dielectric and electrical properties of undoped and BMN doped BST thin films deposited on platinized alumina substrates have been investigated. The undoped film demonstrated a composition close to $Ba_{0.4}Sr_{0.6}TiO_{3-\delta}$, ($\delta$~0.08) suggesting the presence of oxygen vacancies, which is consistent with a slightly larger than expected lattice parameter. The analysis of microstructure has shown that despite the sizable effect of doping on the residual stress, the latter is partially compensated by the CTE mismatch, and its influence on the BST film crystal structure is insignificant. The Raman study on the films has shown significant shifts in peaks, which was attributed to the presence of residual stress in the films.

It was demonstrated that the BMN doped film has an average tunability (>2000 devices) of 52.5% at 640 kV/cm, which is ~8 % lower than the value for the undoped film. This drop is

associated with the presence of Mg ions in BMN whose detrimental effect was partially compensated by Nb ions. The decrease in grain size upon doping may also contribute to the tunability and permittivity drop. On the other hand, BMN doping has reduced the dielectric loss by over 35 %, leading to a higher FOM which shows a good trade-off between the two parameters. Moreover, the interface properties of the films were examined by with the Landau-Ginzberg-Devonshire (LGD) theory. It was found that the effect of the dead layer on the properties of the films is worse because of the magnesium dopant.

The concurrent acceptor and donor doping of BST thin films through BMN allows the achievement of a compensational concentration yielding no free carriers. The presence of Mg^{2+} acceptors prevents the reduction of Ti^{4+} to Ti^{3+} neutralizing the shallow donors associated with oxygen vacancies, substantially reducing the concentration of bulk generated carriers and subsequently the loss and leakage current when compared with the undoped film. Moreover, the defect dipoles formed from $Mg_{Ti}^{''}$, $V_O^{\bullet\bullet}$ and $Nb_{Ti}^{\bullet}$ act as insulating layers to reduce the leakage current.

The carrier transport behavior in the films was analyzed in light of the SE and PF mechanisms. While the conduction in the undoped film was dominated by the SE mechanism, the transport mechanism in the doped film was observed to be dominated by the PF model. The change of the conduction mechanism from SE to PF is attributed to the presence of a large number of $Nb_{Ti}^{\bullet}$ sitting as a positive trap center at the shallow donor level of the forbidden gap of the BST film. These traps also localize free carriers injected from the contacts thus substantially extending the device control voltage (above 10 V).

7. COMBINATORIAL APPROACH IN BST THIN FILMS

As discussed in the preceding chapter, incorporating small amount of dopants into BST has been shown to be an effective method to modify the tunability, dielectric loss and insulating properties of the material. Both aliovalent (e.g. Mg^{2+}, La^{3+}, Ce^{3+}, Nb^{5+}, W^{6+}) [64-68] and isovalent (e.g. Sr^{2+}, Ce^{4+}, Zr^{4+}, Sn^{4+}, Ge^{4+}) [136] dopants have been widely studied for BST thin films. Some of these dopants are effective in suppressing the dielectric loss while deteriorating the permittivity and tunability of the BST material. Others improve the dielectric permittivity and tunability, but worsen the loss properties of the material.

Introducing dopants with opposite effects into BST may be useful to achieve high tunability and low dielectric loss in the material. For example, concurrent Mg/Nb doping in BST has shown an improved loss without significantly reducing the tunability of the film [144] due to the opposite effects of the two dopants on BST. In general, it is believed that the use of multiple dopants (two, three, or even more) in BST is vital to realize an acceptable trade-off between dielectric tunability and loss, since these dopants improve the tunability of the film and target different loss channels (mechanisms) of the material.

In order to obtain the optimum tunability and dielectric loss by multi-doping, it is crucial to select the right type of dopants and determine their precise concentration. For this purpose, the use of conventional one by one (one sample synthesis and characterization at a time) approach is undesirable due to the slow, expensive and rather unpredictable trial-and-error nature of the method. Alternately, the combinatorial materials synthesis methodology is inexpensive; and combined with high throughput characterization (HPC) methods it enables rapid and efficient screening of the best dopants and determination of their concentration [71, 72, 192-194].

Moreover, the combinatorial method can be used to discover new materials as well as optimize the existing ones.

The combinatorial approach can be described as a method used for the synthesis of multiple samples or a "library" of samples that differ in composition. The library is rapidly tested for the property of interest resulting in the generation of large, complete, and reliable data sets which can be analyzed to identify the intended 'sweet spot' [71, 194, 195]. The unique characteristics of this method is that all the experiments are carried out on the same library, with the same measurement tool over a short time period; thus, eliminating most systematic errors.

7.1. Combinatorial Approach in Materials

Traditionally, scientists and engineers have relied on the conventional one-by-one process to discover and develop new materials. However, to compete successfully and claim priority with new products and recipes, one must be able to accelerate the discovery and optimization processes. In this regard, the use of a high throughput combinatorial approach is widely considered as a solution. Perhaps with the biggest impact in the pharmaceutical industries, which along with the advances in robotics allow speeding up the drug discovery processes, combinatorial chemistry is generally recognized as the earliest combinatorial methodology.

The concept of the combinatorial approach was extended to the fields of materials science by J. J. Hanak [196], in 1970, as a way around conventional laboratory procedures. With little acceptance for the next 25 years, mainly due to the lack of suitable tools (e.g. computers and sophisticated high resolution characterization tools) [192], the first successful combinatorial approach in materials science was carried out by Xiang et al.[197, 198]. In this work, arrays of luminescent materials with different composition were obtained by co-depositing a film from

multiple sources by sequentially moving physical masks. Inspired by this, the technique has received tremendous attention [198-200] to the extent that only after 10 years industry is heavily involved in its development.

Analogous to the need for the rapid discovery of new drugs in pharmaceutical industry, the development of new and efficient high performance dielectric materials for the communication technology sector requires a short innovation cycle to keep pace with its short time-to-market characteristics. Thus, applying combinatorial materials synthesis to dielectrics offers advantages: (i) to accelerate the discovery of efficient dielectric material and optimize existing systems, (ii) to investigate the effects of a wide variety of dopants on dielectric properties, and determine the optimal doping level in a timely fashion [193, 201-203].

7.2. Combinatorial Thin Film Libraries

Combinatorial study in dielectric and ferroelectric materials is best performed in the form of thin film libraries [72, 193], which are mainly deposited via PVD methods, including PLD, evaporation and RF magnetron sputtering [197, 204, 205]. The combinatorial thin film libraries can be divided into two main groups: discrete and continuous composition methods. In the discrete combinatorial synthesis (DCS), the combinatorial libraries are generated by sequentially depositing individual (selective) precursors of interest through a series of multiple physical masks. The use of multiple masks during deposition ensures the creation of a spatially defined library of the film [197]. This deposition is usually performed at room temperature and requires a post-deposition annealing to facilitate the reaction between the constituent amorphous precursors and the formation of desired phases [197, 203, 204].

The continuous composition or continuous composition spread (CCS) thin film deposition method is based on the co-deposition of material from multiple (two or more) sources

that are spatially separated and chemically distinct to produce a thin film with an inherent composition gradient on the substrate. The initial work on the CCS approach can be traced as far back as 1965 when Kennedy et al. concurrently evaporated three metals (Fe-Cr-Ni) sources to obtain a composition spread film on a substrate for rapid determination of ternary alloy phase diagrams [206]. Since then the methodology has been used both for systematic exploration of known materials as well as intentional discovery of new materials with targeted properties [205, 207]. No masks or post-deposition annealing are necessary in the CCS method; consequently, the use of deposition conditions optimized for an individual source is sufficient to obtain a film with desirable composition and phase on the substrate.

Combinatorial libraries of BST have been prepared both by DCS and CCS methods. In the DCS approach, layers of amorphous TiO_2, BaF_2 and SrF_2 were sequentially deposited using precisely positioned physical masks to fabricate $Ba_xSr_{1-x}TiO_3$ thin film libraries [208]. The A-site composition (i.e. value of *x*) is controlled through the thickness of the layers at each site on the library. Systematic investigation of the effect of multiple dopants on the dielectric constant and losses of the BST film was also conducted by sandwiching the dopants between the TiO_2 (deposited first) and BaF_2/SrF_2 layers [203, 204]. As the deposition of the layers was conducted at room temperature, a series of controlled thermal treatments were carried out to promote inter-diffusion of layers and dopants, remove F_2, and crystalize the BST film.

Similarly, the CCS method was applied to fabricate an epitaxial $Ba_{1-x}Sr_xTiO_3$ thin film library using PLD from the $BaTiO_3$ and $SrTiO_3$ targets and the layer-by-layer gradient "wedge" approach [209]. The compositional gradient across the substrate was created by performing a series of shadow depositions through a rectangular opening in an automated shutter, which moves back and forth over the substrate during the deposition. The motion of the shutter creates

a thickness gradient with a ‘‘wedge’’ shape on the substrate. The intimate mixing between the two sources at the atomic level was ensured by depositing less than the unit cell (~ 0.4 nm) of BTO/STO at any position on the substrate.

From the preceding discussions, the DCS method can be effectively used in the investigation of a fixed concentration doping on dielectric properties of BST. However, the lack of intimate mixing between precursors at the atomic level may lead to the formation of multi-phase mixtures, even after the necessary heat treatments, deviating from the desired dielectric properties for the device grade BST thin films. Moreover, the DCS method can be designed to explore a selected region of a phase diagram with fine resolution. But, the use of masks during deposition does not allow both fine resolution and broader composition coverage. The masks are also considered to be sources of contamination [194].

Conversely, the CCS method guarantees the intimate mixing between the sources at the atomic level during co-deposition, leading to the formation of BST films with properties close to those obtained from a conventional method. The use of no mask during deposition is advantageous for the CCS method, since the fine compositional resolution as well as broad composition coverage can be achieved [194, 209]. Specially, using the RF-magnetron sputtering technique, a much larger (than those obtained from a PLD based CCS method) spread can be generated [71, 207]. In this chapter, the RF magnetron sputtering based CCS method was applied to BST to identify effective dopants and determine their optimum concentration corresponding to the trade-off between tunability and dielectric loss.

7.3. Combinatorial Setup in This Work

In this study, the CCS combinatorial method based on reactive RF magnetron sputtering with two symmetric (with respect to an axis that passes through the center of a substrate) RF

guns, similar to those proposed in [210, 211], was used. The angular positions of the two guns are adjustable; and they are equipped with equivalent BST targets that are doped with distinct dopants. For the general description of the experimental setup, let's call the two dopants dopant-A and dopant-B. The schematic of the CCS combinatorial setup is shown in Figure 7.1. The BST target doped with dopant-A (i.e. BST+A) is mounted on the left RF source (gun), while the BST target doped with dopant-B (i.e. BST+B) is positioned in the right gun.

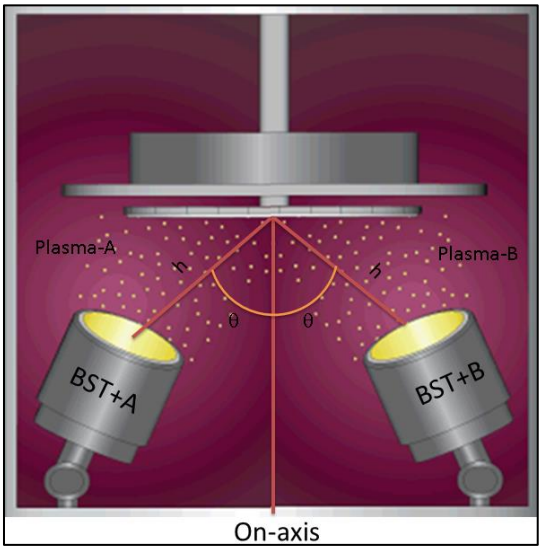

Figure 7.1. CCS combinatorial setup with two symmetric RF sources

The two sputtering guns were shifted and tilted each by the same tilt angle (θ) in the opposite direction from the central axis (on-axis) that passes through the center of the substrate to realize the dopant and thickness gradient across a static (non-rotating) wafer. The distance between the centers of the target and substrate (throw distance) for each source is the same and is represented by *h*. The two sputtering sources were powered by separate RF power supplies of 150 W that ramp at slow rate of 2.0 W/min to avoid the targets cracking. Silicon or platinized alumina substrates were used in the study.

The CCS method is based on the realization of a spatially varying composition across a wafer to acquire a combinatorial library out of which 'sweet spot' for the best tunability and dielectric loss is obtained. The tilt of the RF sources (Figure 7.1) creates a gradient in thickness across the wafer, which in turn is responsible for the gradient in composition. In our case, since the BST sources are doped with distinct dopants, the gradient in thickness leads to the gradient in concentration of the individual dopant. For example, as one goes to the side of source (BST+B) from the source (BST+A) on the substrate, the concentration of the dopant-A decreases while that of dopant-B increases.

Although a thickness gradient from an individual source is required to realize the CCS method, obtaining a uniform film on the entire substrate is crucial from the two sources. The BST film thickness, *t*, is one of the parameters that defines the device capacitance, $C = \varepsilon_r\varepsilon_0 A/t$, where *A* is the electrode area. Furthermore, the permittivity, tunability, control voltage, power handling capacity, and the break down voltage of the film are thickness dependent [180, 212, 213]. Therefore, the thickness variation across the wafer makes the final data interpretation challenging as it is impossible to identify whether the observed changes in properties are due to the introduced dopants or the thickness variation.

7.4. Thickness and Composition Profiles

Generally, in RF magnetron sputtering, the uniformity of a film is ensured by rotating the substrate during deposition. However, with no substrate rotation during combinatorial film deposition, the uniformity of the film can only be realized by adjusting the guns geometry—tilt angle and the throw distance. In order to determine optimal tilt angle and throw distance, the thickness profile on the substrate from each of the source target was first mathematically modeled and then experimentally tested.

7.4.1. Thickness Profile Modeling

The thickness profile of a film deposited by RF magnetron sputtering with the centers of target and substrate coinciding (i.e. no target tilting) was studied by Swann [88] based on a standard Holland [214] method. In this work, the expression for the thickness profile of a film deposited from a tilted target as a function of tilt angle, θ, and throw distance, h, was derived, where the details of the calculations are given in appendix B. Assuming t_A and t_B to be the time rate of thickness of the film deposited from targets BST+A and BST+B, respectively, their expressions are presented as

$$t_{A,B} = \frac{S_{A,B}}{\pi^2 \rho_{A,B}({r_2}^2 - {r_1}^2)} \int_{r_1}^{r_2} \int_0^{2\pi} \frac{\cos\theta\left(2h^2 \pm 2rR\cos\varphi(\cos\theta - \sec\theta) \pm 2hR\sin\theta \pm 2hr\tan\theta\right)}{2(h^2 + r^2 + R^2 + 2rR\cos\theta\cos\varphi \pm 2hR\sin\theta)^2} r\, dr\, d\varphi, \quad (7.1)$$

where, "+" or "-" as well as the subscript "A" and "B" correspond to the expression for t_A and t_B, respectively; θ is tilt angle, h is the throw distance, S_A and S_B are the sputtering rates, ρ_A and ρ_B are the densities, and R is an arbitrary position on the substrate from its center. The parameters r_1 and r_2 are known as the inner and outer radii of the "erosion" region (see Figure B1 (a) in Appendix B) of the target. In the absence of the magnet, r_1=0, and r_2 equals the radius of the target. Lastly, r is an arbitrary radius between r_1 and r_2 (i.e. $r_1 \leq r \leq r_2$) on the target.

When deposition is performed from the two sources (i.e. co-deposition), the total thickness of the film on the substrate is the sum of the thickness from each source as

$$t(R) = t_A(R) + t_B(R). \quad (7.2)$$

Like-wise, the expression for the weight percent (wt. %) composition [210] of the deposited material on the substrate is estimated as (see Appendix B)

$$\%A(R), B(R) = \frac{\rho_{A,B} t_{A,B}(R)}{\rho_A t_A(R) + \rho_B t_B(R)} \times 100\%, \quad (7.3)$$

where, % A(R), % B(R) are the wt.% of the material deposited from the BST+A and BST+B sources as a function of position on a substrate, respectively. The concentration of each dopant at a given position on a substrate can be estimated with the knowledge of the relation between concentrations of each dopant with respect to the bulk material.

The effect of tilt angle and throw distance on the thickness uniformity and deposition rate were studied. Since the analytical expression above cannot be simplified further, the thickness calculation was performed numerically using the MATLAB programming language. The parameters used in the calculation are r_1=0, r_2=3.8 cm, S_A=S_B=2.06x10^{-4} g/sec (measured for aluminium metal target), ρ_A=ρ_B=5.6 g/cm^3 (densitiy of the BST+A and BST+B target). The plot of the thickness versus distance on the substrate is presented in Figure 7.2A with varying tilt angles and fixed throw distance (16.5 cm). When the tilt angle is small (< 20^o), the film shows a non-uniform thickness profile with a big 'hill' in the center that decrease outwards. Conversely, when the tilt angle is large (> 40^o), the profile shows thicker film on the periphery and a big 'hole' in the center of the film. The optimum tilt angle for growing a uniform thin film is found to be 30^o.

The effect of throw distance (*h*) on the thickness profiles of the film using the 30^o tilt angle is shown in Figure 7.2B. As shown in the figure, when the throw distance is small (below 12 cm), high deposition rate is obtained, but the uniformity of the film is compromised. Given the importance of uniformity in combinatorial film deposition, the throw distance of 16.5 cm was selected though it slows down the deposition rate. Therefore, to obtain a uniform combinatorial thin film, the tilt angle and throw distance of the two RF sources should be set to 30^o and 16.5 cm, respectively.

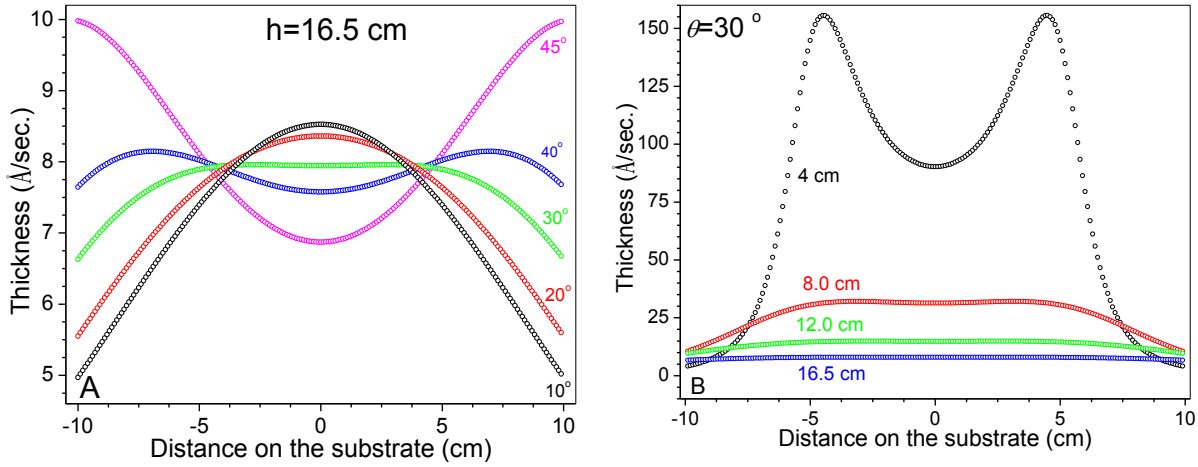

Figure 7.2. Thickness versus distance on a substrate: effects of tilt angle (A) and throw distance (B) on the films' growth rate and uniformity

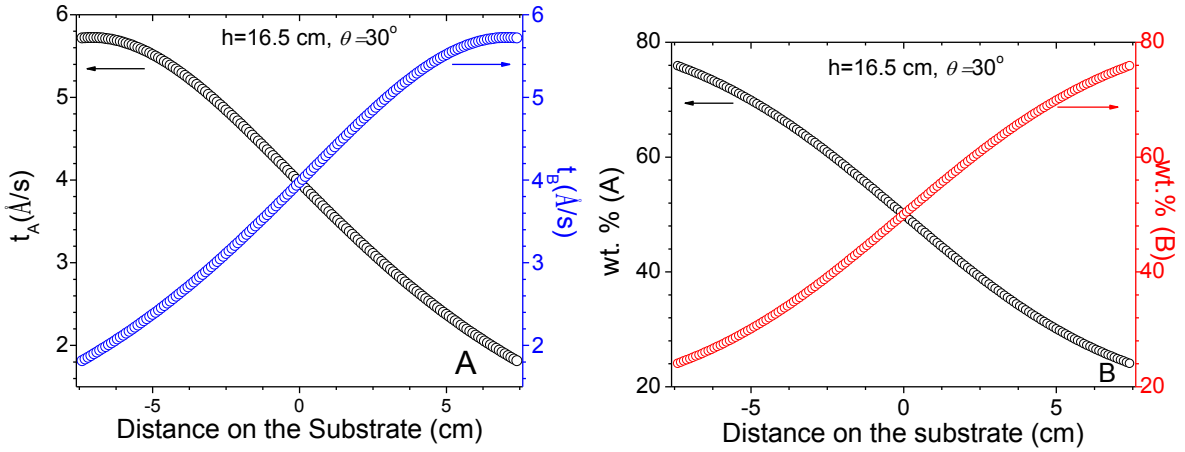

Figure 7.3. Thickness (A) and concentration (B) gradient on the substrate

Based on the optimum tilt angle and throw distance, the thickness and composition profiles calculated from each target are presented in Figure 7.3. The thickness of the film obtained from both targets (Figure 7.3A) decreases quasi-linearly with the thicker film close to the edge of the wafer on the side of the target. The weight percent (wt.%) composition (calculated based on Eq. (7.3), Figure 7. 3B) from each target also shows the gradient in compostion across the wafer, with the highest concentration close the source targets. These results prove the aplicability of the CCS combinatorial method in our RF sputtering system.

7.4.2. Experimental Test of the Combinatorial Setup

Using the tilt angle of 30^{o} and throw distance of 16.5 cm obtained from the mathematical model above, the two RF guns were adjusted to experimentally test the combinatorial geometry. Then, two BST films were deposited on separate 6" silicon wafers at room temperature for 4 hours. One of the two films was deposited from the target (BST+A), while the other was from the target (BST+B). The thickness of the films was measured by ellipsometery from 14 locations along the line connecting the two targets on the wafer in an interval of 1 cm. Figure 7.4 shows the thickness profiles of the BST films deposited from each target. The thickness from each target decreases with distance on the substrate away from the side of the wafer that is close to the target, showing analogous thickness profile with the model above (Figure 7.3A). The result indicates the realization of the CCS method in our RF magnetron sputtering system when the two RF guns are adjusted to the geometry estimated from the above model.

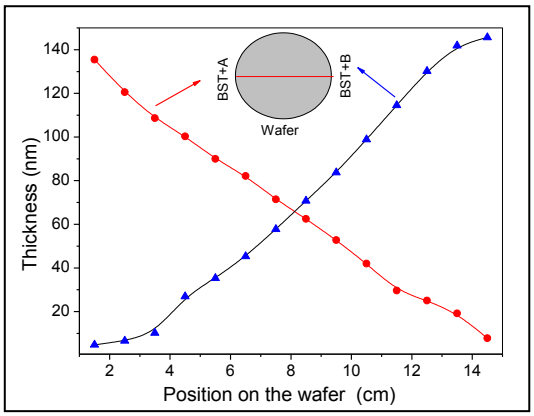

Figure 7.4. Film thickness versus position on the wafer. The red line in wafer scheme shows the path on which the thickness was measured

To verify whether a uniform film can be grown at this geoemetry, BST thin film was co-deposited from the two targets on a 4" silicon wafer at room temperature. The 3D thickness map

of the entire wafer (measured by ellipsometery) is shown in Figure 7.5. As can be seen from the white colored area on the figure, the region on the wafer between the two targets shows a uniform film. The over all results show a uniformity of ~ 6 %, proving that the tilt angle and throw distances obtained from the above model is optimal for depositing of a uniform combinatorial thin films.

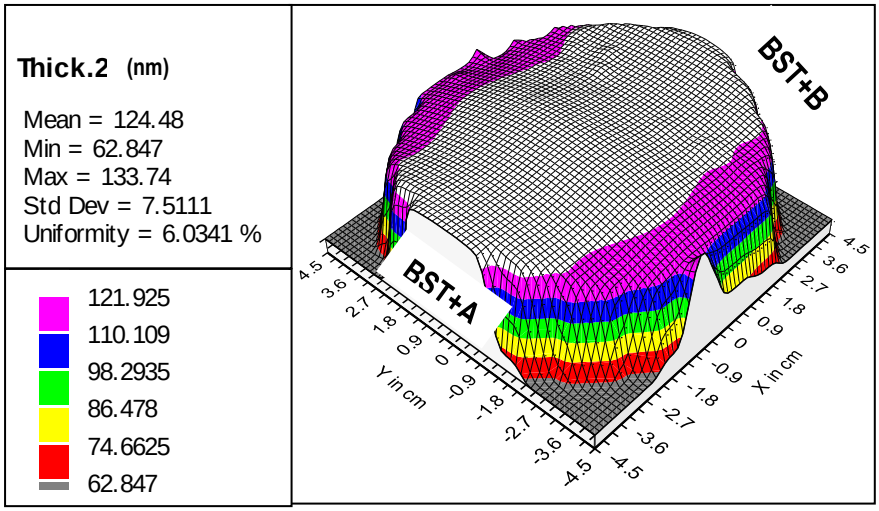

Figure 7.5. 3D thickness map of a film co-deposited on a silicon wafer

7.5. Combinatorial Thin Films for Optimal Dopant Search

Following the experimental test of the RF guns geometry, a BST thin film was co-deposited from the A and B doped BST targets to study the effect of the dopants on the dielectric properties (dielectric constant, tunability, loss, and leakage current) and determine their concentration corresponding to the optimal result. The A and B dopants used in this study are cerium oxide (CeO_2) and barium magnesium niobate ($BaMg_{1/3}Nb_{2/3}O_3$ (BMN)), respectively. The deposition of the film was performed on platinized alumina wafer ($Pt/TiO_2/SiO_2/Al_2O_3$) using the same deposition condition used in chapter 6. Similar to the conventional deposition, a ~10 nm buffer layer was deposited at room temperature to deposit a good crystalline thin film.

After the film deposition, the thickness, crystallinity and phase purity, microstructure and surface morphology of the film were measured and analyzed. The measurements were performed from five spots (top, left, center, right and bottom) on the wafer as shown in Figure 7.6; where, the left and right regions of the wafer are rich with Ce and BMN dopants, respectively. The tunability, dielectric loss, and figure of merit (FOM) of the film were measured from over 2000 pairs of metal-insulator-metal capacitors (reasonable statistics); and an elemental analysis was conducted on 28, 16x16 mm^2 samples. Finally, the composition and dielectric properties were correlated to determine the optimal concentration of the dopants.

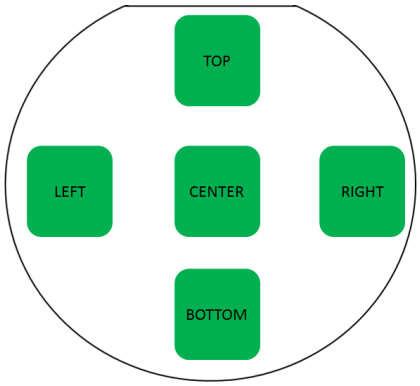

Figure 7.6. Spots on a wafer from which XRD, SEM, AFM, and thickness were measured

7.5.1. Structure and Morphology of the Combinatorial Film

The thickness of the film was measured by ellipsometry from five spots (Figure 7.6) and averaged to be about 240 nm with a reasonably good uniformity (~2 %), suggesting that the thickness non-uniformity does not interfere with the data interpretation (i.e. if there is a change in the dielectric properties across the wafer, it is exclusively from the dopants introduced into the material). The XRD scan was performed on the film to diagnose the crystallinity and phase purity of the grown material. Figure 7.7 shows the grazing incidence XRD (GIXRD, $\gamma = 1.5^{o}$) of

the combinatorial thin film from the five spots. The patterns acquired from all the spots have shown cubic polycrystalline BST material which is in agreement with the reported results [107]. In addition, the absence of extra phases in all the GIXRD patterns suggests that the concentration of the dopants in the film is lower than their solubility limit.

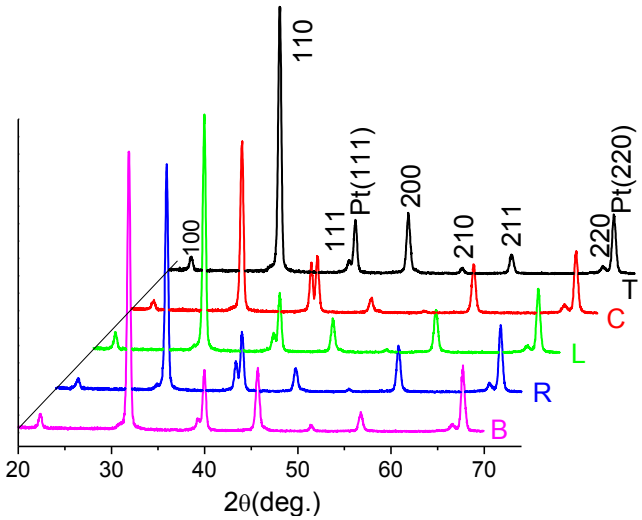

Figure 7.7. GIXRD of the combinatorial thin film acquired from, B (bottom), R (right), L (left), C (center) and T (top)

The effects of dopants on BST film was studied by calculating the lattice constant and crystallite size [97] for the five spots using the strongest (110) peak. The lattice parameters calculated for all spots shows comparable values (Table 7.1.), indicating that the dopants have uniform effects on the lattice of BST. However, the dopants may affect the broadening (crystallite sizes) of the XRD lines differently. As can be seen in Table 7.1, the crystallite size estimated for the right region of the film has shown a relatively lower value compared to the rest of the regions.

To further explore the grain structure and surface morphology of the film, SEM and AFM images were taken from the five spots on the film. Figure 7.8 shows the field emission scanning

electron microscopy (FESEM) micrographs taken from the five regions. The images from all the spots show crack free surfaces, indicating that the film has good insulating properties that withstand large bias voltages without device burning.

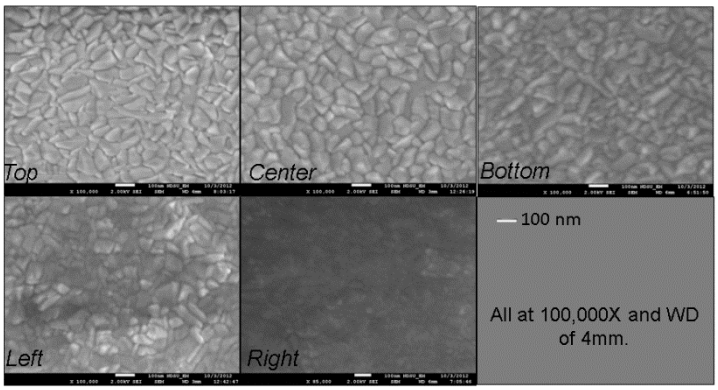

Figure 7.8. FESEM micrographs of the combinatorial film acquired from the Top, Center, Bottom, Left and Right regions

Table 7.1. Lattice constants, crystallite/grain sizes for the combinatorial thin film

Parameters	Measured spots on the wafers				
	Top	Center	Left	Right	Bottom
Lattice constant (Å)	3.969	3.968	3.968	3.968	3.969
Crystallite size (nm)	22.6	22.5	22.7	22.3	22.8
Grain size (nm)	47.1	53.0	49.6	--	50.8
Surface Roughness (nm)	5.04	8.65	2.94	0.94	5.54

As shown in the figure, the images taken from the top, center, bottom and left regions have shown larger grains and definitive microstructures contrary to the image taken from the right region of the film. The grain size for all the spots except the right region (unresolved grains) was estimated using the lineal intercept method [162] and presented in Table 7.1.

The AFM images taken from a scan area of 1x1 μm^2 for each region are shown in Figure 7.9. The images show that all regions have exhibited no cracks, defects, and visible pinholes on the surfaces. Similar to the SEM result, all images except the one

taken from the right region have shown well-defined and resolved grain structures. The surface roughness estimated from the AFM images are presented in Table 7.1.

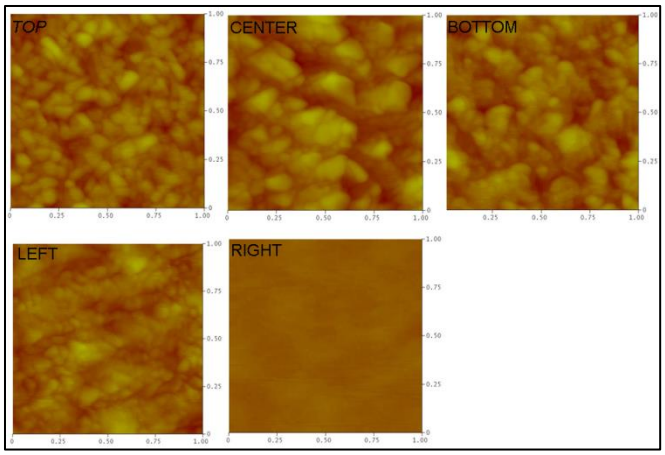

Figure 7.9. AFM images of the combinatorial film acquired from the Top, Center, Bottom, Left and Right regions

The AFM result has shown that the right region of the film is the smoothest of all the regions, in agreement the smallest grain size observed in the XRD and SEM results. The central region of the film has shown higher surface roughness than the flat and top regions that have comparable roughness values as well as the left region which is Ce-rich. The reduction in grain size and the smoother surface roughness of the right region of the film are likely due to the high concentration of Mg and Nb dopants. This is likely since the right side of the wafer is close to the BMN doped target, which as a result of the pinning effects of the two dopants on the grain boundary, reduces the grain sizes of the film [70, 144].

It is known that when the film surface is rough, the film-electrode interface quality is poor and contributes to the conductor loss of the device [34], suggesting that the smooth right (BMN rich) region of the combinatorial film has lower dielectric loss compared to the rest of the regions [144]. In addition, the smoother film surface reduces

the leakage current, which is consistent with the high film resistivity obtained from the right (BMN rich) region of the combinatorial film [164, 165].

7.5.2. Electrical Characterization of the Combinatorial Film

After the structural, phase purity, and morphological characterization, parallel plate capacitors were lithographically patterned (2432 pairs of capacitors connected in series) to measure the dielectric and electrical properties of the film (see Appendix A). The relative tunability, n_r (%), and the quality factor (Q) were mapped by varying the external bias voltage from 0 V to 32 V and back to 0V in the interval of 2 V at a constant frequency of 30MHz.

The 2D map of dielectric constant (at 0V), tunability (n_r %) and quality factor (Q) of the entire combinatorial thin film are shown in Figure 7.10. The color bands on the wafer(Figure 7.10 A&B) indicates the presence of gradients both in dielectric constant and tunability along the deposition X-axis (projection of an axis connecting the two sputtering sources on the wafer) as one goes to the right end of the wafer, where high concentration of BMN dopant is expected. The maximum permittivity and tunability are obtained from the left (close to the Ce-doped BST target). The decrease in permittivity and tunability on the right side of the wafer is consistent with effect of Mg in BST [34, 68]. On the other hand, the Q-map on the entire film (Figure 7.10C) does not show any apparent differences and there is no defined trend of Q unlike tunability. However, a tiny strip close to the right edge of the wafer presents high Q-factor values compared to the other regions. This is due to Mg/Nb rich BST that effectively decreases the dielectric loss of the BST film [144].

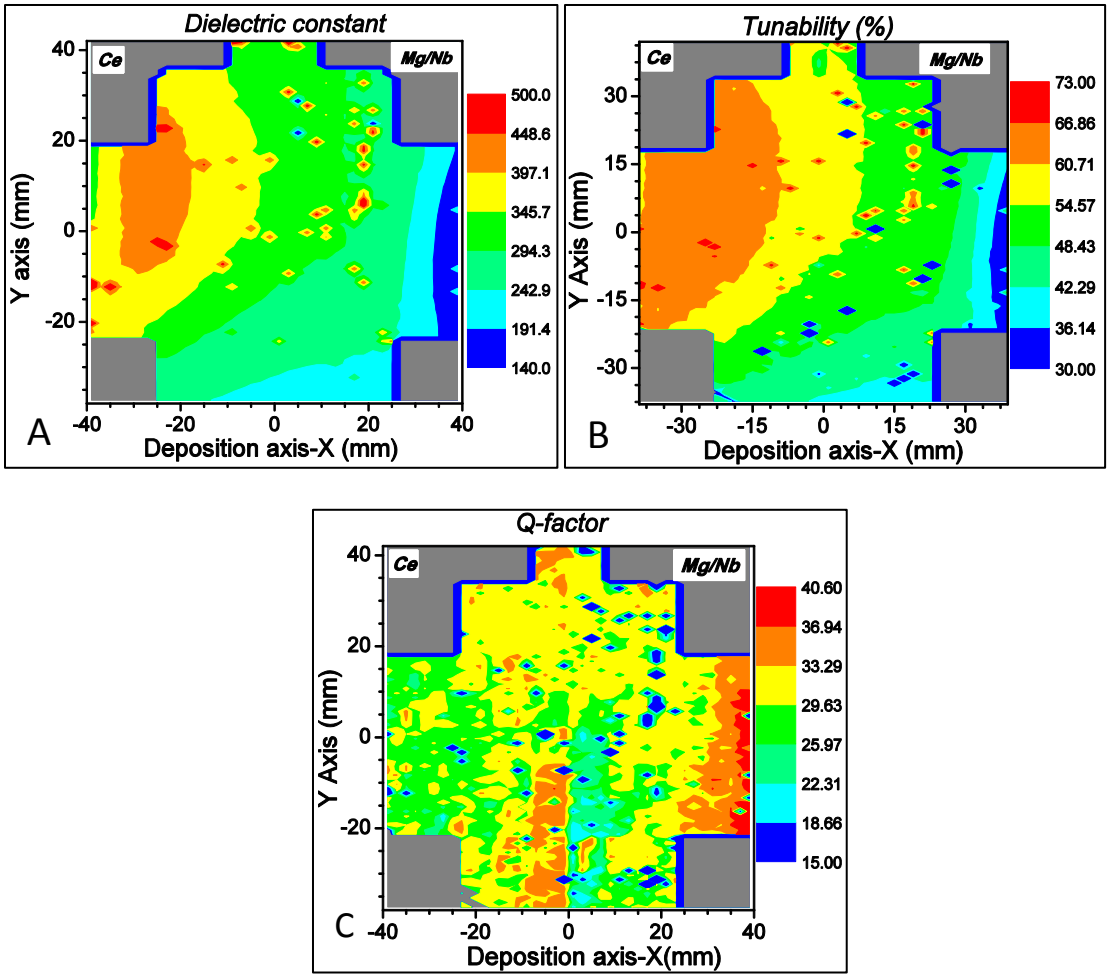

Figure 7.10. The 2D map of permittivity at 0 V (A), relative tunability (B), and quality factor (C) for the combinatorial thin film

The other important property that needs to be explored is behavior of the resistivity of the film on the wafer. Due to the lack of automated equipment to measure the leakage current of all the devices, only representative devices were manually measured. The devices were selected from the region between the sputtering sources as shown in Figure 7.11 by dies (boxes) on the mask layout labeled by rows (*A, B, C, D, and E*) and columns (*1, 2,…10*). This region was intentionally picked as the gradient in the dopant concentration is realized in the region that lies between the two sputtering targets. In each die (i.e. A1, A2…A10, B1…E10), one device was selected for leakage current measurement.

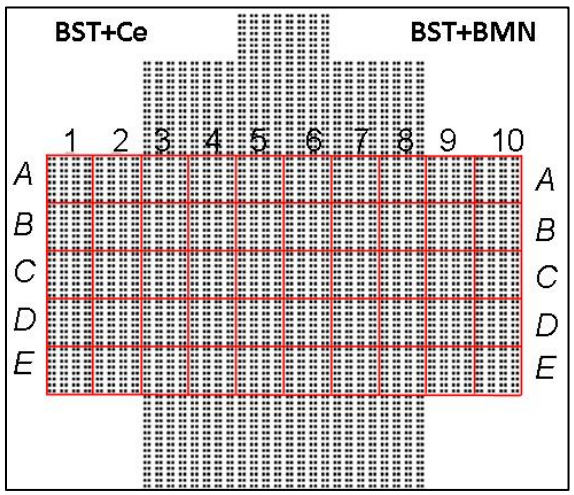

Figure 7.11. Regions selected for the leakage current measurements

The leakage current (value at 32 V) and tunability of the devices (both measured from the same device) versus deposition X-axis for the rows (indicated in Figure 7.11) are shown in Figure 7.12. From the left (Ce-rich) to right (BMN-rich) region of the film along each row, the tunability decreases, showing a similar gradient as observed by the color map in Figure 7.10B. At the two end points, the leakage current is observed to be small; however, the BMN rich region has shown the lowest leakage current of all the regions. The small current in either end of the film is attributed to the lower surface roughness in the right and left regions of the film which might have improved the film-electrode interface and thus the leakage current [164, 165]. Likewise, the higher leakage current measured from the center is related to the rough surface (see Table 7.1). The lowest leakage current measured from the BMN rich region is likely due to the charge compensating effect between the Mg^{2+} and Nb^{5+} ions [70, 144], introducing no free carrier in the material.

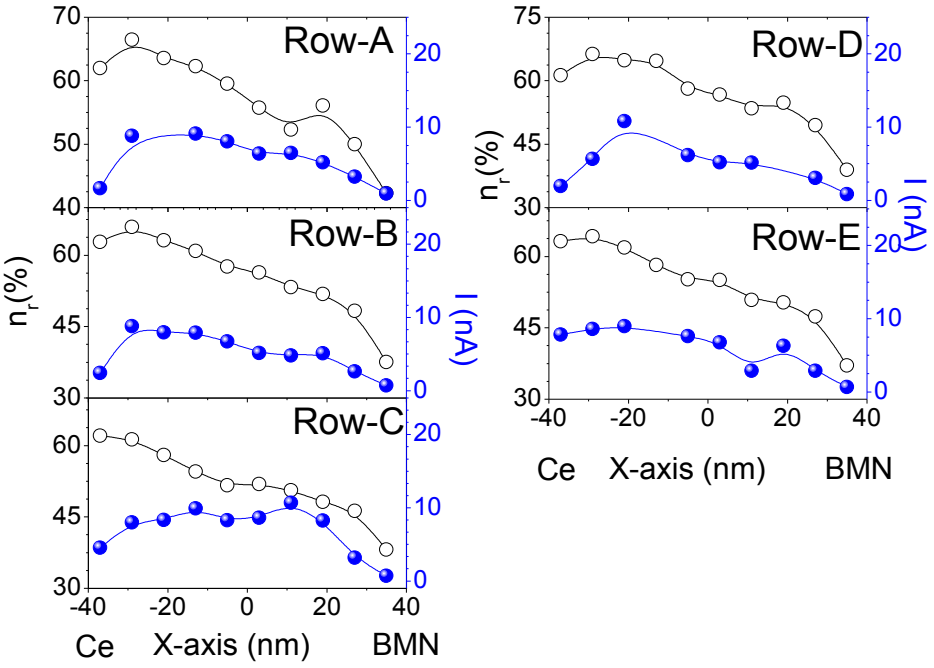

Figure 7.12. Tunability and leakage current vs. deposition X-axis for selected devices. The Ce and BMN rich sides of the film are indicated on the graph

7.6. Composition Library for Combinatorial Thin Film

In order to determine the optimal concentration of the dopants using the combinatorial method, it is vital to establish a library and correlate its composition with the dielectric properties. To achieve this, a BST film was deposited on a SiO_2/Si wafer (4") from the two BST (Ce+BST and BMN+BST) targets using the same conditions as for the film deposited on the platinized alumina wafer. The thickness and GIXRD patterns of the film was comparable (data not shown) with the film grown on the platinized alumina wafer.

As in the leakage current measurement, the composition analysis on the film was performed manually due to the lack of automated equipment. To realize this, the 4" wafer was diced into 28, 16x16 mm^2 samples as schematically shown in Figure 7.13. For convenience, the

samples are labeled as E1, E2…E28 and the elemental analysis was performed on each piece by XRF and ICP-OES methods.

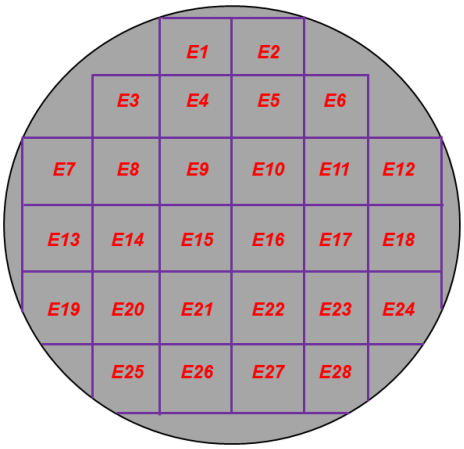

Figure 7.13. Wafer diced to 28, 16x16 mm^2 samples for composition analysis

By using the XRF method, the concentration of both dopants can be quantified for each sample in the library; however, with the ICP-OES technique, the analysis on individual sample has shown no presence of Mg and Nb (proved on a different combinatorial film). It is known that the niobium atom is undetectable by the ICP-OES [101], but the absence of Mg from the analysis was unanticipated. The likely cause for absence of Mg from the analysis on each piece could be due to the dilution of its concentration in the combinatorial film as a result of deposition from two BST sources. In order to obtain a measurable Mg concentration in the ICP-OES analysis, three samples were digested in the volume (~ 5 ml) that was used to make one sample (i.e. tripling the concentration). The ICP-OES analysis performed on the sample proved that digesting three pieces to produce one ICP-OES sample ensures a measurable Mg concentration. Consequently, the ICP-OES analysis of the combinatorial film was conducted on six samples comprising E7 to E24 out of the 28 samples in the library. In each of the six ICP-OES samples, three pieces (samples) that are in the same column were digested together to create one ICP-OES

sample. The six ICP-OES samples and the corresponding digested pieces from the library to make one ICP-OES sample are presented in Table 7.2.

Table 7.2. ICP-OES samples and the corresponding digested samples from the library

ICP-OES samples	Digested samples from the library
ICP-OES1	E7+E13+E19
ICP-OES2	E8+E14+E20
ICP-OES3	E9+E15+E21
ICP-OES4	E10+E16+E22
ICP-OES5	E11+E17+E23
ICP-OES6	E12+E18+E24

7.6.1. XRF Analysis

The 2D maps of the concentrations of Ce and Nb (Nb is part of $BaMg_{0.33}Nb_{0.67}O_3$) dopants (mol. %) measured by XRF method for each sample in the library (on the wafer) are presented in Figure 7.14. The center of each sample on the wafer was taken as a position to graph the 2D map. The observed bands of colors show the presence of compositional gradient for both dopants across the substrate, leading to the gradient of tunablity and permittivity as observed above. Unfortunately, the compositional map for Mg is not presented, since its value for all the samples was found to be below the instrumental detection limit. This could be due to the dilution of Mg concentration in the film (as was the case for the ICP-OES analysis on the individual samples) and the low atomic number of Mg. It is known that the instrument detection limit decreases when the matrix composition has lower atomic number (Z) which could be due to the smaller cross-section of Mg to interact with the X-ray photon [215]. Yet, knowing the concentration of Nb is sufficient to estimate the total amount of BMN in a given sample.

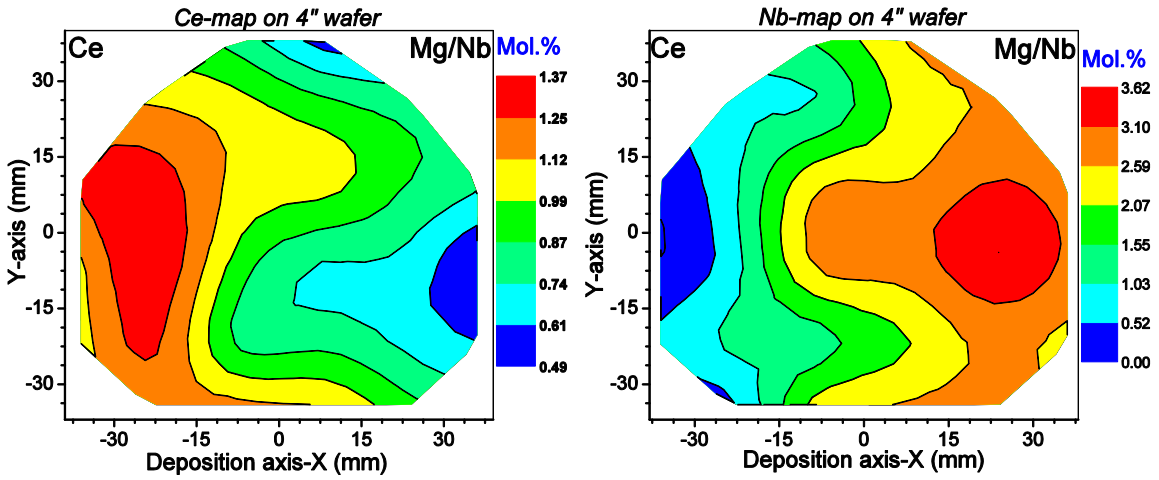

Figure 7.14. The 2D XRF maps of Ce (left) and Nb (right) dopants for the combinatorial film

In order to correlate the dielectric properties with the dopants concentration, the tunability and quality factor of the devices within each sample was averaged. The average tunability (n_{av}) and quality factor (Q_{av}) were calculated based on the number of devices, N (different for various samples), inside each sample as

$$n_{av} = \frac{\sum_{i=1}^{N} n_i}{N}, \; Q_{av} = \frac{\sum_{i=1}^{N} Q_i}{N}. \tag{7.4}$$

where, n_i *and* Q_i are the tunability and Q-factor of individual device in a sample, respectively. The tunability and Q data reduce to 28 values matching the number of samples for the composition analysis via XRF.

The 2D map of the average tunability of the combinatorial film is shown in Figure 7.15 (left). The tunability map shows a gradient which follows the same tendency with the concentration of the Ce dopant on the wafer (Figure 7.14), suggesting the increase in the concentration of Ce is responsible for the improvement of the tunability. The Quality factor, however, does not show an observable trend with the concentration of the dopants, except for the high Q at the far right end of the wafer (data not shown) due to the high concentration Mg/Nb dopants [144].

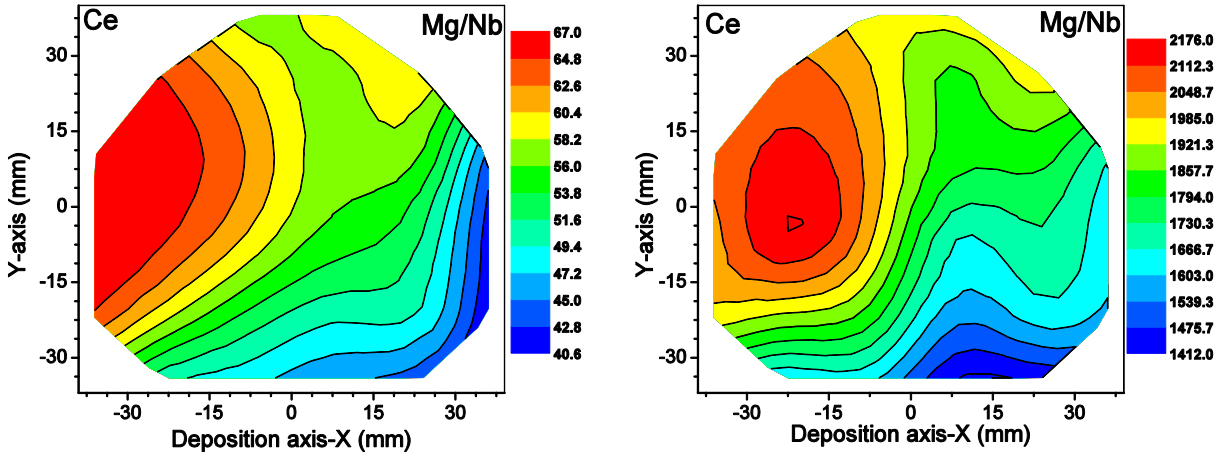

Figure 7.15. The 2D map of average tunability (left) and FOM (right) for the combinatorial film

The trade-off between tunability and dielectric loss can be tested through an average figure of merit ($FOM_{av}= n_{av}\times Q_{av}$) as shown in Figure 7.15 (right) on the entire wafer. The color map shows the gradient of FOM_{av} on the wafer with the maximum (>2100 %) on the region with high concentration of Ce. Precisely, the maximum FOM_{av} of ~2174 % (matching to average tunability of ~65 % and tan δ of~ 0.0299) was measured. This spot corresponds to the optimal concentrations of Ce and BMN dopants of 1.37 mol. %, and 1. 67 mol. %, respectively.

7.6.2. ICP-OES Analysis

The ICP-OES analysis was conducted on six ICP-OES samples as described in Table 7.2. The curves for Mg (Mg is a part of $BaMg_{0.33}Nb_{0.67}O_3$) and Ce (mol. %) are shown in Figure 7.16. The result presents gradients of composition (albeit complex), which is characteristic of the multicomponent continuous composition spread that was targeted in this experiment. The tunability (averaged over all devices in an ICP-OES sample) is also plotted with the composition curves (see the blue line in Figure 7.16). The tunability value of 62.0 % (dashed line) is ~15 % higher than that for only BMN doped BST [144]. Conversely, the loss $tan\delta = 0.03$ for the latter is only marginally lower than this value for the sample ICP-OES2 (0.035) suggesting that doping

with Ce ions (in combination with BMN) enabled a substantial tunability increase and prevented increase in loss. The analysis on the ICP-OES2 sample has shown concentrations of CeO_2 and BMN 1.22 mol % and of 1.65 mol %, respectively, which are comparable with the XRF result above. Therefore, a BST target doped with ~1.66 mol. % of BMN and ~ 1.30 mol. % of CeO_2 can be recommended for the fabrication of a good quality BST thin film for tunable microwave components.

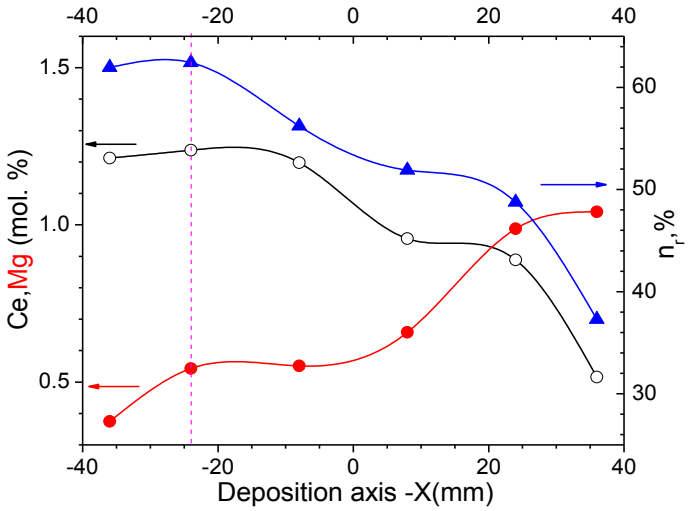

Figure 7.16. ICP-OES analysis of Ce and Mg concentrations, and average tunability vs. position on the wafer

7.7. Conclusions

An RF magnetron sputtering based continuous composition spread (CCS) combinatorial thin film method was applied to BST thin film to optimize its properties via multi-doping. The BST thin film was co-deposited from CeO_2 and $BaMg_{0.33}Nb_{0.67}O_3$ (BMN) doped BST targets with the aim of understanding the effects of the dopants on the properties of BST film and determining their optimum concentration corresponding to the trade-off between tunability and

dielectric loss in a timely fashion. Accordingly, the optimum concentrations of the dopants were determined.

The library created in this work has generated 28 samples from one combinatorial film deposited on 4" wafer in one deposition process that runs for 10 hours. If each sample was to be deposited separately from a single sputter target, we would need 28 discrete depositions, each with 20 hours deposition time to obtain ~ 240 nm thick film. The total process requires over 23 days of consecutive deposition times! Moreover, each sample requires a unique sputtering target with known dopant concentration which is a costly and time consuming process. Therefore, the combinatorial method used for BST is faster and less expensive than traditional approaches in finding the "sweet spot" corresponding to the optimal concentration of the three dopants (Ce, Mg, and Nb) needed to fabricate good quality BST based agile microwave devices.

8. CONCLUSIONS AND FUTURE OUTLOOK OF THE WORK

8.1. Conclusions

In summary, this thesis was devoted to improving the properties of barium strontium titanate through buffer layer deposition, stoichiometric control, concurrent doping, and use of combinatorial thin film method to study the effect of multiple doping. The crystallinity of the BST film on platinized substrates was achieved by using a thin BST buffer layer (homo-buffer) deposited at room temperature which acts as a seed layer for the growth of the main body of the film. The rise of the total gas pressure in the chamber (>/= 30 mTorr) during film deposition has enabled the attainment of a one to one correspondence between the composition of the target and film BST. However, the O_2/Ar ratio should be adjusted as exceeding a threshold of 2 mTorr in oxygen partial pressure facilitates the formation of secondary (undesirable) phases.

Mg/Nb co-doping in BST through complex $BaMg_{0.33}Nb_{0.67}O_3$ (BMN) oxide has considerably improved the properties of BST thin films. The doped film has shown an average tunability of 53 %, which is only ~8 % lower than the value for the undoped film. This drop is associated with the Mg ions, but its detrimental effects are partially compensated by Nb ions. Conversely, the doping has reduced the dielectric loss by ~40 % leading to a higher figure of merit, making the BMN doped film a candidate for application in agile microwave devices compared to the undoped film. Moreover, doping through BMN ensures charge neutrality compensation and results in significant leakage current reduction. Also, the presence of large amounts of empty shallow traps related to $Nb_{Ti}^{\bullet}$ localizes the free carriers injected from the contacts; thus increasing the device control voltage substantially (>10 V).

The carrier transport mechanism for the undoped and BMN doped film was investigated. The conduction for the undoped film was interface limited while the BMN doped film was bulk

limited. The change of the conduction mechanism from SE to PF is attributed to the presence of large number of $Nb_{Ti}^{\bullet}$ sitting as a positive trap center at the shallow donor level of the forbidden gap of the BST film.

The effects of multiple doping (Mg, Nb, and Ce in this work) were studied by successfully applying a RF magnetron sputtering based continuous composition spread (CCS) combinatorial thin film method. The method was based on co-sputtering of BST thin film from CeO_2 and $BaMg_{0.33}Nb_{0.67}O_3$ (BMN) doped BST targets followed by fast electrical and analytical characterization. The correlation between the electrical properties and composition of the film helps determine the optimum concentration of dopants corresponding to the trade-off between tunability and dielectric loss in a timely fashion. Accordingly, the concentrations of Ce and BMN (containing Mg and Nb) of 1.30 mol. % and 1.66 mol. %, respectively, were recommended for obtaining a good quality BST films for tunable microwave applications.

8.2. Future Outlook of the Work

8.2.1. Concurrent Al/V dopant for BST

In chapter 6, the effect of concurrent Mg/Nb doping was studied. The combination ensures charge neutrality and reduces the loss and leakage current of the film without significantly dropping the tunability. Similar mixtures of other dopants may have an equivalent effect. One possible blend of dopants to realize the charge neutrality condition can be aluminum and vanadium (Al/V). The two atoms can be introduced into BST through a single phase aluminum orthovanadate ($AlVO_4$) which realizes the neutrality condition by satisfying ($[Al'_{Ti}] = [V_{Ti}^{\bullet}]$) relation.

Two synthesis routes for $AlVO_4$ from aluminum nitrate none-hydrate ($Al(NO_3)_3.9H_2O$) and vanadium (V) oxide (V_2O_5) precursors were reported in [216]. The first route bases on direct

mixing of Al $(NO_3)_3.9H_2O$ with V_2O_5 in nitric acid, while the second one involves dissolving V_2O_5 in tetramethyl ammonium hydroxide ($(CH_3)_4NOH$) before mixing it with $Al(NO_3)_3.9H_2O$ in H_2O in nitric acid. While both methods can be equally used to synthesize the compound, the second route it was found to ensure an intimate mixing between the two precursors and promotes the formation of single phase $AlVO_4$. Based on the second route, 20 grams $AlVO_4$ was synthesized and doped to the base BST powder to fabricate an $AlOV_4$ doped BST target (following the solid state reaction procedures in Chapter 4). The target was fabricated and its crystallinity was studied by XRD and is ready for machining and metal bonding to deposit film. These concomitant dopants are believed to show similar effects when compared with the BMN dopant, and have the potential to improve both the loss and tunability of the BST thin film.

8.2.2. Effect of Electrode Area on Dielectric loss

One major problem observed in the course of this work was the high dielectric loss of the devices which is mainly due to the contribution from the large area of the electrode ($0.5x0.5mm^2$). Using a highly conductive and thick electrode with a small plate area is important to minimize the contribution of the electrode to the device losses. In addition, it is also important to mention that the electrode loss depends on the geometry of the device [217]. One of the electrode geometries used for this purpose consists a central circular patch surrounded by concentric circles (Figure 8.1, left) [105].

To test the effectiveness of the new capacitor structure, a mask with variable diameter of the central patch (20 μm, 30 μm, 40 μm, and 50 μm) was fabricated and applied in capacitor fabrication of a BMN doped BST film which was deposited on platinized alumina wafer using the same deposition condition as the one in Chapter 6. The film was 242.7 nm thick and its GIXRD pattern showed a pure phase polycrystalline BST material. The RF measurements were

performed by a ground-signal-ground (GSG) probe with a 250 µm pitch (probe tip spacing) as shown in Figure 8.1, right.

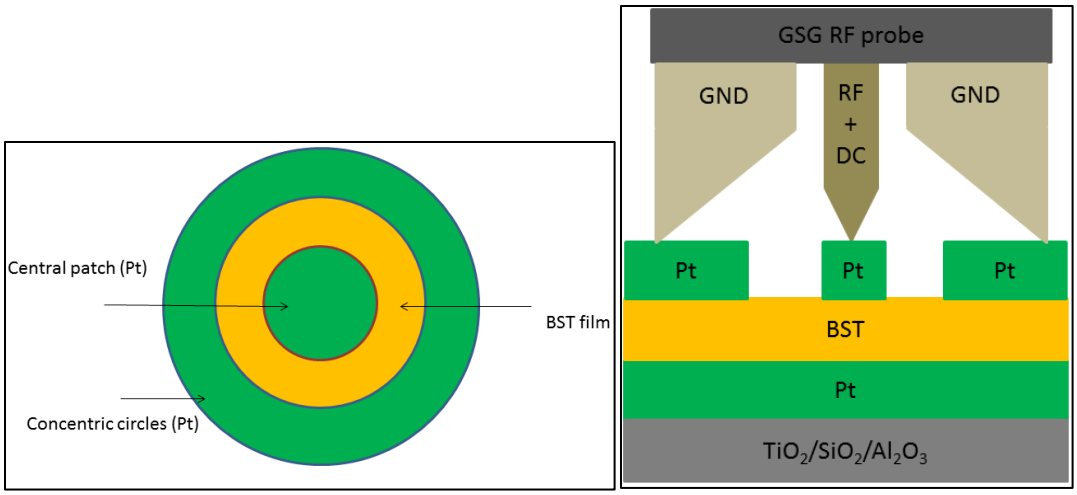

Figure 8.1. Top view (left) and cross section with GSG probe (right) of the new capacitor structure

With these capacitor structures, the capacitance and Q-factor measurements were performed at 30 MHz and 2 GHz frequencies on representative device for each central patch diameter of 20 µm, 30 µm, 40 µm, and 50 µm. Interestingly, regardless of the area, all the devices have shown tunability of ~63 % (at 660 kV/cm bias field) for both frequencies. However, the quality factor has shown a decrease with the increase of frequency as well as the diameter of the central patch (i.e. Q is area dependent).

The quality factors and tunability for the four representative capacitors at 30MHz and 2 GHz frequencies are presented in Table 8.1. For comparison purposes, the values obtained from the BMN doped BST film with a capacitor area of 0.5x0.5 mm^2, measured at 30 MHz frequency is included in the table. From the table, one can see that the highest Q is obtained for small area device, indicating the reduction of electrode contribution to the total dielectric loss. Therefore, this result shows the need for using the new capacitor structure for measuring a reduced

dielectric loss both in the conventional and combinatorial BST thin films without affecting the tunability. The expected loss gradient on the combinatorial film may also be revealed by using these small area capacitor devices.

Table 8.1. Q-factor of capacitors with the four diameters at 30 MHz and 2 GHz

	20μm	30 μm	40 μm	50 μm	MA2457*
Q@30 MHz	132.2	118.1	120.7	99.6	~ 32.4
Q@2 GHz	28.2	22.8	14.4	13.3	--
Tunability (%)	63.4	63.4	63.5	62.7	62.4

* BMN doped film patterned with 0.5x0.5 mm^2 area top electrode.

8.2.3. Three Sputtering Sources for Combinatorial Approach

The continuous composition spread (CCS) combinatorial method has been realized as a fast and cost effective way of studying the effects of multiple-dopants on BST. With the existing set up, performing more iteration to precisely determine the concentration of the dopants in the film is necessary. On the other hand, it is also possible to use three sources to increase the number of dopants in BST and determine their effects. The Mg/Nb, Al/V co-doped and CeO_2 doped BST targets can be co-sputtered on a substrate and the effect of the dopants and their optimal concentration can be determined in a cost effective and timely manner.

REFERENCES

[1] GSM Bands information by country (October 10,2014) *World Time Zone Website.* Retrieved November 15, 2014, from http://www.worldtimezone.com/gsm.html

[2] A. R.Rofougaran, M.Rofougaran, A.Behzad, Radios for Next Generation Wireless Networks, IEEE Microw. Mag. **6,** (2004) 38.

[3] S.Gevorgian, Agile Microwave Devices, IEEE Microw.Mag. **93**, (2009) 1529.

[4] F. Reggia, E. G. Spencer, A New Technique in Ferrite Phase Shifting for Beam Scanning of Microwave Antennas, Proc.IRE. **45**, (1957) 1510.

[5] A.G. Fox, An adjustable waveguide phase changer, Proc. IRE. **35**, (1947) 1489.

[6] A. Mahmud, T. S. Kalkur, A. Jamil, N.Cramer, A 1-GHz Active Phase Shifter With a Ferroelectric Varactor IEEE Microw. Wirel. Compon. Lett. **16**, (2006) 261.

[7] D. Kuylenstierna, A. Vorobiev, P. Linnér, S. Gevorgian, Composite Right/Left Handed Transmission Line Phase Shifter Using Ferroelectric Varactors, IEEE Microw.Wirel. Compon. Lett. **16**, (2006) 167.

[8] J. Nath, D. Ghosh, J.-P. Maria, A. I. Kingon, W. Fathelbab, P. D. Franzon, M.B. Steer, An Electronically Tunable Microstrip Bandpass Filter Using Thin-Film Barium Strontium Titanate (BST) Varactors, IEEE Trans. Microw. Theory Techn. **53** (2005) 2707.

[9] L.-Y. Chen, R. Forse, D. Chase, R. York, Analog Tunable Matching Network Using Integrated Thin-Film BST Capacitors, IEEE MTT-S Intl. Microwave Symp. Digest, **1** (2004) 261.

[10] M.W. Cole, C. Hubbard, E. Ngo, M. Ervin, M. Wood, R.G. Geyer, Structure-property relationships in pure and acceptor-doped $Ba_{1-x}Sr_xTiO_3$ thin films for tunable microwave device applications, J. Appl. Phys.**92**, (2002) 475.

[11] R. York, A. Nagra, E.Erker, T.Taylor, P.Periaswamy, J.Speck., S. Streiffer, O. Auciello, Microwave Integrated Circuits Uning Thin-Film BST, IEEE Int. Ferro.**1**, (2000) 195.

[12] P. Bao, T.J. Jackson, X. Wang, M.J. Lancaster, Barium strontium titanate thin film varactors for room-temperature microwave device applications, J. Phys.D: Appl.Phys. **41** (2008) 063001.

[13] L.Solymar, D.Walsh, Lectures on the Electrical Properties of Materials, 5th ed., Oxford University Press, Oxford, UK, 1993.

[14] S. Gevorgian, A. Vorobiev, D.Kuylenstierna, A. Deleniv, S. Abadei, A.Eriksson, P. Rundqvist, Silicon Substrate Integrated Ferroelectric Microwave Components, Integr. Ferroelectr. **66**, (2004) 125.

[15] R.A. York, Tunable Dielectrics for RF Circuits, in: Multifunctional Adaptive Microwave Circuits and Systems, Scitech Publishing, 2009.

[16] D. E. Kotecki, J.D. Baniecki, H. Shen, R.B. Laibowitz, K.L. Saenger, J.J. Lian, T.M. Shaw, S.D. Athavale, C. Cabral, P.R. Duncombe, M. Gutsche, G. Kunkel, Y.-J. Park, Y.-Y. Wang, R. Wise, (Ba,Sr)TiO_3 dielectrics for future stacked-capacitor DRAM, IBM J.Res. Dev. **43**, (1999)369.

[17] A.R.V. Hippel, Dielectric materials and applications: Papers by twenty-two contributors, John Wiley & Sons, Inc. 1954.

[18] S.O. Kasap, Principles of Electronic Materials and Devices, 3rd ed., McGraw-Hill, New York, 2006.

[19] C. Kittel, Introduction to Solid State physics, 8th ed., John Wiley&Sons, Inc., Hoboken,NJ, 2005.

[20] K.C.Kao, Dielectric Phenomena in Solids Elsevier,Inc. San Diego, 2004.

[21] C. Elissalde, J. Ravez, Ferroelectric ceramics: defects and dielectric relaxations, J. Mater. Chem. **11** (2001)1957.

[22] U. Bottger, Dielectric Properties of Polar Oxides, (2005)12.

[23] J. Valaske, Piezo-Electric and Allied Phenomena in Rochelle Salt, Phys. Rev. **17**, (1921) 475.

[24] A. J. Moulson, J.M. Herbert, Electroceramics: Materials. Properties. Applications, 2nd ed. John Wiley & Sons Ltd., Chichester, England, 2003.

[25] C. P. Poole. Jr., Encyclopedic Dictionary of Condensed Matter Physics, Elsevier Academic Press, London, 2004, pp. 1658.

[26] J. P. Srivastava, Elements of Solid State Physics, 3rd ed., PHI Learning Private Ltd., New Delhi, 2011.

[27] V. N. Murzin, R. E. Pasynkov, S.P. Solovev, Ferroelectricity and Crystal-Lattice Dynamics, Sov. Phys. Usp. **10**, (1968) 453.

[28] W. Cochran, Crystal Stability and the Theory of Ferroelectricity, Phys. Rev. Lett. **3**, (1959) 412.

[29] J. F. Scott, Applications of modern ferroelectrics, Science, **315** (2007) 954.

[30] S. Gevorgian, Ferroelectrics in Agile Microwave Components, Arm. J. Phys.**2**, (2009) 64.

[31] A. K. Tagantsev, V.O. Sherman, K.F. Astafiev, J.Venkatesh, N. Setter, Ferroelectric Materials for Microwave Tunable Applications, J. Electroceram. **11**, (2003) 5.

[32] T. Mitsui, I. Tatsuzaki, E. Nakamura, An Introduction to the Physics of Ferroelectrics, Gordon and Breach Scienece Publishers, LTD., London, 1976.

[33] S. Gevorgian, Ferroelectrics in Microwave Devices, Circuits and Systems: Physics, Modelling, Fabrication and Measurements, Springer-Verlag London Ltd, London, 2009.

[34] M.W. Cole, R.G. Geyer, Novel tunable acceptor doped BST thin films for high quality tunable microwave devices, Rev. Mex. Fis. **50,** (2004) 232.

[35] F.Jona, G.Shirane, Ferroelectric Crystals, Dover Publications,Inc., New York, 1993.

[36] T. Schneider, H. Beck, E. Stoll, Quantum effects in an n-component vector model for structural phase transitions, Phys. Rev. B, **13** (1976) 1123.

[37] K. Müller, H. Burkard, $SrTiO_3$: An intrinsic quantum paraelectric below 4 K, Phys. Rev. B **19**, (1979) 3593.

[38] C. Fu, C. Yang, H. Chen, Y. Wang, L. Hu, Microstructure and dielectric properties of $Ba_xSr_{1-x}TiO_3$ ceramics, Mater.Sci. Eng.: B **119,** (2005)185.

[39] H.V. Alexandru, C. Berbecaru, A. Ioachim, L. Nedelcu, A. Dutu, BST solid solutions, temperature evolution of the ferroelectric transitions, Appl.Surf. Sci. **253**, (2006) 354.

[40] L. Davis, L.G. Rubin, Some Dielectric Properties of Barium-Strontium Titanate Ceramics at 3000 Megacycles, J. Appl.Phys. **24,** (1953) 1194.

[41] T.M. Shaw, Z. Suo, M. Huang, E. Liniger, R.B. Laibowitz, J.D. Baniecki, The effect of stress on the dielectric properties of barium strontium titanate thin films, Appl.Phys. Lett. **75,** (1999) 2129.

[42] S. Yamamichi, H. Yabuta, T. Sakuma, Y. Miyasaka, (Ba+Sr)/Ti ratio dependence of the dielectric properties for $(Ba_{0.5}Sr_{0.5})Ti0_3$ thin films prepared by ion beam sputtering, Appl. Phys.Lett. **64**, (1994) 1644.

[43] Y. Gim, T. Hudson, Y. Fan, C. Kwon, A. T. Findikoglu, B. J. Gibbons, B. H. Park, Q. X. Jia, Microstructure and dielectric properties of $Ba_{1-x}Sr_xTiO_3$ films grown on $LaAlO_3$ substrates, Appl.Phys. Lett. **77**, (2000)1200.

[44] A.A. Sirenko, C. Bernhard, A. Golnik, A.M. Clark, J. Hao, W. Si, X.X. Xi, Soft-mode hardening in $SrTiO_3$ thin flms, Nature, **404**, (2000) 373.

[45] W. Chang, J. S. Horwitz, A.n C. Carter, J. M. Pond, S. W. Kirchoefer, C.M. Gilmore, D. B. Chrisey, The effect of annealing on the microwave properties of $Ba_{0.5}Sr_{0.5}TiO_3$ thin films, Appl.Phys. Lett. **74**, (1999)1033.

[46] A. A. Sirenko, I. A. Akimov, J. R. Fox, A. M. Clark, Hong-Cheng Li, Weidong Si, X.X. Xi, Observation of the First-Order Raman Scattering in $SrTiO_3$Thin Films, Phys. Rev. Lett. **82**, (1999) 4500.

[47] C. Zhou, D.M. Newns, Intrinsic dead layer effect and the performance of ferroelectric thin film capacitors, J. Appl.Phys. **82**, (1997) 3081.

[48] J. Im, O. Auciello, P. K. Baumann, S. K. Streiffer, D. Y. Kaufman, A. R. Krauss, Composition-control of magnetron-sputter-deposited $(Ba_xSr_{1-x})Ti_{1+y}O_{3+z}$ thin films for voltage tunable devices, Appl.Phys. Lett. **76**, (2000) 625.

[49] W. K. Simon, E. K. Akdogan, A. Safari, Misfit strain relaxation in $Ba_{0.6}Sr_{0.4}TiO_3$ epitaxial thin films on orthorhombic $NdGaO_3$substrates, Appl.Phys. Lett. **89**, (2006) 022902.

[50] B. H. Park, E. J. Peterson, Q. X. Jia, A. A. Sirenko, J. Lee, X. Zeng, W. Si, X.X. Xi, Effects of very thin strain layers on dielectric properties of epitaxial $Ba_{0.6}Sr_{0.4}TiO_3$films, Appl. Phys. Lett.78 (2001) 533.

[51] W. Chang, C.M. Gilmore, W.-J. Kim, J.M. Pond, S.W. Kirchoefer, S.B. Qadri, D.B. Chirsey, J.S. Horwitz, Influence of strain on microwave dielectric properties of $(Ba,Sr)TiO_3$ thin films, J. Appl.Phys. **87**, (2000) 3044.

[52] L.J. Sinnamon, M.M. Saad, R.M. Bowman, J.M. Gregg, Exploring grain size as a cause for "dead-layer" effects in thin film capacitors, Appl.Phys. Lett. **81**, (2002)703.

[53] C.T. Black, Jeffrey J. Welser, Electric-Field Penetration Into Metals: Consequences for High-Dielectric-Constant Capacitors, IEEE Trans. Electron Devices, **46**, (1999) 776.

[54] H.Rohdin, N.Moll, A.M.Bratkovsky, C.-Y.Su, Dispersion and Tunneling analysis interfacial gate resistance in Shottky barriers, Phys.Rev.B, Condens.Matter. **59**, (1999) 13102.

[55] U. Ellerkmann, R. Liedtke, U. Boettger, Interface-related thickness dependence of the tunability in $BaSrTiO_3$ thin films, Appl.Phys. Lett. **85**, (2004) 4708.

[56] M. Dawber, K. M. Rabe, J. F. Scott, Physics of thin-film ferroelectric oxides, Rev. Mod. Phys. **77,** (2005) 1083.

[57] R. Dittmann, R. Plonka, E. Vasco, N. A. Pertsev, J. Q. He, C. L. Jia, S. Hoffmann-Eifert, R. Waser, Sharp ferroelectric phase transition in strained single-crystalline $SrRuO_3$/ $Ba_{0.7}Sr_{0.3}TiO_3$/$SrRuO_3$ capacitors, Appl.Phys. Lett. **83** (2003) 5011.

[58] W.-J. Lee, H.-G.Kim, S.-G.Yoon, Microstructure dependence of electrical properties of $(Ba_{0.5}Sr_{0.5})TiO_3$thin films deposited on $Pt/SiO_2/Si$, J. Appl. Phys. **80**, (1996) 5891.

[59] A. Podpirka, M.W. Cole, S. Ramanathan, Effect of photon irradiation on structural, dielectric, and insulating properties of $Ba_{0.6}Sr_{0.4}TiO_3$ thin films, Appl.Phys. Lett. **92**, (2008) 212906.

[60] T. Kawahara, M. Yamamuka, T. Makita, J. Naka, A. Yuuki, N. Mikami, K. Ono, Step Coverage and Electrical-Properties of (Ba, Sr)TiO_3 Films Prepared by Liquid Source

Chemical-Vapor-Deposition Using TiO(DPM)(2), J. J. Appl. Phys.Part 1-Regular Papers Short Notes & Review Papers, **33**, (1994) 5129.

[61] C.B. Eom, J.Z. Sun, K. Yamamoto, A.F. Marshall, K.E. Luther, T.H. Geballe, S.S. Laderman, In situ grown $YBa_2Cu_3O_{7-d}$ thin films from single-target magnetron sputtering, Appl.Phys. Lett. **55,** (1989) 595.

[62] U. Poppe, J. Schubert, R.R. Arons, W. Evers, C.H. Freiburg, W. Reichert, K. Schmidt, W. Sybertz, K. Urban, Direct production of crystalline superconducting thin films of $YBa_2Cu_3O_7$ by high-pressure oxygen sputtering, Solid State Commun. **66**, (1988) 661.

[63] K. Tanabe, D.K. Lathrop, S.E. Russek, R.A. Buhrman, Epitaxial Y-Ba-Cu-O thin films on MgO deposited by high-pressure reactive magnetron sputtering, J.Appl.Phys. **66** (1989) 3148.

[64] M.W. Cole, P.C. Joshi, M.H. Ervin, La doped $Ba_{1-x}Sr_xTiO_3$ thin films for tunable device applications, J. Appl.Phys. **89**, (2001) 6336.

[65] N. Navi, J.S.Horwitz, R.C.Y.Auyeung, S.B. Qadri, H.-D. Wu Microwave dielectric properties of W-doped $Ba_{0.6}Sr_{0.4}TiO_3$ thin films grown on (001) MgO by pulsed laser deposition with a variable oxygen deposition pressure, Thin Solid Films, **510** (2002) 115.

[66] S.Y. Wang, B.L. Cheng, C. Wang, T.W. Button, S.Y. Dai, K.J. Jin, H.B. Lu, Y.L. Zhou, Z.H. Chen, G.Z. Yang, Ce-doping effects on electronic structures of $Ba_{0.5}Sr_{0.5}TiO_3$ thin film, J. Phys.D: Appl. Phys. **39,** (2006) 979.

[67] T.G. In, S. Baik, S. Kim, Leakage current of Al- or Nb-doped $Ba_{0.5}Sr_{0.5}TiO_3$ thin films by rf magnetron sputtering, J. Mater. Res. **13** (1998) 990.

[68] M.W. Cole, P.C. Joshi, M.H. Ervin, M.C. Wood, R.L. Pfeffer, The influence of Mg doping on the materials properties of $Ba_{1-x}Sr_xTiO_3$ thin films for tunable device applications, Thin Solid Films,**374,** (2000) 34.

[69] Y.-L. Kuo, J.-M. Wu, Tunable dielectric properties of lead barium zirconate niobate films, Appl.Phys. Lett. **89**, (2006) 132911.

[70] S.-Y. Chen, H.-W. Wang, L.-C. Huang, Electrical properties of Mg/La, Mg/Nb Co-doped $(Ba_{0.7}Sr_{0.3})TiO_3$ thin films prepared by metallo-organic deposition method, J.J. Appl. Phys. Part 1, **40,** (2001) 4974.

[71] M. L. Green, I.Takeuchi, J.R. Hattrick-Simpers, Applications of high throughput (combinatorial) methodologies to electronic, magnetic, optical, and energy-related materials, J. Mater. Sci. Lett.**113**, (2013) 231101.

[72] I. Takeuchi, J. Lauterbach, M. Fasolka, Combinatorial materials synthesis, Mater. Today, **8**, (2005)18.

[73] R. Waser, T. Schneller, S. Hoffmann-eifert, P. Ehrhart, Advanced chemical deposition techniques- from research to production, Integr. Ferroelectr. **36**, (2001) 3.

[74] J.-S. Kang, H.-C. Kim, Y.-B. Kim, D.-K. Choi, S.-T. Kim, C.-Y. Yoo, Metal-Organic CVD of a (Ba,Sr)RuO_3 Oxide Electrode Using a Single Cocktail Source, Chem. Vap. Deposition,**11**, (2005)17.

[75] S. Stemmer, S.K. Streiffer, N.D. Browning, A.I. Kingon, Accommodation of nonstoichiometry in (100) fiber-textured $Ba_xSr_{1-x}Ti_{1+y}O_{3+z}$ thin films grown by chemical vapor deposition, Appl.Phys. Lett. **74,** (1999) 2432.

[76] S.K. Streiffer, C. Basceri, C.B. Parker, S.E. Lash, A.I. Kingon, Ferroelectricity in thin films: The dielectric response of fiber-textured $(Ba_xSr_{1-x})T_{1+y}O_{3+z}$ thin films grown by chemical vapor deposition, J. Appl.Phys. **86**, (1999) 4565.

[77] S. Saha, D.Y. Kaufman, S.K. Streiffer, O. Auciello, Anomalous leakage current characteristics of Pt/($Ba_{0.75}Sr_{0.25}Ti_{1+y}O_{3+z}$)/Pt thin films grown by metalorganic chemical vapor deposition, Appl.Phys. Lett. **83,** (2003) 1414.

[78] T. Kawahara, M. Yamamuka, A. Yuuki, K. Ono, (Ba, Sr)TiO3 films prepared by liquid source chemical vapor deposition on Ru electrodes, J.J. Appl. Phys.Part 1-Regular Papers Short Notes & Review Papers, **35,** (1996) 4880.

[79] P.C. Joshi, S. Ramanathan, S.B. Desu, S. Stowell, S. Sengupta, Characterization of $Ba_{0.6}Sr_{0.4}TiO_3$ thin films with Mg additive fabricated by metalorganic decomposition technique, Integr. Ferroelectr.**19**, (1998) 141.

[80] M.S. Bhuiyan, M. Paranthaman, K. Salama, Solution-derived textured oxide thin films—a review, Supercond. Sci. Technol. **19**, (2006) R1.

[81] F. Yan, P. Bao, Z. Zhang, J. Zhu, Y. Wang, H. L.W. Chan, C.-L. Choy, Dielectric properties of $(Ba_{0.5}Sr_{0.5})TiO_3$ thin films, Thin Solid Films, **375**, (2000) 184.

[82] V.A. Vasiljev, K.A. Vorotilov, Sol-Gel Derived Barium-Strontium Titanate Films, J. Sol-Gel Sci. Technol. **13**, (1998) 877.

[83] W.J. Kim, W. Chang, S.B. Qadri, J.M. Pond, S.W. Kirchoefer, D.B. Chrisey, J.S. Horwitz, Microwave properties of tetragonally distorted $Ba_{0.5}Sr_{0.5}TiO_3$ thin films, Appl.Phys. Lett.,**76**, (2000) 1185.

[84] M S Tsai, T Y Tseng, Effect of oxygen to argon ratio on defects and electrical conductivities in $Ba_{0.47}Sr_{0.53}TiO_3$ thin-film capacitors, J. Phys. D: Appl. Phys. **32** (1999) 2141.

[85] R. Reshmi, M.K. Jayaraj, M.T. Sebastian, Influence of Oxygen to Argon Ratio on the Properties of RF Magnetron Sputtered $Ba_{0.7}Sr_{0.3}TiO_3$ Thin Films, J.Electrochem. Soc.**158**, (2011) G124.

[86] H. Shen, Y. Gao, P. Zhou, J. Ma, J. Sun, X. Meng, J. Chu, Effect of oxygen to argon ratio on properties of (Ba,Sr)TiO_3 thin films prepared on $LaNiO_3$/Si substrates, J. Appl.Phys. **105**, (2009) 061637.

[87] D.B. Chrisey, G.K. Hubler, Pulsed Laser deposition of thin films, John wiley&Sons, New York, 1994.

[88] S. Swann, Magnetron Sputtering, Phys.Technol. **19,** (1988) 67.

[89] D. Smith, Thin-Film Deposition McGraw Hill, New York, 1995.

[90] M. Ohring, The Material Science of Thin Films, Academic Press, New York, 1992.

[91] K. Seshan, Handbook of Thin-Film Deposition Processes and Techniques: Principles, Methods, Equipment and Applications,2nd (Ed.), William Andrew Publishing, Norwich, NY, 2002.

[92] A. B. Kozyrev, A. V. Ivanov, O. I. Soldatenkov, A. V. Tumarkin, S. V. Razumov, S. Yu. Aigunova, Ferroelectric (Ba,Sr)TiO_3Thin-Film 60-GHz Phase Shifter, Tech.Phys. Lett. **27,** (2001) 1032.

[93] T. B. Samoilova, A. B. Kozyrev, A. V. Tumarkin, A. M. Nikolaenko, A. G. Gagarin, Microwave Up-Converter Based on a Nonlinear Ferroelectric Capacitor, Tech. Phys. Lett. **50**, (2005) 1335.

[94] P.Sigmund, Theory of Sputtering. I. Sputtering Yield of Amorphous and Polycrystalline Targets, Phys. Rev.**184**, (1969) 383.

[95] T.S. Kim, C.H. Kim, M.H. Oh, Structural and electrical properties of rf magnetron-sputtered $Ba_{1-x}Sr_xTiO_3$ thin films on indium-tin-oxide-coated glass substrate, J. Appl.Phys.**75**, (1994) 7998.

[96] M. Migliuolo, R. M. Belan, J. A. Brewer, Absence of negative ion effects during on-axis single target sputter depositions of Y-Ba-Cu-O thin films on Si(100) Appl.Phys. Lett. **56,** (1990) 2572.

[97] B.D. Cullity, S.R. Stock, Elements of X-ray Diffraction, 3rd ed., Prentice-Hall, Inc., Upper Saddle River, NJ, 2001.

[98] T. C. Huang, P. K. Predecki, Grazing-Incidence X-ray Technique For Surface, Interface, and Thin-Film Analysis Adv. X-ray Anal. **40**, (1997) 056.

[99] B.K.Tanner, T .P.A.Hase, T.A.Lafford, M. .S.Goorsky, Grazing Incidence In-Plane X - Ray Diffraction in the Laboratory, Adv. X-ray Anal. **47**, (2004) 309.

[100] T.L.Alford, L.C. Feldman, J.W. Mayer, Fundamentals of Nanoscale Film Analysis, Springer Science+Business Media, Inc., NewYork, 2007.

[101] X. Hou, B.T. Jones, Inductively Coupled Plasma/Optical Emission Spectrometry, R.A.Meyers (Ed.) Encyclopedia of Analytical Chemistry, John Wiley & Sons Ltd., Chichester, 2000, pp.9468.

[102] J.F. Watts, J. Wolstenholme, An Introduction to Surface Analysis by XPS and AES, 2nd ed., John Wiley & Sons Ltd., Chichester, England, 2003.

[103] I. Bahl, Lumped Elements for RF and Microwave Circuits, Artech House, Inc., Norwood, MA, 2003.

[104] Z. Ma, A. J. Becker, P. Polakos, H. Huggins, J. Pastalan, H. Wu, K. Watts, Y. H. Wong, P. Mankiewich, RF Measurement Technique for Characterizing Thin Dielectric Films, IEEE Trans. Electron Devices, **45**, (1998) 1811.

[105] A. Vorobiev, P. Rundqvist, K. Khamchane, S. Gevorgian, Silicon substrate integrated high Q-factor parallel-plate ferroelectric varactors for microwave millimeterwave applications, Appl.Phys. Lett. **83**, (2003) 3144.

[106] R. Roongtaoa, W. C.Vittayakorn, Synthesis of barium titanate-barium magnesium niobate solid solution by a mixed-oxide method. J. Ceram. Proc. Res., **12** (2011) 398.

[107] T. Remmel, R. Gregory, B. Baumert, Characterization of barium strontium titanate films using XRD, Adv. X-Ray Anal. **41,** (1999) 38.

[108] S.W. Kirchoefer, J.M. Pond, A.C. Carter, W. Chang, K.K. Agarwal, J.S. Horwitz, D.B. Chrisey1, Microwave Properties Of $Sr_{0.5}Ba_{0.5}TiO_3$Thin-Film Interdigitated Capacitors, Microw. Optical Technol. Lett. **18**, (1998)168.

[109] I.P. Koutsaroff, P. Woo, L. McNeil, M. Zelner, A. Kassam, M. Capanu, L. Chmiel, B. McClelland, A. Cervin-Lawry, Dielectric Properties of (Ba,Sr)TiO_3 MOD Films Grown on Various Substrates, IEEE Int.Ferro.(2002)247.

[110] D. Rafajaa, J. Kubb, D.S. imek, J. Lindner, J. Petzelt, Microstructure of $Ba_xSr_{1-x}TiO_3$ thin films grown on sapphire substrates, Thin Solid Films, **422**, (2002) 8.

[111] Z.G. Ban, S.P.Alpay, Phase diagrams and dielectric response of epitaxial barium strontium titanate films: A theoretical analysis, J. Appl.Phys. **91**, (2002) 9288.

[112] G.W. Dietz, M. Schumacher, R. Waser, S.K. Streiffer, C. Basceri, A.I. Kingon, Leakage currents in $Ba_{0.7}Sr_{0.3}TiO_3$ thin films for ultrahigh-density dynamic random access memories, J. Appl.Phys. **82,** (1997) 2359.

[113] M. Copel, P.R. Duncombe, D.A. Neumayer, T.M. Shaw, R.M. Tromp, Metallization induced band bending of $SrTiO_3$(100) and $Ba_{0.7}Sr_{0.3}TiO_3$, Appl.Phys. Lett. **70,** (1997) 3227.

[114] J.O. Olowolafe, R.E. Jones, A.C. Campbell, R.I. Hegde, C.J. Mogab, R.B. Gregory, Effects of anneal ambients and Pt thickness on Pt/Ti and Pt/Ti/TiN interfacial reactions, J. Appl.Phys.**73,** (1993)1764.

[115] H.-J. Nam, D.-K. Choi, W.-J.Lee, Formation of hillocks in Pt/Ti electrodes and their effects on short phenomena of PZT films deposited by reactive sputtering, Thin Solid Films, **371,** (2000) 264.

[116] Z.-T.Song, N. Chong, L.-W. Helen, W. Chan, C.-L. Choy, C.L. Lin, Thermal stability of electrode stacks for application in oxide film devices, Thin Solid Films, **406**, (2002)268.

[117] D. Peng, Z. Meng, Influence of buffer layer on dielectric properties of $Ba_{1-x}Sr_xTiO_3$ thin films, Micro. Eng. **66,** (2003) 631.

[118] D.-S. Kil, B.-I. Lee, S.-K. Joo, Effect of deposition conditions of buffer layer on the characteristics of $(Ba,Sr)TiO_3$ thin films fabricated by a self-buffering process, Thin Solid Films, **343**, (1999) 453.

[119] A.R. Katritzky, M. Kuanar, S. Slavov, C.D. Hall, M. Karelson, I. Kahn, D.A. Dobchev, Quantitative Correlation of Physical and Chemical Properties with Chemical Structure: Utility for Prediction, Chem. Rev. **110,** (2010) 5714.

[120] T. Miyao, M. Arakawa, K. Funatsu, Exhaustive Structure Generation for Inverse-QSPR/QSAR, Molecular Informatics, **29**, (2010)111.

[121] T. Remmel, M. Schulberg, S. Fujimura, H. Honma, H. Kobayashi, H. Kohno, S. Owens, R. Deslattes, J. Pedulla, Barium strontium titanate thin film analysis, Adv. X-Ray Anal., **43**, (2000) 541.

[122] N.K. Pervez, P.J. Hansen, R.A. York, High tunability barium strontium titanate thin films for rf circuit applications, Appl.Phys. Lett. **85**, (2004) 4451.

[123] B.A. Baumert, L.H. Chang, A.T. Matsuda, T.L. Tsai, C.J. Tracy, R.B. Gregory, P.L. Fejes, N.G. Cave, W. Chen, D.J. Taylor, T. Otsuki, E. Fujii, S. Hayashi, K. Suu, Characterization of sputtered barium strontium titanate and strontium titanate-thin films, J. Appl.Phys. **82**, (1997) 2558.

[124] L.C. Angela, R.B. Rand, S. Guru, K. Gregory, A.K. Richard, N.Z. Hollie, C.H. Simon, A.G. Bartek, D.R. Bonnie, L.P. Timothy, Microwave characterization of nanostructured ferroelectric $Ba_{0.6}Sr_{0.4}TiO_3$ thin films fabricated by pulsed laser deposition, Nanotechnology, **19**, (2008) 485704.

[125] M.S. Tsai, S.C. Sun, T.Y. Tseng, Effect of oxygen to argon ratio on properties of $(Ba,Sr)TiO_3$ thin films prepared by radio-frequency magnetron sputtering, J. Appl.Phys. **82**, (1997) 3482.

[126] R.-B. Zhang, C.-S. Yang, G.-P. Ding, The effects of oxygen partial pressure on BST thin films deposited on multilayered bottom electrodes, Mater. Lett. **59**, (2005) 1741.

[127] J.M. Grace, D.B. McDonald, M.T. Reiten, J. Olson, R.T. Kampwirth, K.E. Gray, The Effect of Oxidant On re-Sputtering Of Bi From Bi-Sr-Ca-Cu-O Films, J. Vac. Sci. Technol. A-Vac. Surf. Films,**10**, (1992) 1600.

[128] A. Hamerich, R. Wunderlich, J. Muller, Modeling of Deposition and re-Sputtering Rate Profiles in Planar Face-To-Face Sputtering Systems, J. Vac. Sci. Technol. A-Vac. Surf. Films, **12**, (1994) 2873.

[129] J.M. Grace, D.B. McDonald, M.T. Reiten, J. Olson, R.T. Kampwirth, K.E. Gray, Selective resputtering of bismuth in sputtered Bi-Sr-Ca-Cu-O films, J. Appl.Phys.**70**, (1991) 3867.

[130] D. Cox, T. Fryberger, S. Semancik, Oxygen vacancies and defect electronic states on the SnO_2(110)-1×1 surface, Phys. Rev. B **38** (1988) 2072.

[131] S. Srivastav, C. V. R. Vasant Kumar, A. Mansingh, Effect of Oxygen on the Physical parameters of RF sputtered ZnO thin film, J. Phys. D: Appl. Phys. **22**, (1989) 1768.

[132] F. Alema, A. Reinholz, K. Pokhodnya, Stoichiometry and phase purity control of radio frequency magnetron sputter deposited $Ba_{0.45}Sr_{0.55}TiO_3$ thin films for tunable devices, J. Appl.Phys. **114**, (2013) 174104.

[133] R. Varatharajan, P. Santhanaraghavan, R. Jayavel, G. Bocelli, L. Right, P. Ramasamy, $BaSrTiCeO_3$: growth and crystal structure, Cryst. Eng. **3**, (2000) 195.

[134] K.-T. Kim, C.-I. Kim, Electrical and dielectric properties of Ce-doped $Ba_{0.6}Sr_{0.4}TiO_3$ thin films, Surf. Coat. Technol. **200**, (2006) 4708.

[135] R. Varatharajan, S. Madeswaran, R. Jayavel, Nb:barium strontium titanate (BST) Crystal growth and ferroelectric properties, J. Cryst. Growth, **225**, (2001) 484.

[136] D.M. Potrepka, S.C. Tidrow, A. Tauber, Improved Temperature Stability of Microwave Properties in Tunable Devices Using Substituted $Ba_{1-x}Sr_xTiO_3$, Integr. Ferroelectr. **42**, (2002) 97.

[137] J. Ravez, M. Pouchard, P. Hagenmuller, Chemical bonding, a relevant tool for designing new perovskite-type ferroelectric materials, Ferroelectrics, **197**, (1997) 797.

[138] L. Yang, W.Q. Cao, Dielectric and ferroelectric properties of Nb-doped $Ba_{0.8}Sr_{0.2}TiO_3$ ceramics, J. Electroceram. **21**, (2007) 206.

[139] S. Gopalan, C.-H. Wong, V. Balu, J.-H. Lee, J.H. Han, R. Mohammedali, J.C. Lee, Effect of niobium doping on the microstructure and electrical properties of strontium titanate thin films for semiconductor memory application, Appl.Phys. Lett. **75**, (1999) 2123.

[140] S.S. Kim, C. Park, Leakage current behaviors of acceptor- and donor-doped ($Ba_{0.5}Sr_{0.5}TiO_3$ thin films, Appl.Phys. Lett. **75,** (1999) 2554.

[141] F.Weill, J. L.Rehspringer, P.Poix, J.C.Bernier, Dielectric Characterization of $BTiO_3$-$BaM_{1/3}N_{2/3}O_3$ Systams (with M=Co,Mg and N=Nb or Ta), J. Mater. Sci. **27,** (1992) 2321.

[142] A. Munpakdee, J. Tontragoon, K. Siriwitayakorn, T. Tunkasiri, Effects of $Ba(Mg_{1/3}Nb_{2/3})O_3$ on microstructure and dielectric properties of barium titanate ceramics, J. Mater. Sci. Lett. **22**, (2003) 1307.

[143] T. Z.-Qing, L.H.-Xing, Y. H.-Tao, O. S.-Xi, Molten Salt Synthesis of $Ba(Mg_{1/3}Nb_{2/3})O_3$ Powder, J. Wuhan Univ. Technol. Mater. Sci. Ed.**19**, (2004) 17.

[144] F. Alema, M. Reich, A. Reinholz, K. Pokhodnya, Effect of concurrent Mg/Nb-doping on dielectric properties of $Ba_{0.45}Sr_{0.55}TiO_3$ thin films, J. Appl.Phys. **114,** (2013) 084102.

[145] M. Mayer, SIMNRA User's Guide, Max-Planck-Institut für Plasmaphysik Boltzmannstr. 2006.

[146] Windischmann H, Intrinsic Stress in Sputter-Deposited Thin Films, Crit. Rev. Solid State Mater. Sci.**17**, (1992) 547.

[147] Noyan. I.C, Cohen J.B., Residual Stress in Materials, American Scientist, **79**, (1991) 142.

[148] S. J. Skrzypek, A. Baczmanaski, W. Ratuszek, E. Kusior, New approach to stress analysis based on grazingincidence X-ray diffraction, J. Appl. Crystallogr. **34**, (2001) 427.

[149] V. Valvoda, R. Kuzel, R. Cerny, D. Rafaja, J. Musil, S. Kadlec, A.J. Perry, Structural Analysis of TiN Films by Seemann-Bohlin X-ray diffraction, Thin Solid Films **193**, (1990) 401.

[150] S. Lu, Z. Xu, Internal residual stress studies and enhanced dielectric properties in $La_{0.7}Sr_{0.3}CoO_3$ buffered $(Ba,Sr)TiO_3$ thin films, J. Appl.Phys. **106** (2009) 064107.

[151] F. Fitsilis, S. Regnery, P. Ehrhart, R. Waser, F. Schienle, M. Schumacher, M. Dauelsberg, P. Strzyzewski, H.J. b, BST thin films grown in a multiwafer MOCVD reactor, J. Eur. Ceram. Soc. **21**, (2001) 1547.

[152] S. Ito, H. Funakubo, I.P. Koutsaroff, M. Zelner, A. Cervin-Lawry, Effect of the thermal expansion matching on the dielectric tunability of (100)-one-axis-oriented $(Ba_{0.5}Sr_{0.5}TiO_3$ thin films, Appl.Phys. Lett. **90,** (2007) 142910.

[153] L.B. Freund, S. Suresh, Thin Film Materials: Stress, Defect Formation and Surface Evolution, Cambridge University Press, Cambridge, NY, 2003.

[154] X. W.-Hua, L.D. Zhang, T.-Yi, Determination of residual stresses in Pb $Zr_{0.53}Ti_{0.47}O_3$ thin films with Raman spectroscopy, Appl.Phys. Lett. **79**, (2001) 4112.

[155] R.W. Hoffman, Stresses in Thin-Films -Relevance of Grain-Boundaries and Impurities, Thin Solid Films **34,** (1976) 185.

[156] T.R. Taylor, P.J. Hansen, B. Acikel, N. Pervez, R.A. York, S.K. Streiffer, J.S. Speck, Impact of thermal strain on the dielectric constant of sputtered barium strontium titanate thin films, Appl.Phys. Lett. **80**, (2002) 1978.

[157] W.D. Nothwang, M.W. Cole, S.G. Hirsch, Grain Growth and Residual Stress in BST Thin Films, Integr. Ferroelectr. **71**, (2005) 107.

[158] J.W. Edwards, R. Speiser, H.L. Johnston, High Temperature Structure and Thermal Expansion of Some Metals as Determined by X-Ray Diffraction Data. I. Platinum, Tantalum, Niobium, and Molybdenum, J. Appl.Phys. **22**, (1951) 424.

[159] M.B. Okatan, M.W. Cole, S.P. Alpay, Dielectric tunability of graded barium strontium titanate multilayers: Effect of thermal strains, J. Appl.Phys. **104**, (2008) 104107.

[160] W.D. Nothwang, M.W. Cole, C. Hubbard, E. Ngo, Residual Stress Effects in Doped Barium Strontium Titanate Thin Films, J. Electrochem. Soc. **152**, (2005) F37.

[161] J. Vlassak, Thin Film Mechanics, in, Harvard University, Boston, MA, 2004.

[162] R.E. Chinn, Ceramography: Preparation and Analysis of Ceramic Microstructures 1st ed., Wiley-American Ceramic Society, 2002.

[163] Y. Kuru, M. Wohlschlogel, U. Welzel, E.J. Mittemeijer, Large excess volume in grain boundaries of stressed, nanocrystalline metallic thin films: Its effect on grain-growth kinetics, Appl.Phys. Lett. **95**, (2009) 163112.

[164] F.M. Pontes, E. Longo, E.R. Leite, J.A. Varela, Study of the dielectric and ferroelectric properties of chemically processed $Ba_xSr_{1-x}TiO_3$ thin films, Thin Solid Films **386**, (2001) 91.

[165] N. Sugii, K. Takagi, Change in surface morphologies with pulsed-laser-deposition-temperature for $SrTiO_3$ and $Ba_{0.7}Sr_{0.3}TiO_3$ thin films on Pt electrodes, Thin Solid Films **323**, (1998) 63.

[166] W.G.Nilsen, J.G.Skinner, Raman Spectrum of Strontium Titanate, J. Chem. Phys. **48**, (1968) 2240.

[167] M. DiDomenico, S. Wemple, S. Porto, R. Bauman, Raman Spectrum of Single-Domain $BaTiO_3$, Phys. Rev. **174**, (1968) 522.

[168] F.M. Pontes, E.R. Leite, D.S.L. Pontes, E. Longo, E.M.S. Santos, S. Mergulhão, P.S. Pizani, F. Lanciotti, T.M. Boschi, J.A. Varela, Ferroelectric and optical properties of $Ba_{0.8}Sr_{0.2}TiO_3$ thin film, J. Appl.Phys. **91**, (2002) 5972.

[169] X. Wei, N. P. Padture, Hydrothermal synthesis of tetragonal $Ba_xSr_{1-x}TiO_3$ powders, J. Ceram. Proc. Res. **5**, (2004) 175.

[170] L.Z. Cao, B.L. Cheng, S.Y. Wang, W.Y. Fu, S. Ding, Z.H. Sun, H.T. Yuan, Y.L. Zhou, Z.H. Chen, G.Z. Yang, Influence of stress on Raman spectra in $Ba_{1-x}Sr_xTiO_3$ thin films, J. Phys.D: Appl.Phys. **39**, (2006) 2819.

[171] S.Y. Wang, B.L. Cheng, C. Wang, S.Y. Dai, K.J. Jin, Y.L. Zhou, H.B. Lu, Z.H. Chen, G.Z. Yang, Raman spectroscopy studies of Ce-doping effects on $Ba_{0.5}Sr_{0.5}TiO_3$ thin films, J. Appl.Phys. **99**, (2006) 013504.

[172] A. Munpakdee, K. Pengpat, J. Tontrakoon, T. Tunkasiri, The study of dielectric diffuseness in the $Ba(Mg_{1/3}Nb_{2/3})O_3$-$BaTiO_3$ ceramic system, Smart Mater. Struct. **15,** (2006) 1255.

[173] B. Su, Microstructure and dielectric properties of Mg-doped barium strontium titanate ceramics, J. Appl.Phys. **95**, (2004)1382.

[174] R. Waser, Dielectric analysis of intergrated ceramic thin film capacitors, Integr. Ferroelectr.**15**, (1997) 39.

[175] J.F. Ihlefeld, A.M. Vodnick, S.P. Baker, W.J. Borland, J.-P. Maria, Extrinsic scaling effects on the dielectric response of ferroelectric thin films, J. Appl.Phys. **103**, (2008) 074112.

[176] K. Binder, Surface effects on phase transitions in ferroelectrics and antiferroelectrics, Ferroelectrics, **35**, (1981) 99.

[177] C.B. Parker, J.P. Maria, A.I. Kingon, Temperature and thickness dependent permittivity of (Ba,Sr)TiO_3 thin films, Appl.Phys. Lett., **81**, (2002) 340-342.

[178] B. Chen, H. Yang, L. Zhao, J. Miao, B. Xu, X.G. Qiu, B.R. Zhao, X.Y. Qi, X.F. Duan, Thickness and dielectric constant of dead layer in Pt/$(Ba_{0.7}Sr_{0.3}TiO_3)$/$YBa_2Cu_3O_{7-x}$ capacitor, Appl.Phys. Lett. **84**, (2004) 583.

[179] J.D. Baniecki, R.B. Laibowitz, T.M. Shaw, C. Parks, J. Lian, H. Xu, Q.Y. Ma, Hydrogen induced tunnel emission in Pt/$(Ba_xSr_{1-x}Ti_{1+y}O_{3+z})$/Pt thin film capacitors, J. Appl.Phys. **89**, (2001) 2873.

[180] D. R. Chase, L.-Y. Chen, Robert A. York, Modeling the Capacitive Nonlinearityin Thin-Film BST Varactors, IEEE Trans. Microw. Theory Techn. **53**, (2005) 3215.

[181] A. Vorobiev, P. Rundqvist, K. Khamchane, S. Gevorgian, Microwave loss mechanisms in $Ba_{0.25}Sr_{0.75}TiO_3$ thin film varactors, J. Mater. Sci. Lett. **96**, (2004) 4642.

[182] L. Pintilie, I. Vrejoiu, D. Hesse, G. LeRhun, M. Alexe, Ferroelectric polarization-leakage current relation in high quality epitaxial Pb(Zr,Ti)O_3 films, Phys. Rev. B **75**, (2007) 104103.

[183] S. Zafar, R.E. Jones, B. Jiang, B. White, V. Kaushik, S. Gillespie, The electronic conduction mechanism in barium strontium titanate thin films, Appl. Phys. Lett.**73**, (1998) 3533.

[184] S.M. Sze, Kwok.K.Ng, Physics of Semiconductor Devices, 3rd ed., John Wiley & Sons, Inc, Hoboken, New Jersey, 2007.

[185] P. Zubko, D.J. Jung, J.F. Scott, Electrical characterization of $PbZr_{0.4}Ti_{0.6}O_3$ capacitors, J. Appl.Phys.**100**, (2006) 114113.

[186] S.K. Sahoo, D. Misra, D.C. Agrawal, Y.N. Mohapatra, S.B. Majumder, R.S. Katiyar, Leakage mechanism of $Ba_{0.8}Sr_{0.2}TiO_3/ZrO_2$ multilayer thin films, J. Appl.Phys.**108**, (2010) 074112.

[187] H. Yang, K. Tao, B. Chen, X. Qiu, B. Xu, B. Zhao, Leakage mechanism of $Ba_{0.7}Sr_{0.3}TiO_3$ thin films in the low-temperature range, Appl.Phys. Lett. **81**, (2002) 4817.

[188] S.-T. Chang, J.Y.-m. Lee, Electrical conduction mechanism in high-dielectric-constant $(Ba_{0.5}Sr_{0.5})TiO_3$ thin films, Appl. Phys. Lett. **80**, (2002) 655.

[189] C.S. Hwang, B.T. Lee, C.S. Kang, K.H. Lee, H.-J. Cho, H. Hideki, W.D. Kim, S.I. Lee, M.Y. Lee, Depletion layer thickness and Schottky type carrier injection at the interface between Pt electrodes and (Ba, Sr)TiO_3 thin films, J. Appl. Phys. **85**, (1999) 287.

[190] Y.-P. Wang, T.-Y. Tseng, Electronic defect and trap-related current of $(Ba_{0.4}Sr_{0.6})TiO_3$ thin films, J. Appl.Phys. **81**, (1997) 6762.

[191] Y. Chishima, Y. Noguchi, Y. Kitanaka, M. Miyayama, Defect Control for Polarization Switching in $BiFeO_3$ Single Crystals, IEEE Trans. Ultrason.,Ferroelectr.,Freq.Control, **57**, (2010) 2233.

[192] H.Koinuma, I. Takeuchi, Combinatorial solid-state chemistry of inorganic materials, Nat.Mater. **3** (2004) 429.

[193] B. Wessler, V. Jéhanno, W. Rossner, W.F. Maier, Combinatorial synthesis of thin film libraries for microwave dielectrics, Appl. Surf. Sci. **223,** (2004) 30.

[194] X.X. -Dong, T.Ichiro, Combinatorial Materials Synthesis, Marcel Dekker, Inc., New York, Basel, 2003.

[195] Z.H. Barber, M.G. Blamire, High throughput thin film materials science, Mater. Sci. Technol. **24**, (2008)757.

[196] J. J. Hanak, The "Multiple-Sample Concept" in Materials Research: Synthesis, Compositional Analysis and Testing of Entire Multicomponent Syatems, J. Mater. Sci. **5**, (1970) 964.

[197] X.-D.Xiang, X. Sun, G.Briceno, Y.Lou, K.-A.Wang, H.Chang, W.G. W.-Freedman, S.-W. Chen, P.G. Schultz, A Combinatorial Approach to Materials Discovery, Science, **268**, (1995) 1738.

[198] X.-D. Xiang, Combinatorial Materials Synthesis and Screening: An Integrated Materials Chip Approach to Discovery and Optimization af Functional Materials, Annu. Rev. Mater. Sci. **29**, (1999) 149.

[199] E. W. McFarland, W.H. Weinberg, Combinatorial approaches to materials discovery, Tibtech, **17**, (1999) 107.

[200] R.A. Potyrailo, I. Takeuchi, Role of high-throughput characterization tools in combinatorial materials science, Meas. Sci.Technol. **16**, (2005) 1.

[201] R.C. Pullar, Y. Zhang, L. Chen, S. Yang, J.R.G. Evans, N.M. Alford, Manufacture and measurement of combinatorial libraries of dielectric ceramics Part I. Physical characterization of $Ba_{1-x}Sr_xTiO_3$ libraries, J. Eur. Ceram. Soc. **27**, (2007) 3861.

[202] R.C. Pullar, Y. Zhang, L. Chen, S. Yang, J.R.G. Evans, P.K. Petrov, A.N. Salak, D.A. Kiselev, A.L. Kholkin, V.M. Ferreira, N.M. Alford, Manufacture and measurement of combinatorial libraries of dielectric ceramics Part II. Dielectric measurements of $Ba_{1-x}Sr_xTiO_3$ libraries, J. Eur. Ceram. Soc. **27**, (2007) 4437.

[203] H. Chang, C. Gao, I. Takeuchi, Y. Yoo, J. Wang, P. G. Schultz, R. P. Sharma, M. Downes, T. Venkatesan, X.-D. Xiang, Combinatorial synthesis and high throughput evaluation of ferroelectric/dielectric thin-film libraries for microwave applications, Appl.Phys. Lett. **72**, (1998) 2185.

[204] I. Takeuchi, H. Chang, C. Gao, P. G. Schultz, X.-D. Xiang, R. P. Sharma, M. J. Downes, T. Venkatesan, Combinatorial synthesis and evaluation of epitaxial ferroelectric device libraries, Appl.Phys. Lett. **73**, (1998) 894.

[205] I.Takeuchi, R. B.van Dover, H. Koinuma, Combinatorial Synthesis and Evaluation of Functional Inorganic Materials Using Thin-Film Techniques, Mrs Bull. (2002) 301.

[206] K. Kennedy, T.Stefansky, G.Davy, V.F. Zackay, E. R.Parker, Rapid Method for Determining Ternary-Alloy Phase Diagrams, J. Appl. Phys.**36**, (1965) 3808

[207] R. B. van Dover, L. F. Schneemeyer, R.M. Fleming, Discovery of a useful thin-film dielectric using a composition-spread approach, Nature **392**, (1998) 162.

[208] I. Takeuchi, K. Chang, R. P. Sharma, L. A. Bendersky, H. Chang, X.-D. Xiang, E. A. Stach, C.-Y. Song, Microstructural properties of$(Ba,Sr)TiO_3$ films fabricated from $BaF_2/SrF_2/TiO_2$ amorphous multilayers using the combinatorial precursor method, J. Mater. Sci. Lett. **90**, (2001) 2474.

[209] K. S. Chang, M. Aronova, O. Famodu, I. Takeuchi, S.E. Lofland, J. Hattrick-Simpers, H. Chang, Multimode quantitative scanning microwave microscopy ofin situ grown epitaxial $Ba_{1-x}Sr_xTiO_3$ composition spreads, Appl.Phys. Lett. **79**, (2001) 4411.

[210] R E Treharne, K Hutchings, D A Lam, SJCIrvine, D Lane, K Durose, Combinatorial optimization of Al-doped ZnO films for thin-film photovoltaics, J. Phys.D: Appl.Phys. **45**, (2012) 335102.

[211] R. B. van Dover, E. M. Gyorgy, R. P. Frankenthal, M. Hong, D.J. Siconolf, Effect of oxidation on the magnetic properties of unprotected TbFe thin films, J. Appl. Phys.**59**, (1986) 1291.

[212] R. Gerson, T.C. Marshall, Dielectric breakdown in porous ceramics, J. Appl.Phys. **30**, (1959) 1650

[213] C. Basceri, S. K. Streiffer, A.I. Kingon, R. Waser, The dielectric response as a function of temperature and film thickness of fiber-textured (Ba,Sr)TiO3 thin films grown by chemical vapor deposition, J. Appl. Phys. **82**, (1997) 2497.

[214] L.Holland, Vacuum Deposition of Thin Films, 1st ed., John Wiley & Sons Inc.,New York, 1956.

[215] R.M. Rousseau, Detection Limit and Estimate of Uncertainty of Analytical XRF Results, The Rigaku Journal **18**, (2001) 33.

[216] U. G. Nielsen, A.Boisen, M.Brorson, C.J. H. Jacobsen, H.J. Jakobsen, J.Skibsted, Aluminum Orthovanadate (AlVO4): Synthesis and Characterization by ^{27}Al and ^{51}V MAS and MQMAS NMR Spectroscopy, Inorg. Chem. **41**, (2002) 6432.

[217] T. Riekkinen, Fabrication and characterization of ferro-and piezoelectric multilayer devices for high frequency applications, Helsinki University of Technology, Helsinki, 2009, pp. 96.

APPENDIX A. CAPACITOR FABRICATION PROCESS

The dielectric and electrical measurements were performed on a metal-insulator-metal (MIM) capacitor structure consisting of two capacitors connected in series on the platinized alumina wafers (Chapter 3). Due to the structural, morphological and other characterization prior to patterning the film, surface contamination is unavoidable. Thus, before starting the fabrication process, the wafers were annealed at 400 ^{o}C under the flow of oxygen to remove any organic as well as water molecules adsorbed on the surface of the film. Then, the wafers were taken straight to the sputtering chamber and a 500 nm platinum top electrode was deposited on them. Thick positive photoresist was coated on top of the platinum and capacitor structures were lithographically patterned, dry etched (at University of Minnesota Nanofabrication center (UM-NFC)). After dry etching (ion milling), the photoresist was stripped off by oxygen plasma using reactive ion etching (RIE). Ion milling and oxygen plasma damages the film by introducing defects, residual stress, and oxygen vacancies which have a detrimental effect on the electrical properties of the film. To alleviate this, the films must be annealed (i.e. repair annealing).

Steps for the fabrication of capacitor structures by lithography process:

1. Dehydration annealing is performed at 400 ^{o}C and 10 sccm of O_2 for 2 hours to remove organic contaminants and water from the surface of the film.
2. Deposit 500 nm platinum (Pt) top electrode.
3. Lithography processes:
    - Spin coat ~2 μm photoresist on top of the Pt electrode
    - Bake at 90 ^{o}C (soft baking) for 2 minutes.
    - Align mask and expose ~16 seconds
    - Bake at 120 ^{o}C (hard baking)~1.5 minutes

- Develop in OPD262 developer
- Inspect the patterns under optical microscope
- If the structure in not good repeat step 3
- If the structure is good, bake the wafer at 120 ^{o}C for 15 seconds

4. Dry etching (ion milling) the Pt electrode; the BST film is protected by the 2 μm photoresist.
5. Strip photoresist: use RIE by mixing 80 sccm of $O_{2,}$ and 10 sccm of CHF_3 at a pressure of 120 mTorr, power 200 W for 8-17 minutes.
6. Anneal the films at 650 ^{o}C under the flow of O_2 (15 sccm) for 2 hours.

APPENDIX B. THICKNESS PROFILE FOR COMBINATORIAL SETUP

In this appendix, detailed steps for obtaining analytical expressions of the film thickness for the combinatorial setup are presented. In this calculation, the following assumptions were considered: (1) the sputtering process is carried out at a sufficiently low pressure so that the scattering of sputtered atoms is negligible, (2) the collision between the sputtered molecules should be neglected, (3) every sputtered atom striking the wafer condenses on first impact, and (4) the sputtered particles are assumed to follow the Knudsen's cosine distribution.

Consider an infinitesimal mass, dm_{σ}, sputtered from an infinitesimal area, $d\sigma$, on the sputtering target (Figure B1 (A)) at the sputtering rate of S (gram/second). The fraction, say *dm*, of the sputtered mass that pass through a solid angle, dΩ, in the direction of an angle ϕ with the axis normal to the surface per unit time follows Knudsen's cosine law distribution as [214]

$$dm = \frac{S}{\pi}\cos\phi \, d\Omega. \tag{B1}$$

Assuming that all the particles passing through the solid angle arrive at an infinitesimal area, *dS*, on the substrate inclined at angle θ to the direction of the stream, the total mass of the material that lands on the substrate in the *dS* can be written as

$$dm = \frac{S}{\pi}\cos\phi\cos\theta\frac{dS}{r^2}. \tag{B2}$$

In this work, the thickness profile derivation is focused on RF magnetron sputtering since it is a suitable method for the deposition of dielectric or oxide films. When targets are sputtered in a magnetron sputtering setup, the electrons are confined by the Lorentz force to a region between the magnets leading to major erosion of the material from this region. Thus, one can approximate the usage of the target to be between the inner and outer magnets bounded by r_1 and r_2 as indicated in Figure B1 (B).

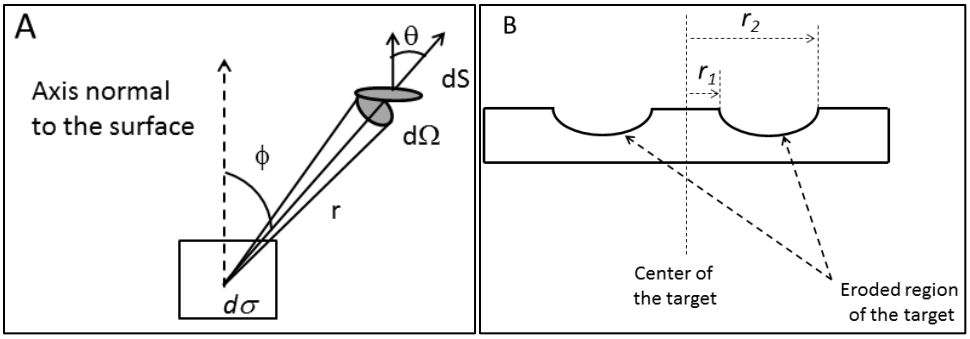

Figure B1. Scheme of target-substrate to set up the thickness calculation (A), the eroded regions between magnets in the magnetron sputtering (B)

In order to ensure the composition gradient across the substrate, it is necessary to shift and tilt the source material. In our combinatorial setup, two targets were equally shifted and tilted opposite to each other by the same tilt angle, and throw distance. Assume that a BST target doped with a dopant A is shifted to the left, while a BST target doped with a dopant B shifted to the right. Since the two sources are the same a calculation on one target will suffice to get the thickness profile due to the two sources.

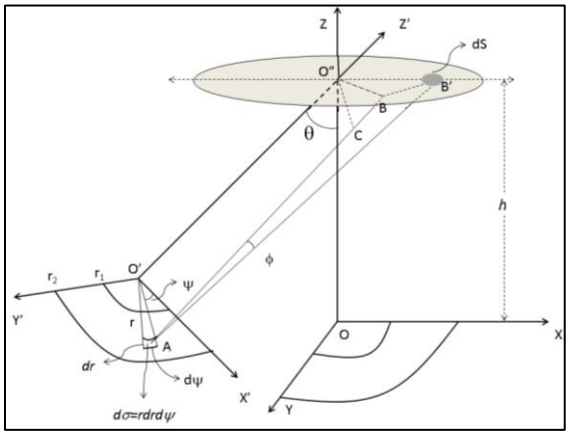

Figure B2. Schematic representation of a tilted target

Let's define the following parameters from the schematic above:

$\left|\overrightarrow{AB'}\right| = L;\ \left|\overrightarrow{OO"}\right| = \left|\overrightarrow{O'O"}\right| = \left|\overrightarrow{AC}\right| = h;\ \left|\overrightarrow{O"B}\right| = r\sec\theta;\ \left|\overrightarrow{CB}\right| = r\tan\theta;\ \left|\overrightarrow{AB}\right| = L' = h +$

$r \tan\theta$; $\left|\overrightarrow{O"B'}\right| = R$; where, R is a position on the substrate from the origin $O"$ and r is position on the target from its origin O'. Using a vector addition one can write $\overrightarrow{O'O''}+\overrightarrow{O''B'} - \overrightarrow{AB'} - \overrightarrow{O'A} = 0$, which leads to

$$\left|\overrightarrow{AB'}\right|^2 = \left|\overrightarrow{0'O''}\right|^2 + 2\overrightarrow{O'O''}.\left(\overrightarrow{O''B'} - \overrightarrow{O'A}\right) + \left|\left(\overrightarrow{O''B'} - \overrightarrow{OA'}\right)\right|^2. \quad \text{(B3)}$$

The angle between $\overrightarrow{O'O''}$ and $\overrightarrow{O''B'}$ is 90-θ, and $\overrightarrow{O'O''} \perp \overrightarrow{O'A}$, thus, Eq. (B3) can be simplified as

$$\left|\overrightarrow{AB'}\right|^2 = \left|\overrightarrow{0'O''}\right|^2 + 2\left|\overrightarrow{0'O''}\right|\left|\overrightarrow{0''B'}\right| \sin\theta + \left|\left(\overrightarrow{O''B'} - \overrightarrow{OA'}\right)\right|^2. \quad \text{(B4)}$$

By translating the vector $\overrightarrow{O''B'}$ to the origin of the X'Y'Z' coordinates, it can be expressed as $\overrightarrow{O"B'} = R\cos\theta\,\hat{\imath} + R\sin\theta\,\hat{k}$, and similarly, the vector $\overrightarrow{O'A}$ can be written as $\overrightarrow{O'A} = r\cos\psi\,\hat{\imath} + r\sin\psi\,\hat{\jmath}$, allowing us to write $\left|\left(\overrightarrow{O''B'} - \overrightarrow{OA'}\right)\right|^2 = \left|\left(\overrightarrow{O''B'}\right)\right|^2 + \left|\left(\overrightarrow{OA'}\right)\right|^2 - 2\left(\overrightarrow{O''B'}\right).\left(\overrightarrow{O'A}\right)$ to simplify Eq. (B4) as

$$\mathrm{L}^2 = \mathrm{h}^2 + \mathrm{r}^2 + R^2 + 2hR\sin\theta - 2rR\cos\theta\cos\psi. \quad \text{(B5)}$$

Similarly, from the vector addition of $\overrightarrow{AB}+\overrightarrow{BB'} - \overrightarrow{AB'} = 0$, the expressions for $\cos\phi$ can be written as

$$\cos\phi = \frac{L^2 + (h + r\tan\theta)^2 - \left(R^2 + r^2/(\cos\theta)^2 + 2rR\cos\psi/\cos\theta\right)}{2L(h + r\tan\theta)}. \quad \text{(B6)}$$

Furthermore,

$$\cos\beta = \frac{(\mathrm{h} + \mathrm{r}\tan\theta)\cos\theta}{\mathrm{L}}. \quad \text{(B7)}$$

The total mass sputtered off the infinitesimal area $d\sigma = rdrd\psi$ per unit time is given by

$$dm_\sigma = \frac{S_A d\sigma}{\pi(r_2^2 - r_1^2)} \quad \text{(B8)}$$

where, S_A is the sputter rate of the target doped with A. The mass, *dm*, which passes through a solid angle, $d\Omega = {\cos\beta\, dS}/{L^2}$, per unit time follows the Knudsen's cosine law in Eq. (B2)

$$dm = \frac{S_A \cos\phi \cos\beta\, d\sigma dS}{\pi^2(r_2^2 - r_1^2)L^2}. \quad \text{(B8)}$$

Suppose that all the *dm* materials that pass through the solid angle are deposited on the infinitesimal area, *dS*, and form a film of infinitesimal thickness, *dt*. Let ρ_A be the density of the A doped target, the infinitesimal mass that is deposited on the substrate can be written as

$$dm = \rho_A dV, \quad \text{(B9)}$$

where, ($dV = dtdS$) is the infinitesimal volume created by an infinitesimal area *dS* and thickness *dt*. Comparing B8 and B9, the infinitesimal thickness on the substrate can be written as

$$dt = \frac{S_A \cos\phi \cos\beta}{\rho_A \pi^2(r_2^2 - r_1^2)L^2} d\sigma. \quad \text{(B10)}$$

Substituting the expression for L, $\cos\phi$, $\cos\beta$, and $d\sigma$, the expression for the thickness profile for the film deposited from the A doped target is presented as

$$t_A = \frac{S_A}{\pi^2 \rho_{A(r_2{}^2 - r_1{}^2)}} \int_{r_1}^{r_2} \int_0^{2\pi} \frac{\cos\theta\left(2h^2 + 2rR\cos\varphi(\cos\theta - \sec\theta) + 2hR\sin\theta + 2hr\tan\theta\right)}{2(h^2 + r^2 + R^2 + 2rR\cos\theta\cos\varphi + 2hR\sin\theta)^2} r\, dr\, d\varphi. \quad \text{(B11)}$$

Similarly, the thickness on the film from the B doped target is expressed as

$$t_B = \frac{S_B}{\pi^2 \rho_{B(r_2{}^2 - r_1{}^2)}} \int_{r_1}^{r_2} \int_0^{2\pi} \frac{\cos\theta\left(2h^2 - 2rR\cos\varphi(\cos\theta - \sec\theta) - 2hR\sin\theta + 2hr\tan\theta\right)}{2(h^2 + r^2 + R^2 - 2rR\cos\theta\cos\varphi - 2hR\sin\theta)^2} r\, dr\, d\varphi. \quad \text{(B12)}$$

In the expression θ is the tilt angle, *h* is throw distance, S_A and S_B are the sputtering rates of the A and B doped targets, respectively; ρ_A and ρ_B are the density of the A and B doped targets, respectively; r_1 is the inner radius of erosion region (r_1=0 in the absence of magnet) and r_2 is the outer radius of erosion region (r_2 equals the radius of the target in the absence of magnet), *r* is the distance at any arbitrary point on the target from its center, and *R* is arbitrary distance on the substrate from its center.

Like-wise, the expression for the composition of the material on the substrate is estimated. Let the mass of the material deposited at a position, *R*, on the substrate from the A doped target be $M_A(R)$, and from the B doped target be $M_B(R)$. Then the $M_A(R)$ and $M_B(R)$ can be expressed as

$$M_A(R) = \rho_A \times V_A(R) = \rho_A \times A_S \times t_A(R), \tag{B13}$$

and

$$M_B(R) = \rho_B \times V_B(R) = \rho_B \times A_S \times t_B(R), \tag{B14}$$

where, $V_A(R)$ and $V_B(R)$ are the volume created due to the deposited material from the A and B doped targets at any point *R*, respectively, and A_S is the area of the substrate. The mass percentage (fraction) of each material at any point *R* on the substrate can be written as

$$\%A(R), \%B(R) = \frac{M_A(R), M_B(R)}{M_A(R) + M_B(R)} \times 100\%, \tag{B15}$$

where, $\%A(R)$ and $\%B(R)$ are the mass % of A and B doped materials on the film, respectively. Substituting B13 and B14 into B15, the variation of the percentage composition of each material with respect to position on the substrate is written as

$$\%A(R), \%B(R) = \frac{\rho_{A,B} t_{A,B}(R)}{\rho_A t_A(R) + \rho_B t_B(R)} \times 100\%. \tag{B16}$$